Doctoral Dissertation

博士論文

Revealing the Origins of Violent Stellar Transients
from Fast Radio Bursts and Magnetars

(高速電波バーストとマグネターからの
突発天体現象の起源解明)

A Dissertation Submitted for the Degree
of Doctor of Philosophy

令和元年12月博士 (理学) 申請

December 2019

Department of Astronomy, Graduate School of Science
The University of Tokyo

東京大学大学院理学系研究科
天文学専攻

Shotaro Yamasaki

山崎 翔太郎

Revealing the Origins of Violent Stellar Transients

from

Fast Radio Bursts and Magnetars

Shotaro Yamasaki

A dissertation submitted in conformity with the
requirements for the degree
of Doctor of Philosophy

in

Astronomy

in the

Graduate School of Science

of the

UNIVERSITY OF TOKYO

Feb 2020

Dissertation Advisor: Tomonori Totani   Shotaro Yamasaki

Revealing the Origins of Violent Stellar Transients

from

Fast Radio Bursts and Magnetars

Abstract

The transient sky is a goldmine of enigmatic violent astrophysical phenomena. Fast radio bursts (FRBs) are one of such mysterious transients with millisecond-duration bright radio flashes originating from beyond our galaxy. Most of FRBs have not been observed to repeat and such non-repeating FRBs may be explained by pulsar-like emissions expected from the merger of double neutron stars. In the Chapter 2, by using numerical-relativity simulations of a BNS merger, we examine this scenario with particular focus on the spatial distribution of the matter ejected during the coalescence, which may prohibit the FRB signal to propagate. We show that the formation of ejecta occurs about 1 ms after the rotation speed of the merged neutron star becomes sufficiently high enough to produce an FRB. Furthermore, we propose a new scenario that a super young (1–10 yr) neutron star left after the binary neutron star merger could be an origin of repeating FRBs. In Chapter 3, we highlight one of the key observable quantities of FRBs, the dispersion measure (DM), which is defined as an electron column density from the source to the observer. Thanks to their extragalactic origin, FRBs offer a unique approach to probe the unknown matter distribution inside and outside galaxies. We provide a new model for the hot gas distribution inside our Galaxy, thereby estimating its contribution to the DM of FRBs. Since our model predicts relatively large DM values over the whole sky, this strong DM signal would be imprinted onto the DM of FRBs, which could be tested by using an increasing sample of nearby FRBs with a small DM.

The second half of this thesis is dedicated to magnetars, a class of highly magnetized isolated neutron stars, which may be related to FRBs. Magnetars are distinguished by their violent flaring/bursting activities in X- to soft gamma-rays with luminosity ranging over ten orders of magnitude. Huge amounts of magnetic energy are released as a hot electron-positron pair plasma (fireball), observed as a flare. We begin Chapter 4 by stressing possible relationship between magnetar flares and radio transients. We particularly investigate how magnetar flares influence on the coherent radio pulsations and find that radio pulsations would be absorbed by the

expanding plasma flow launched by magnetar flares. Since the plasma frequency would decrease with time, the timescale for the radio suppression would be shorter for higher frequencies. Namely, an unambiguous test of our model would be provided by future simultaneous observations of radio-emitting neutron stars at X-ray and at multiple radio frequencies during a period of magnetar flares. Finally, in Chapter 5, we present our recent progress on the spectral formation of magnetar flares in terms of the resonant inverse Compton scattering, which is the most efficient process in the magnetospheres. We predict that the original thermal spectrum arising from the magnetosphere should be mildly Comptonized, which is in good agreement with the observed spectra of magnetar flares observed in 2006 March from SGR 1900+14.

Acknowledgments

Contents

Chapter 1

Introduction

1.1 Preface

Since the serendipitous discoveries in the 2000s (Lorimer et al. 2007; Thornton et al. 2013), Fast Radio Bursts (FRBs) has been receiving increasing attention during the last decade, growing up to be a new forefront fields in modern astronomy. Since the discovery of the so-called Lorimer Burst (Lorimer et al. 2007) and four additional bursts (Thornton et al. 2013), about 100 FRBs have been reported by various radio transient surveys to date (see Petroff et al. 2016 and references therein). Interestingly, their dispersion measures $\mathrm{DM} \equiv \int n_e ds$ (a line-of-sight integration of electron number density n_e), typically hundreds of $\mathrm{pc\,cm^{-3}}$, far exceed that accumulated through the interstellar medium (ISM) of the Galaxy or its halo, suggesting their cosmological origins at $z = 0.1$–2 (Ioka 2003; Inoue 2004) provided that the dominant contribution to DMs is induced by electrons in the ionized intergalactic medium (IGM).

Observationally, some FRBs are seen to repeat multiple times, while the bulk of FRBs so far do not show the evidence of repetition ($\sim 90\%$ as of late 2019). The first repeating source, FRB 121102, has been observed to repeat, allowing it to be localized (Spitler et al. 2016). A persistent radio counterpart and host galaxy were identified at a redshift of $z = 0.19$, confirming extragalactic origin for FRBs (Section 1.2.3). With the advent of other powerful FRB surveys, such as the Canadian Hydrogen Intensity Mapping Experiment (CHIME; CHIME/FRB Collaboration et al. 2018) and Australian Square Kilometre Array Pathfinder (ASKAP; Johnston et al. 2008), there have been additional landmark discoveries (Section 1.2.4), contributing to the FRB phenomenology. Along with these observational advances, a range of progenitor models for FRBs have been actively proposed by theorists. Most remark-

ably, observations of FRB 121102 gave a great boost to the interpretation of FRBs as the activity of young neutron star (possibly with strong magnetic fields, called "magnetars") produced through some sort of formation channels (Section 1.2.3).

Considering and predicting potential origins of FRBs is one of the important themes in this thesis. This is because such models connect FRBs closely to other extreme transient phenomena in modern astrophysics, such as magnetars, gamma-ray bursts (GRBs), supernovae (SNe), compact stellar mergers and gravitational waves, making important links across different wavelengths and research fields. We will particularly investigate the existing binary neutron star merger model for FRBs (Section 2). On the other hand, whatever their origins are, the observed dispersion and rotation measures of FRBs itself provide unique probes of baryons and magnetic fields in and outside galaxies (Section 1.2.6), which will certainly yield more accurate information about the local environment of FRBs (i.e., amounts of local dispersion) and thus help us constrain the origins of FRBs in the long run. As the first step toward this aim, we will carry out a complementary study on the Galactic baryon distribution in this work (Chapter 3)

The second theme of this thesis is uncovering the origins of magnetar flares, which are invoked to explain some extreme transients in the Universe, such as GRBs, SNe and FRBs (as mentioned above). Magnetars (Duncan & Thompson 1992, see also Paczynski 1992; Usov 1992) represent an enigmatic subclass of strongly magnetized neutron stars. They possess the strongest magnetic fields known in the Universe, with polar surface values of $B_p \sim 10^{13}$–10^{15} G, which are typically a few orders of magnitude higher than that for normal radio pulsars, and also exceed the quantum critical field strength at Schwinger limit $B_Q \equiv m_e^2 c^3/(\hbar e) \sim 4.4 \times 10^{13}$ G. This high field value makes them quickly spin down and thus spin periods for Galactic magnetars are the longest among all isolated pulsars that are generally powered by rotation. Intriguingly, magnetars are uniquely characterized by its violent flaring/bursting activities across a wide range of luminosity (Section 1.3.1).

Though the field of magnetar flares have already reached a certain level of maturity (at least its progenitor is known), the emission mechanism still remain unclear (e.g., Kaspi & Beloborodov 2017; Section 1.3.2). This may be partly due to the limited number of energetic flares with sufficient photon statistics and simultaneous multiwavelength observations. In this work, we will consider two fundamental problems that remain properly unanswered: "*What is the relationship between magnetar flares and radio emissions?*" and "*What shapes the magnetar flare spectra inside the magnetosphere?*". Regarding the former question, a focus will be on the generation of electron-positron plasma at the onset of flares and its subsequent expansion which bring about the absorption of the radio emission (Chapter 4). Meanwhile, for

the latter, we will consider the possible spectral distortion due to the resonant inverse Compton scattering, which is the most efficient process in the magnetospheres (Chapter 5).

In summary, this thesis will examine the origins and nature of possibly connected two violent stellar transients: FRBs and magnetar flares in the spirit of revealing their origins individually (i.e., instead of attempting to reveal the connection between FRBs and magnetars, which could be a future work). The remainder of this introductory chapter is organized as follows. We begin in Section 1.2 and in 1.3 with the phenomenological and theoretical aspects of FRBs and magnetar flares, respectively. In addition, we also provide subsections describing important observations that motivate the works in the subsequent chapters. We then conclude in Section 1.4 with an outline of the remainder of the thesis. During writing this chapter, we have greatly benefited from most recent reviews (Katz 2016; Keane 2018; Popov et al. 2018; Cordes & Chatterjee 2019; Petroff et al. 2019 for FRBs, and Rea & Esposito 2011; Kaspi & Beloborodov 2017; Enoto et al. 2019 for magnetized neutron stars). More specific details and references will be offered in the tailor-made introduction sections of each chapter.

1.2 Fast Radio Bursts

1.2.1 Diagnostics by Propagation Effects

The following review of the basic plasma physics follows the one given by Rybicki & Lightman (1979). Maxwell's equations for a uniform plasma that consists of electrons with number density n_e yields to the dispersion relation connecting the wave number k and the wave frequency ω as

$$\omega^2 = \omega_p^2 + k^2 c^2, \tag{1.1}$$

where the plasma frequency ω_p is defined as

$$\omega_p = \sqrt{\frac{4\pi n_e e^2}{m_e}} \sim 5.6 \times 10^4 \ \text{Hz} \ \left(\frac{n_e}{\text{cm}^{-3}}\right)^{1/2}. \tag{1.2}$$

One can see that the wave number becomes imaginary when $\omega < \omega_p$. In this case, the plane wave function ψ can be expressed as

$$\psi \propto e^{i(kx-\omega t)} = \exp\left(-\sqrt{|\omega^2 - \omega_p^2|}\, x/c\right) e^{-i\omega t}, \tag{1.3}$$

and thus its amplitude decreases exponentially on a negligible scale length of $2\pi c/\omega_p$. This is why ω_p is often referred to as "plasma cutoff frequency", below which any waves are prevented from propagating through media. Conversely, when $\omega > \omega_p$, the electromagnetic radiation propagates with the group velocity, defined as

$$v_g \equiv \frac{\partial \omega}{\partial k} = c\sqrt{1 - \frac{\omega_p^2}{\omega^2}} \approx c\left(1 - \frac{\omega_p^2}{2\omega^2}\right), \qquad (1.4)$$

where $\sqrt{1 - \omega_p^2/\omega^2}$ is the refraction index. The last approximation holds when $\omega_p \ll \omega$, which is the case for a MHz–GHz radio pulse propagating through typical interstellar media (ISM) with $\nu_p \lesssim 10^3$ Hz. Since v_g is always less than the speed of light, a radio pulse traveling through a plasma with a length scale D arrives later than in pure vacuum by

$$
\begin{aligned}
\Delta t &= \int_0^D \frac{ds}{v_g} - \frac{D}{c} \\
&\sim 4.150 \text{ msec} \left(\frac{\nu}{\text{GHz}}\right)^{-2} \left(\frac{\text{DM}}{\text{pc cm}^{-3}}\right),
\end{aligned}
\qquad (1.5)
$$

where we have replaced angular frequency ω with frequency ν for observational convenience and defined the DM as

$$\text{DM} \equiv \int_0^D n_e \, ds, \qquad (1.6)$$

which is normally measured in units of pc cm^{-3}. In terms of observation, the above dispersion law ($\Delta t \propto \nu^{-2}$) is known to hold within 1% accuracy (see Cordes & Chatterjee 2019 and references therein), and thus the DM can be determined by the slope of the pulse sweep seen in the ν–t plane (e.g., see the upper panel of Figure 1.1). The DM as a distance modulus will be discussed in Section 1.2.2 and Chapter 3.

When the intervening plasma has a density fluctuation due to the turbulence, the frequency-dependent scattering effects, such as temporal broadening and diffractive scintillation, also come into play. The former in the broadening of the pulse width (the broadening time scales with $\propto \nu^{-4.4}$), while the latter results in the intensity modulation in time (Rickett 1990; Cordes et al. 2017).

For a linearly-polarized wave, the polarization angle rotates as the wave propagates through a magnetized medium, which is so-called "Faraday Rotation". The
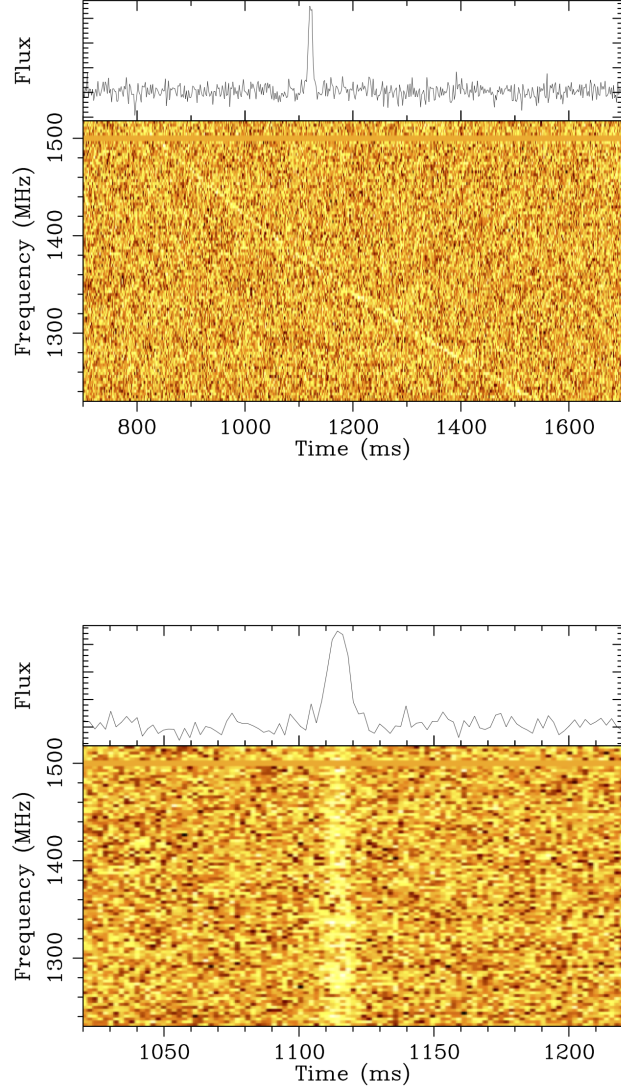
Figure 1.1: Dynamic spectra (ν-t plane) and light curves (burst flux versus t) of FRB 010125 originally reported by Lorimer et al. (2007) (the data are available at the FRB Catalogue: Petroff et al. 2016). The lower panel is for the same event but after the de-dispersion (removing frequency-dependent time delays due to the dispersion effect) at the correct DM value of $790\,\mathrm{pc\,cm^{-3}}$.

Faraday Rotation is expressed by

$$\Psi = \text{RM}\,\lambda^2, \tag{1.7}$$

where Ψ is the polarization position angle of the wave in radians with respect to its infinite-ν limit of $\lambda = 0$ (λ is the wavelength in m). Here we define the rotation measure (RM) as

$$\begin{aligned} \text{RM} &= \frac{e^3}{2\pi m_e^2 c^4} \int_0^D n_e \boldsymbol{B} \cdot d\boldsymbol{s} \\ &\sim 0.810 \ \text{rad}\,\text{m}^{-2} \int_0^D \left(\frac{n_e}{\text{cm}^{-3}}\right) \left(\frac{\boldsymbol{B}}{\mu\text{G}}\right) \cdot \left(\frac{d\boldsymbol{s}}{\text{pc}}\right), \end{aligned} \tag{1.8}$$

where $\boldsymbol{B}$ denotes the vector magnetic field at each position on a line-of-site, and $d\boldsymbol{s}$ is the vector line-of-site element. Therefore the RM gives a useful measure of the line-of-sight component of the magnetic field and the electron number density of the medium. At the time of writing, eight sources, FRBs 110523 (Masui et al. 2015), 121102 (Michilli et al. 2018), 150215 (Petroff et al. 2015), 150807 (Ravi et al. 2016), 151230, 160102 (Caleb et al. 2018), 180301 (Price et al. 2019) and 181226 (CHIME/FRB Collaboration et al. 2019) have been reported to show a significant degree of linear polarization (30–100%), which allows for a measurement of the RM. Some of them show a negligible RM with absolute values $\sim \mathcal{O}(10\ \text{rad}\,\text{m}^{-2})$ (FRBs 150215 and 150807) and/or comparable to the Galactic foreground contribution with $\sim \mathcal{O}(100\ \text{rad}\,\text{m}^{-2})$ (FRBs 110523, 160102 and 181226), whereas FRB 121102 exhibits a larger RM of $\sim \mathcal{O}(10^5\ \text{rad}\,\text{m}^{-2})$ as much as four orders of magnitude in excess of the Galactic contribution, implying that the burst had traveled through a highly magnetized, dense plasma near its origin. Such a diversity in the RMs might be used as a discriminator between differing progenitors, since the RM has a tendency to directly reflect the local surrounding environment of the source than the DM does (see also Chapter 2).

1.2.2 Distance, Rate and Energetics

Distance

One of the most astounding natures of FRBs is their large DM, which significantly exceeds the DM contribution from the Galactic cold electrons. Figure 1.2 illustrates the observed DMs for FRBs in comparison with the Galactic pulsar population. According to the ATNF Pulsar Catalogue (Manchester et al. 2005), the median DM of
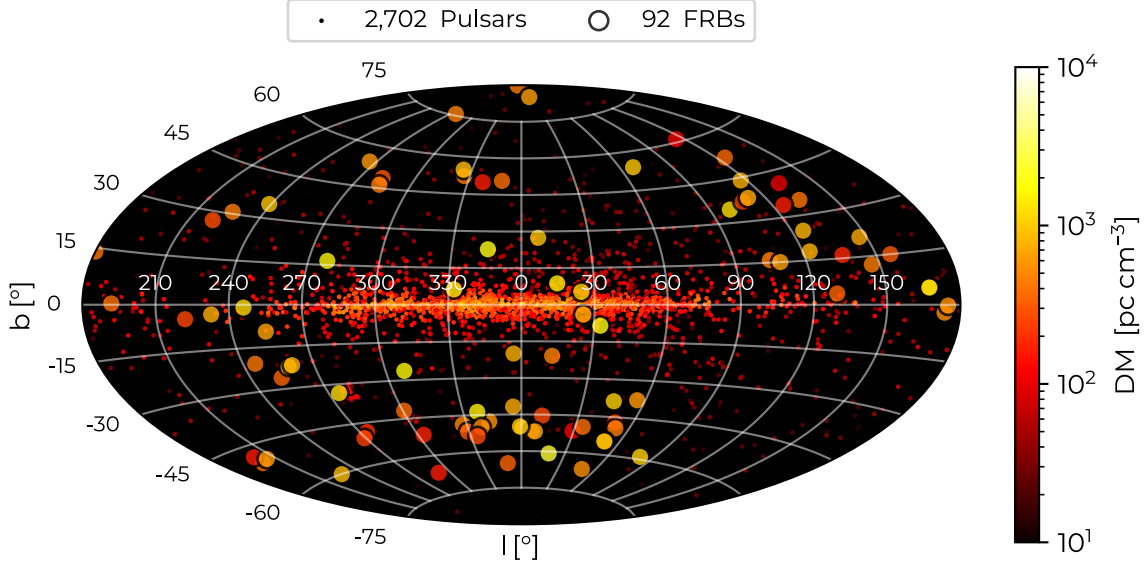
Figure 1.2: All-sky map (Galactic coordinates) of FRB (FRBCAT: Petroff et al. 2016) and Galactic pulsar (The ATNF Pulsar catalogue: Manchester et al. 2005) DMs. One can see that FRBs have almost isotropic spatial distribution in the sky and show higher DM values compared to Galactic pulsars.

all Galactic pulsars is $\mathrm{DM_{pulsar}} = 133$ pc cm^{-3}, with a maximum of 1778 pc cm^{-3} in the Galactic center. Meanwhile, FRBs typically show $\mathrm{DM_{FRB}} = 100\text{--}2600$ pc cm^{-3} at significantly high Galactic latitudes, where the Galactic contribution to the DM is negligibly small. Therefore, the distance to FRBs should be extremely large if the DM excess is responsible for the intergalactic medium whose density is several orders of magnitude smaller than the typical ISM. Given the simplified DM-redshift relation (Ioka 2003; Inoue 2004; Deng & Zhang 2014), $z \approx (\mathrm{DM_{FRB}} - \mathrm{DM_{MW}})/900$, the cosmological distance of FRBs at $z \lesssim 2$ is immediately inferred. The more extensive discussion on the DM-redshift relation will be given in Chapter 3. The above prediction is also supported by the almost isotropic sky distribution of FRBs, which is in stark contrast to pulsars that are concentrated on the Galactic Stellar disk as demonstrated in Figure 1.2. This is in fact a reminiscence of cosmological GRBs. As

will be further presented in Section 1.2.4, the cosmological distance scale of FRBs is now being nearly established thanks to successful localization of FRBs to their host galaxies.

Detection Rate

FRBs are also uniquely characterized by its high occurrence rate around GHz frequencies (0.8–8 GHz). At 1.4 GHz, Thornton et al. (2013) first derived all sky rate of FRBs as $N_{\mathrm{FRB}} = 10^3$–10^4 sky^{-1} day^{-1} above the burst fluence of $\mathcal{O}(1$ Jy ms). The results for different surveys at $\sim$GHz frequencies are broadly consistent with the above figure with a trend toward the lower-end value $N_{\mathrm{FRB}} \sim 10^3$ sky^{-1} day^{-1} (see Table 1 of Cordes & Chatterjee 2019), and no strong Galactic latitude dependence of burst detection rates has been reported so far (Petroff et al. 2014; Spitler et al. 2014; Keane & Petroff 2015; Champion et al. 2016; Scholz et al. 2016; Bhandari et al. 2018). Assuming the maximum comoving distance of observable FRBs is $D_{\mathrm{max}} \sim 3$ Gpc (corresponding to a redshift of $z = 1$), the above all-sky detection rate is translated into the intrinsic FRB event rate density of

$$\mathcal{R}_{\mathrm{FRB}} \sim 3.2 \times 10^3 \ \mathrm{Gpc}^{-3} \ \mathrm{yr}^{-1} \left(\frac{N_{\mathrm{FRB}}}{10^3 \ \mathrm{sky}^{-1} \ \mathrm{day}^{-1}} \right) \left(\frac{D_{\mathrm{max}}}{3 \ \mathrm{Gpc}} \right)^{-3} \left(\frac{f_b}{1} \right)^{-1}. \quad (1.9)$$

Here f_b is the beaming factor of FRBs defined by $f_b \equiv \Delta\Omega/4\pi$, where $\Delta\Omega$ is the solid angle over which an FRB is emitted. As one can see, a small beaming fraction would significantly affect the estimate of the rate density. The above qualitative estimate indicates that the FRB event rate density is roughly a hundred times higher than typical GRB rate (e.g., Zhang 2018).

Coherent Process

Despite the large uncertainty regarding the nature of FRB progenitors (see Section 1.2.5), there is a wide consensus on the necessity for a coherent emission process. In the radio astronomy, it is useful to estimate the brightness temperature T_b of the source to distinguish whether the process is thermal or non-thermal (i.e., coherent). The brightness temperature is defined as an effective blackbody temperature of the Planck spectrum with the Rayleigh-Jeans approximation: $k_B T_b = c^2/(2\nu^2)I_\nu$, where k_B and I_ν are the Boltzmann's constant and the specific intensity (brightness) of the source, respectively. Let us consider a source at a distance D with its observed duration Δt, the observed solid angle of the beam Ω_s and the fluence $\mathcal{F}_\nu$. Then the

specific intensity of the source is written as

$$I_\nu = \frac{\mathcal{F}_\nu}{\Delta t\, \Omega_s} \approx \frac{\mathcal{F}_\nu}{\Delta t}\left(\frac{\Delta x}{D}\right)^{-2}, \tag{1.10}$$

where Δx is the observed source size. The brightness temperature is

$$k_B T_b \equiv \frac{I_\nu\, c^2}{2\nu^2} \approx \frac{\mathcal{F}_\nu}{2\nu^2}\frac{D^2}{\Delta t^3}, \tag{1.11}$$

where we have assumed $\Delta x \approx c\Delta t$. Typical parameters for an FRB yield

$$T_b \sim 3.5 \times 10^{35}~\text{K}~\left(\frac{\mathcal{F}_\nu}{\text{Jy ms}}\right)\left(\frac{\Delta t}{\text{ms}}\right)^{-3}\left(\frac{\nu}{\text{GHz}}\right)^{-2}\left(\frac{D}{\text{Gpc}}\right)^2, \tag{1.12}$$

which far exceeds the upper-limit on the brightness temperature for an incoherent electron synchronton radiation called inverse Compton catastrophe limit $T_b = 10^{11}$–10^{12} K (Readhead 1994)[1]. Therefore, there is little doubt that FRB emission is *not* from thermal process but from coherent process like the pulsar radio emission.

Energy and Power

The true (beaming-corrected) emission energy of an FRB can be estimated by assuming a flat radio spectrum ($\mathcal{F}_\nu \propto \nu^0$) over the observing band width $\Delta \nu$ as

$$E \approx 4\pi D^2 \mathcal{F}_\nu \Delta\nu f_b \sim 1.2 \times 10^{39}~\text{erg}~\left(\frac{\mathcal{F}_\nu}{\text{Jy ms}}\right)\left(\frac{\Delta\nu}{\text{GHz}}\right)\left(\frac{D}{\text{Gpc}}\right)^2\left(\frac{f_b}{1}\right). \tag{1.13}$$

This translates into a peak luminosity of $\sim 1.2 \times 10^{42}\, f_b$ erg s^{-1} for bursts with millisecond duration. This huge energy release makes FRBs one of the brightest radio transients in the Universe.

1.2.3 Repeating Sources

FRB 121102 was the first FRB discovered by Arecibo Radio Telescope at 1.4 GHz band (Spitler et al. 2014) when only several FRBs had been reported by the Parkes Radio Telescope. This therefore supported the astrophysical origin of FRBs. Light was shed on the FRB mystery in 2016, when FRB 121102 was seen to repeat multiple

---

[1]In fact, this is the case even if the relativistic beaming effect of the source is taken into account, which would significantly decrease the rest-frame brightness temperature (see e.g., Katz 2014).

times (Spitler et al. 2016; Scholz et al. 2016) with all burst DMs consistent with the single value ~ 560 pc^{-3} pc, implying that they are the same in origin. This repeating nature of FRB 121102 enabled an extensive follow-up by the Karl G. Jansky Very Large Array in 83 hours over six months, which eventually led to the detection of recurrent FRBs with a high precision of $\sim 0.1''$ and thereby localizing FRBs to a star-forming ($\sim 0.4\,M_\odot\,\mathrm{yr}^{-1}$) dwarf ($M_\star \sim 6 \times 10^7 M_\odot$ where $M_\star$ is the total stellar mass) galaxy at a redshift of $z = 0.193$ (Chatterjee et al. 2017; Tendulkar et al. 2017; Marcote et al. 2017; Kokubo et al. 2017). This was the first unambiguous confirmation that, at least some FRBs have extragalactic origins.

Furthermore, FRB 121102 is known to associate with an unusually bright, quasi-steady (in time), compact (< 0.7 pc) radio source that coincides with the location of FRB 121102 but offsets from the nucleus of the host galaxy (Tendulkar et al. 2017). The currently favored interpretation of this bright radio source is a nebula powered by a young (with age ~ 10-100 yr) neutron star born from SNe (Murase et al. 2016; Kashiyama & Murase 2017; Metzger et al. 2017; Beloborodov 2017; Omand et al. 2018) or a super-young (with age ~ 1-10 yr) post-merger remnant neutron star of binary neutron stars (Yamasaki et al. 2018; Chapter 2, see also Margalit et al. 2019). FRB 121102 have shown to have an extremely large and variable ($\sim 10\%$ decrease over seven months) RM of $\sim 10^5$ rad m^{-2} (Michilli et al. 2018) with almost 100% linear polarization, indicating a highly-magnetized plasma environment.

Recently, additional nine repeating sources have been discovered by CHIME (CHIME/FRB Collaboration et al. 2018, 2019), which broadly share the complicated time-frequency pulse characteristics seen in FRB 121102 (Spitler et al. 2016; Hessels et al. 2019). Intriguingly, the study on a sample of CHIME FRBs detected at 400–800 MHz implies that repeating FRBs statistically have a much wider pulse duration than for FRBs that have not repeated, suggesting different emission mechanisms (CHIME/FRB Collaboration et al. 2019). Finally, FRB 171019 originally detected by the ASKAP survey (Shannon et al. 2018) has been seen to repeat by Green Bank Telescope (Kumar et al. 2019). Accordingly, the repeating FRBs are no more big news to the community, underpinning the notion that any FRBs may potentially repeat.

1.2.4   Host Galaxies

As seen in the history of cosmological GRBs, the great revolution in FRB astronomy should be directly linked to localization (Kulkarni 2018), which is about being proven correct. As of late 2019, the total number of localized FRBs is four (including repeating source FRB 121102 as mentioned in Chapter 1.2.3), out of about a hundred

total detected bursts. We summarize and show these landmark discoveries in Figure 1.3. The first two examples of host galaxies for thus far non-repeating FRBs 180924 (Bannister et al. 2019) and 190523 (Ravi et al. 2019) have been identified to more massive ($M_\star \sim 10^{10}$–$10^{11}\ M_\odot$) and quiescent galaxies than that of FRB 121102 at $z = 0.32$ and $z = 0.66$, respectively.

Most curiously, FRB 180924 was found to lie in the outskirt of the host at ~ 4 kpc from the galaxy center (1.4 times the half-light radius) thanks to ASKAP's sub-arcsecond accuracy for localization. Another interesting feature of this event is that it is not associated with a persistent radio source with an upper-limit of ~ 3 times fainter than FRB 121102, and it has a small RM of 14 rad m^{-2}. Regarding the other event FRB 190523 detected by Deep Synoptic Array (DSA), the localization power (roughly arcsecond resolution) is not as good as that of FRB 180924 by ASKAP. Nevertheless, the probability that FRB 190523 occurred in the outskirt of galaxy is high according to their FRB error ellipse (see black contours shown in bottom right panel of Figure 1.3). These two galaxies are in stark contrast to the host of FRB 121102, being a hundred to a thousand times more massive, with a greater than a hundred times lower specific star-formation rate (Bannister et al. 2019; Ravi et al. 2019). The properties of these galaxies highlight the possibility of an FRB production channel associated with older stellar populations such as binary neutron stars, which preferentially occur in elliptical galaxies with a relatively large offset from the galactic center presumably due to its high systemic velocity reflecting past two supernova explosions (e.g., Margalit et al. 2019).

Meanwhile, the arcsecond localization of FRB 181112 to an intermediate-mass ($\sim 2.6 \times 10^9\ M_\odot$) star-forming ($\sim 0.6\ M_\odot\,\mathrm{yr}^{-1}$) galaxy at $z = 0.48$ was subsequently followed (Prochaska et al. 2019). These discoveries, along with some unpublished news of additional host galaxy identifications, imply potential diversity in the properties of FRB host galaxies and progenitors. Namely, it is crucial to uncover more examples of their host galaxies to ultimately determine their causes.

1.2.5   Binary Neutron Star Coalescence Model

The millisecond duration and the enormous energy release of FRBs allow for a broad range of progenitor models particularly involving compact objects (see a comprehensive review for Platts et al. 2018). Roughly speaking, these models are classified by how many FRBs they are capable of producing, a single or multiple bursts. The former includes binary neutron star (or black hole) mergers (Totani 2013; Mingarelli et al. 2015), binary white dwarf mergers (Kashiyama et al. 2013), binary black hole mergers (Liu et al. 2016) and collapsing supermassive neutron stars (Falcke & Rezzolla

2014). Meanwhile, the latter includes giant flares from highly magnetized neutron stars (magnetars; Popov & Postnov 2010a; Thornton et al. 2013; Lyubarsky 2014; Kulkarni et al. 2014), giant radio pulses from pulsars (Connor et al. 2016; Cordes & Wasserman 2016), repeating FRBs from a young neutron star (Kashiyama & Murase 2017; Metzger et al. 2017; Beloborodov 2017), collisions of asteroids with a neutron star (Geng & Huang 2015; Dai et al. 2016), and pulsars interacting with plasma stream (Zhang 2017). Above all, the binary coalescence models are especially attractive because, if this were the case, FRBs would be promising electromagnetic counterparts to GW signals produced by compact binary mergers, and would be ideal targets for future multi-messenger studies. Since the majority of the models postulates that the FRB generation would take place only once through the merger process, obviously they cannot explain the repeating sources (but see Chapter 2 for the possible generation of repeating FRBs from the post-merger remnant).

Here we specialize to a binary neutron star (BNS) coalescence model proposed by Totani (2013), in which an FRB signal is explained as the pulsar-like coherent emission generated by the synchronization of the magnetosphere at the time of merger (see Wang et al. 2016 for a unipolar inductor model in which the energy is extracted from its orbital motion, not from rotation). During the last in-spiral of the merger, two neutron stars are expected to start to rapidly rotate at spin period of $P \sim 1$ ms due to the conservation of the binary orbital energy. The characteristic duration of FRBs is explained by the dynamical timescale of the merger (or the spin period of neutron star). The total power available through this process is limited by the energy loss rate due to magnetic dipole rotation

$$L_{\mathrm{MDR}} = 3.9 \times 10^{44} \text{ erg s}^{-1} \left(\frac{B_p}{10^{12.5} \text{ G}} \right)^2 \left(\frac{P}{1 \text{ ms}} \right)^{-4} \left(\frac{R}{10^6 \text{ cm}} \right)^6 , \qquad (1.14)$$

where B_p is the polar surface magnetic field strength and R the stellar radius. Therefore, if the neutron stars have a rotation power (L_{MDR}) to radio luminosity ratio (radio conversion efficiency) of $\sim 10^{-3}$, which is broadly consistent with the median value for conventional radio pulsars (see e.g., Figure 13 of Enoto et al. 2019), the FRB luminosity $\sim 10^{42}$ erg s^{-1} (see Chapter 1.2.2) can be reasonably accounted for.

As discussed in Totani (2013), the BNS merger rate density was thought to be sufficiently high ($\mathcal{R}_{\mathrm{BNS}} = 1.26 \times 10^4$ Gpc^{-3} yr^{-1}; Abbott et al. 2016) enough to accommodate FRBs ($\mathcal{R}_{\mathrm{FRB}} = 10^3$-$10^4$ Gpc^{-3} yr^{-1}, see Section 1.2.2). However, after the first GW detection of GW170817 from a binary neutron star merger, the BNS merger rate estimate went down to $\mathcal{R}_{\mathrm{BNS}} = 1540^{+3200}_{-1220}$ Gpc^{-3} yr^{-1} (Abbott et al. 2017), which is only marginally consistent with the FRB event rate density. Therefore, although both $\mathcal{R}_{\mathrm{FRB}}$ and $\mathcal{R}_{\mathrm{BNS}}$ should suffer from a large uncertainty, the event rate

in this model might not be high enough to account for all FRBs. As will be discussed in Chapter 2, if FRBs are produced after the merger by the activity of a stable remnant neutron star, then each remnant will produce multiple FRBs, which might significantly contribute to the FRB rate through BNS merger channel.

1.2.6   Galactic Baryon Census with FRB

In general, the observed total DM (Section 1.2.1 and 1.2.2) for an FRB DM_{FRB} can be roughly split into the four components as

$$DM_{FRB} = DM_{ISM} + DM_{halo} + DM_{IGM} + DM_{host}/(1 + z), \qquad (1.15)$$

where DM_{ISM} is the contribution from the warm ionized medium (WIM; $T \lesssim 10^4$ K) of ISM in the MW disk, DM_{halo} is that from the extended hot Galactic halo ($T \sim 10^6$–10^7 K), DM_{IGM} is that from IGM, and DM_{host} is that from the host galaxy including the local surrounding environment of the source in its rest frame at redshift z. In addition to the above four component, the DM contribution form intervening galaxy halos should be taken into account depending on the siteline configuration (McQuinn 2014; Shull & Danforth 2018; Prochaska & Neeleman 2018; Prochaska & Zheng 2019).

Breaking the degeneracies between different DM components appearing in the right-handed side of Equation (1.15) is a difficult task. We are still at a stage where it is only possible to estimate the rough contribution of Galactic electrons (i.e., DM_{ISM} and DM_{halo}) for the direction of an observed radio source, thereby obtaining a rough estimate of the maximum source distance through the analytic DM_{IGM}–z relation (Ioka 2003; Inoue 2004; Deng & Zhang 2014; McQuinn 2014; Shull & Danforth 2018; Li et al. 2019, for simulation study see also Dolag et al. 2015; Pol et al. 2019). For the ISM contribution, the warm electron density distribution models, such as NE2001 (Cordes & Lazio 2002, 2003) and YMW16 (Yao et al. 2017), have been developed and widely used, whereas less attention has been paid to the halo contribution (often ignored for the sake of simplicity), whose relative importance to the IGM contribution increases for nearby FRBs. This motivated theoretical investigations of the extended hot gas halo (Prochaska & Zheng 2019; Yamasaki & Totani 2020) in mind of FRBs (see Chapter 3).

Historically, on the other hand, the convincing evidence for the existence of such an extended hot gas halo around the MW and other galaxies (see e.g., Bregman 2007) have been provided mainly by X-ray (and UV) studies. The information about its spatial distribution and the total mass content is crucial to understand the cosmological *missing galactic baryon problem* (e.g., Fukugita & Peebles 2004; Shull et al.

2012). However, it is still challenging to obtain strong constraints on them due to the insufficient sensitivity of current X-ray observations. Since the key observable quantity of FRBs, the DM, traces the information of all baryons along the siteline, FRBs offer an entirely new approach to assess the baryon distribution in galaxies (McQuinn 2014; Prochaska & Zheng 2019).

An illustrative example that demonstrates the potential power of FRBs to probe the halo gas distribution was recently given by the localization of FRB 181112 to a host galaxy at $z = 0.48$ (Prochaska et al. 2019). As shown in the top right panel of Figure 1.3, the exceptional feature of this event is that the FRB sightline coincidentally passes the intervening massive galaxy (at $z = 0.37$) at an impact parameter $R_\perp \sim 29$ kpc from its center, which is well within the typical halo size (a few hundreds kpc) for such a massive galaxy ($M_\star \sim 10^{10}\,M_\odot$), allowing them to probe the halo of this foreground galaxy. Because an observation of this kind informs us of physical properties of diffuse gas in the halos of galaxies, which is ideally given back to the modeling of DM contribution from both the MW and host galaxies.

Another interesting avenue to test models for the MW hot gas halo is to utilize nearby FRBs with a small total DM of $\lesssim 100\,\mathrm{pc\,cm^{-3}}$ (e.g., FRB 171020 with $\mathrm{DM_{obs}} = 114\,\mathrm{pc\,cm^{-3}}$ found by ASKAP; Shannon et al. 2018; Mahony et al. 2018, FRB 110214 with $\mathrm{DM_{obs}} = 169\,\mathrm{pc\,cm^{-3}}$ by Parkes; Petroff et al. 2019 and FRB 181030.J1054+73 with $\mathrm{DM_{obs}} = 104\,\mathrm{pc\,cm^{-3}}$ by CHIME; CHIME/FRB Collaboration et al. 2019). Since such a low DM value is already comparable to the total Galactic DM contribution, it can set a strong limit on the existing models even without localizing its host galaxy. This perspective will be emphasized in Chapter 3 in line with the results obtained by the theoretical modeling of the Galactic halo DM.
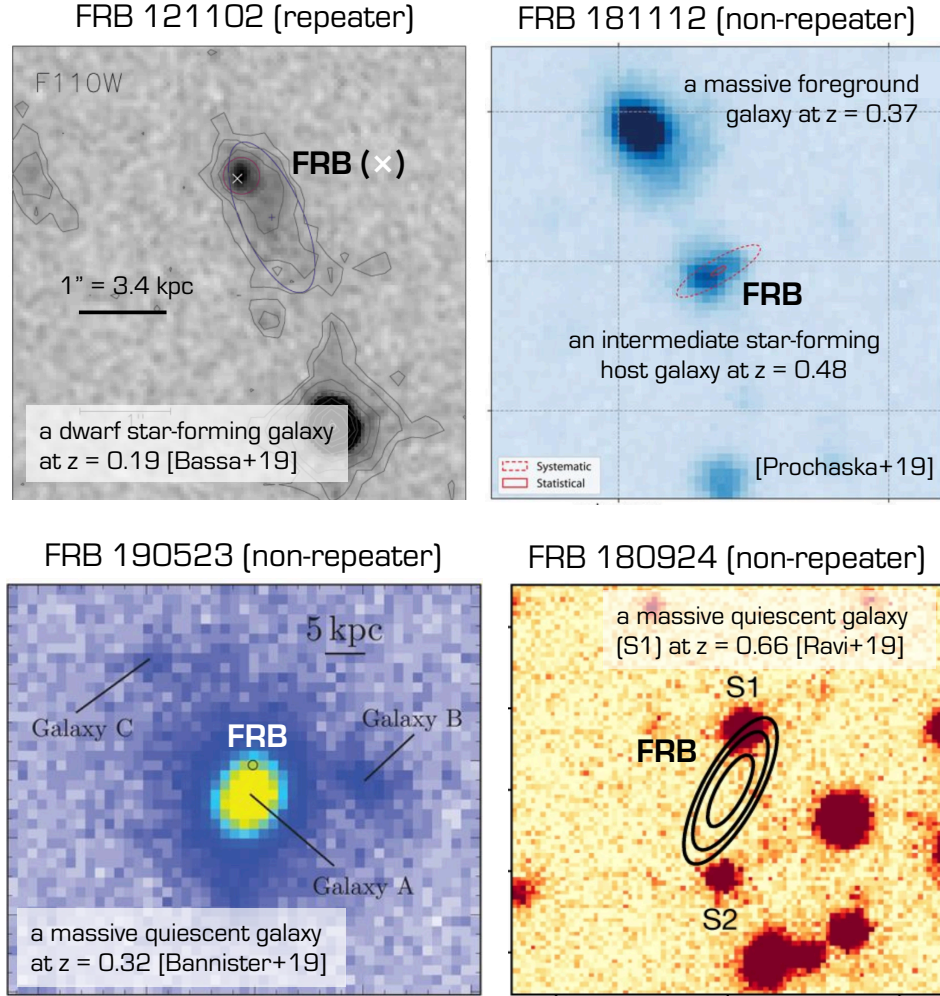
Figure 1.3: Images of galaxies that host FRBs 121102 (top left, Bassa et al. 2017, adapted by permission from the AAS), 181112 (top right, Prochaska et al. 2019), 190523 (bottom left, Bannister et al. 2019) and 180924 (bottom right, Ravi et al. 2019, adapted by permission from Springer Nature).

1.3 Magnetar Flares

1.3.1 Burst Phenomenology

Magnetars spend most of their time in a quiescent state, when they are observed as persistent quasi-thermal hot (typically ~ 0.3 keV) X-ray sources with thermal X-ray luminosity of

$$L_X = 4\pi R^2 \sigma_{\mathrm{SB}} T^4 \sim 1.0 \times 10^{35} \text{ erg s}^{-1} \left(\frac{R}{10^6 \text{ cm}}\right)^2 \left(\frac{kT}{0.3 \text{ keV}}\right)^4 , \qquad (1.16)$$

where an isotropic radiation from the stellar surface is assumed, and σ_{SB} represents the Stefan-Boltzmann constant. This far exceeding their spin-down luminosity

$$L_{\mathrm{sd}} = -I\Omega\dot{\Omega} = 3.2 \times 10^{33} \text{ erg s}^{-1} \left(\frac{P}{5 \text{ s}}\right)^3 \left(\frac{\dot{P}}{10^{-11} \text{ s s}^{-1}}\right) . \qquad (1.17)$$

Here $I = 10^{45}$ g cm^3 is the typical momentum of inertia of the star, and the timing properties (the neutron star spin period P and its time derivative $\dot{P}$) can be directly measured (but not always visible) via the pulsation of the persistent X-ray emission (e.g., Kouveliotou et al. 1998; Kouveliotou et al. 1999). Consequently, magnetars cannot be powered by rotational energy loss alone, but instead extract their power from the immense storage of magnetic energy (Thompson & Duncan 1996). In contrast, normal radio pulsars are believed to have their emission powered by the rotational energy loss. Transient magnetars are known to exhibit repeated and/or sporadic bursting activities[2], which span a wide range of luminosity. They can be roughly classified into following three classes:

- **Giant Flares** are the most intense flares with total power of $L_X = 10^{44}$–10^{47} erg s^{-1}. In general, a single giant flare consists of two successive components. Initially, a short ($\lesssim 1$ s) hard ($\sim$ MeV) spike appears, subsequently followed by a gradually decaying pulsating tail which shows intense pulsations over several minutes. The pulsations clearly visible during the decaying tail phase are at the spin period of the underlying neutron star (Kouveliotou et al. 1998; Kouveliotou et al. 1999). In terms of energetics, majority of the total

---

[2]Originally, they have been called "Soft Gamma Repeaters (SGRs)" and "Anomalous X-ray Pulsars (AXPs)", respectively for decades. Nowadays, however, the wide agreement that they are merely a different manifestation of the same object makes these terminologies slightly out-of-date (Kaspi & Beloborodov 2017).

energy released during the giant flare is carried away by the initial hard spike (over 10^{46} erg within ~ 0.2 s).

Kaspi & Beloborodov (2017) characterize the spectral evolution of giant flares as follows. The initial spike (at $t \lesssim 1$ s after the burst onset) shows a blackbody with temperature $k_B T \sim \mathcal{O}(100)$ keV. The subsequent spectrum is a combination of a low-temperature blackbody with temporary decreasing $k_B T \lesssim \mathcal{O}(10)$ keV and a non-thermal power-law component with index[3] of $\Gamma = 1$–2 extending up to 100 keV–1 MeV. The non-thermal spectral component gradually disappears and the soft-thermal component remains at $t \gtrsim 40$ s.

Giant flares are extremely rare; the only three giant flares from three different sources (SGR 0526−66 in 1979; Mazets et al. 1979, SGR 1900+14 in 1998; Hurley et al. 1999, and SGR 1806−20 in 2004; Hurley et al. 2005; Palmer et al. 2005) have been recorded in the last decades.

- **Intermediate Flares** are intermediate in duration (typically a few seconds) and luminosity ($L_X = 10^{41}$–10^{43} erg s^{-1}) between the short bursts (see below) and the giant flares. They are observed episodically from four different sources (SGR 1900+14; Mazets et al. 1999; Olive et al. 2004; Israel et al. 2008, SGR 1806−20; Göğüş et al. 2011, SGR 1627−41; Mazets et al. 1999, SGR J1550−5418; Mereghetti et al. 2009; Savchenko et al. 2010, SGR 1935+2154; Kozlova et al. 2016). Similarly to the giant flares, some brightest bursts exhibit a short hard spike, followed by a soft extended tail with 1-10 s duration, which occasionally shows pulsations at the spin period of underlying source (Savchenko et al. 2010). However, this picture is not necessarily valid for all bursts. Burst spectra are often fitted by multi-component spectral models comprising one or two blackbodies (e.g., Olive et al. 2004; Israel et al. 2008; Mereghetti et al. 2009; Göğüş et al. 2011).

- **Short Bursts** are the most frequent event among magnetar flares with typical duration of ~ 0.1 s, peak luminosity of $L_X = 10^{38}$–10^{41} erg s^{-1}, and soft thermal spectra. Similarly to the intermediate flares, the bursts spectra can be phenomenologiocally reproduced by multi-component different models containing at least one blackbody (see Enoto et al. 2019 and reference therein), which makes it difficult to distinguish different models (Kaspi & Beloborodov 2017).

In addition to the above, magnetars occasionally show transient enhancements (up to 10^{36} erg s^{-1} lasting months to years) of the persistent emission named "outbursts",

---

[3]Here the power-law index Γ is defined by $N(\epsilon) \propto \epsilon^{-\Gamma}$, where $N(\epsilon)$ is the spectral photon flux (the number of photons emitted per unit energy).

which often accompany a variety of anomalies in radiative behaviors. It is remarkable that the fluence of magnetar flares (from short bursts to giant flares) broadly follow a single power-law distribution ($N \propto \mathcal{F}^{-\alpha}$) with an index of $\alpha \sim 1-2$ (Cheng et al. 1996; Göğüş et al. 2001; Woods & Thompson 2006; Nakagawa et al. 2007). Those bursts with enormous energies can be readily afforded by the magnetic energy stored inside the magnetosphere:

$$
E_{\mathrm{B}} \gtrsim \frac{1}{8\pi} \int_R^\infty |\boldsymbol{B}|^2 dV \sim 3.4 \times 10^{47} \ \mathrm{erg} \ \left(\frac{B_p}{10^{15} \ \mathrm{G}}\right)^2 \left(\frac{R}{10^6 \ \mathrm{cm}}\right)^3 , \qquad (1.18)
$$

where a dipole field $B(r) = B_p(r/R)^{-3}$ is assumed and the magnetic energy inside the star is not included. To date, 29 magnetars (including 6 candidates) are reported and the more details and references are available at McGill Online Magnetar Catalogue[4] (Olausen & Kaspi 2014) and Magnetar Burst Library[5].

1.3.2 Burst Emission Mechanism

There is a wide consensus that the underlying cause of the bursting activities is the decay of the strong magnetic field in the star (Thompson & Duncan 1996; Woods & Thompson 2006). This makes the field deformed (twisted or sheared), which eventually leads to an unstable field configuration. Such a rapid reconfiguration of the magnetic field results in the dissipation of magnetic energy and the formation of a copious plasma, which are believed to be responsible for generating magnetar flares.

Burst Trigger

It remains still opaque how magnetar flares are triggered. There is a variety of models proposed for the trigger mechanism of flares; some of them are related to internal trigger mechanisms, such as a MHD instability inside the core or a fracture of the rigid stellar crust, leading to the sudden deposition of magnetic energy from stellar interior into magnetosphere (Thompson & Duncan 1995, 1996, 2001), while others to an external release of magnetic energy through magnetic reconnections (Lyutikov 2003; Gill & Heyl 2010; Yu 2012; Parfrey et al. 2013; Yu & Huang 2013).

---

[4]http://www.physics.mcgill.ca/~pulsar/magnetar/main.html (Last accessed on Jan. 30, 2020)

[5]http://staff.fnwi.uva.nl/a.l.watts/magnetar/mb.html (Last accessed on Jan. 30, 2020)

Burst Radiation

One of the keys to understanding the nature of flare emissions is the formation of an optically-thick electron-positron ($e^{\pm}$) photon (γ) plasma dubbed "fireball". A huge and sudden energy release into the magnetosphere triggered by either the solid crust failure or magnetic reconnections generates strong Alfvén waves, which will quickly cascade into smaller scales and dissipate (Thompson & Blaes 1998). Thompson & Duncan (1995) argued that such dissipation would immediately result in the formation of a fireball. The most common pair creation process is the photon-photon interaction: $\gamma + \gamma' \rightleftharpoons e^+ + e^-$. Under a strong magnetic field, the field feeds its energy to a photon, which also leads to the creation of pairs: $\gamma + B \rightarrow e^+ + e^-$. Moreover, the above two processes can be efficiently catalyzed by providing additional seed photons via photon splitting expected in a strong magnetic field: $\gamma + B \rightarrow \gamma' + \gamma''$. Consequently, the interior of the fireball becomes extremely optically-thick and the radiation dominates the total pressure.

Thompson & Duncan (1995) argued that the initial spike of the giant flare should be produced by the relativistic outflow arising from fireball. Since the initial radiation pressure of such an energetic fireball should far exceed the magnetic pressure, the fireball is expected to expand at the relativistic speed. As a consequence, the pair creation inside the expanding plasma becomes inefficient and thus thermalized photons start to escape from the photosphere, which would be observed as a main spike (see also Chapter 4). The discovery of a bright radio afterglow from the historical giant flare from SGR 1806−20 on 2004 December 27 also supports the existence of such a plasma outflow launched during the giant flare (e.g., Gaensler et al. 2005; Cameron et al. 2005; Granot et al. 2006; Gelfand et al. 2005).

Right after the initial hard spike, the remaining population of fireball plasma around the star is confined onto the stellar surface (so-called "trapped fireball"), and gradually evaporates by radiating a quasi-thermal emission from its thin surface layer (Thompson & Duncan 2001). This is possible *if* the radiation pressure of the fireball is a fraction of the local magnetic pressure, which is likely the case for most flares. Although the trapped fireball model can qualitatively account for the temporal characteristics of the extended tail of giant flares (Feroci et al. 2001), theoretical models expected from the trapped fireball (e.g., Lyubarsky 2002) cannot fully explain the observed flare spectra (e.g., Olive et al. 2004; Israel et al. 2008, see Chapter 5; Figure 5.1). The hard non-pulsating spectral component visible only during the early extended tail phase ($t \lesssim 40$ s) requires an additional explanation, such as emission from the heated corona around the trapped fireball (Thompson & Duncan 2001).

It is tempting to speculate that a similar dissipation process may well operate

in lesser flares. However, observations suggest that the rate of energy dissipation for smaller bursts may be relatively lower (e.g., Göğüş et al. 2001). Therefore, whether the fireball successfully forms in the smaller bursts is not yet clear due to the lack of theoretical developments (Watts et al. 2010; Kaspi & Beloborodov 2017). One of the alternative models to explain the thermal spectra of less-energetic bursts is the formation of "hot sopts" on the neutron star surface by the bombardment of $e^{\pm}$ plasma (Yamasaki et al. 2019), which will be presented in Chapter 4.

1.3.3   High-B Radio Pulsars as Quiescent Magnetars?

The bursting/flaring activity in X-ray and gamma-ray bands has been preferentially found in sources with $B_p > B_Q \sim 4.4 \times 10^{13}$ G, with exceptions of SGR 0418+5729 ($B_p \sim 6 \times 10^{12}$ G; Rea et al. 2010) and Swift J1822.3$-$1606 ($B_p \sim 2.7 \times 10^{13}$ G; Rea et al. 2012), and such an activity may be correlated with magnetic field as is likely the case for quiescent emissions from magnetars. It has been argued by Kaspi & McLaughlin (2005) that if the magnetic field is a key prerequisite for such a bursting activity, there is such a possibility of magnetar-like bursts from high-B radio pulsars[6], that has later proven to be correct (Gavriil et al. 2008; Archibald et al. 2016, 2017).

Meanwhile, four magnetars are thus far known to exhibit transient radio pulsations during the X-ray outbursts, although temporal and spectral characteristics of magnetar radio emission is quite different from that for canonical radio pulsars. In the curious case of the first detected radio-emitting magnetar XTE J1810$-$197, the radio flux density clearly correlates with the spin-down power (P) over years (Camilo et al. 2016). This implies that the radio emission in magnetars might be also powered by rotation as ordinary radio pulsars are, although theories remain inconclusive whether and how radio emission in magnetars is produced (e.g.,Beloborodov 2009; Szary et al. 2015).

In short, a handful of observations all strongly suggest that there should be a link between the two populations: "classic" magnetars and high-B radio pulsars. One of the most ideal and unique targets to investigate such a relationship is the high-B radio pulsar PSR J1119–6127. Archibald et al. (2017) reported the detection of three short bursts from this source on 30 August 2016. This alone is an intriguing finding that confirms the magnetar-like activity from a high-B radio pulsar. More interestingly, they also found that these short bursts temporally coincide with the disappearance of persistent radio emissions (see Figure 1.4). This underlying connection will be

---

[6]Although "high-B radio pulsar" is not a well-defined (established) concept, it often refers to a rotation-powered radio pulsar with $B_p \gtrsim 10^{13}$ G in the literature (e.g., Enoto et al. 2019).

Observations of PSR J119-6127 [Archibald+17]

a — XMM & NuSTAR 0.5-20 keV — Short bursts

e — Parkes 1.4 GHz — Radio suppression for O(100 s)
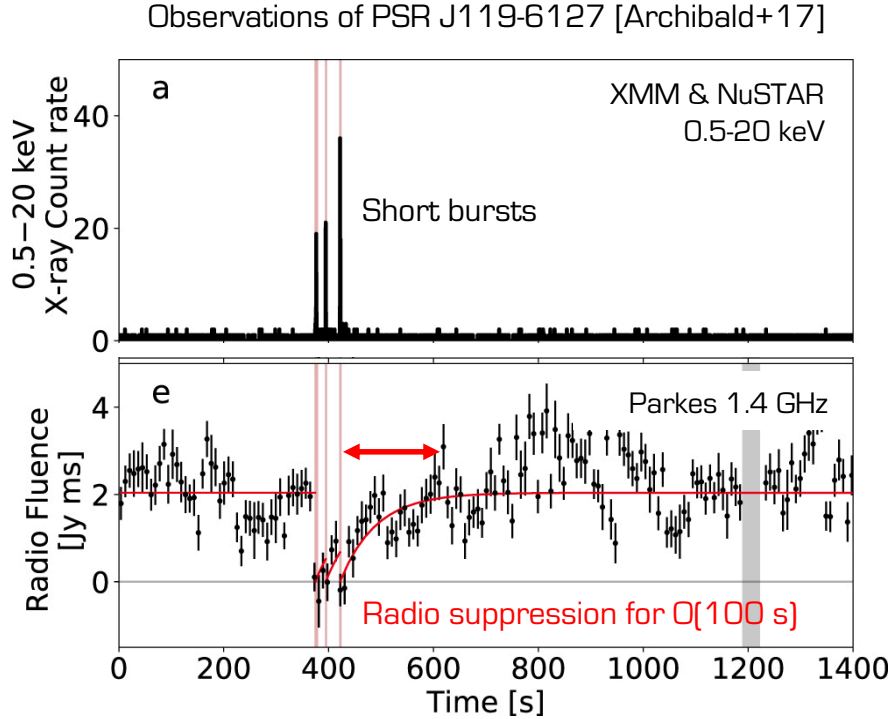
Figure 1.4: The simultaneous X-ray and 1.4 GHz radio observations of PSR J1119–6127 (Archibald et al. 2017, reproduced with permission by AAS). (a) The combined XMM and NuSTAR 0.5–20 keV count rate over time. (e) The total pulsed radio fluence over time. The red line shows the best-fit exponential recovery model for the persistent radio emission with a timescale of $\sim \mathcal{O}(100\,\mathrm{s})$. Note that the time delay due to dispersion has been corrected for the observed dispersion measure of 706.5(3) pc cm^{-3}. The red vertical lines indicate the duration of the three X-ray bursts.

explored in Chapter 4 with particular emphasis on the radio disappearance at the time of magnetar flares.

1.4 This Dissertation

1.4.1 Outline

This thesis is organized into four main chapters, most of which have been adopted from previously published papers (except for Chapter 5). In the first part, the origin

of FRBs is probed in terms of BNS mergers in Chapter 2, and the Galactic halo DM model for FRB is developed in Chapter 3 for future application. The second half of this thesis is related to magnetar flares. In Chapter 4, we explore the relationship between magnetars and radio pulsars. This chapter is motivated by the disappearance of radio pulsations observed simultaneously with the onset of magnetar-like short bursts (Archibald et al. 2017). We consider the instantaneous expansion of the fireball plasma as a plausible mechanism that can suppress the radio emission. We also proposed a qualitative explanation for the short burst. In Chapter 5, we model the X-ray spectra of energetic magnetar flares. A summary of the outcome of this work is provided in Chapter 6.

1.4.2   Contribution of Authors

I would like to acknowledge the contributions of my coauthors:

- **Chapter 2 (Yamasaki, Totani, Kiuchi, 2018)**
  Tomonori Totani suggested investigating the simulation. The BNS merger simulations used in this work was fully performed by Kenta Kiuchi who provided me with data, helped my analysis a lot. The guiding of Tomonori Totani was crucial to formulate our model and to interpret the simulation results.

- **Chapter 3 (Yamasaki, Totani, 2020)** Tomonori Totani played an important roll in the formulation of the model proposed in this chapter.

- **Chapter 4 (Yamasaki, Kisaka, Terasawa, Enoto, 2019)** Shota Kisaka suggested the basic idea of the model. Toshio Terasawa and Teruaki Enoto provided useful comments and suggestions on the manuscript.

- **Chapter 5 (Yamasaki, Lyubarsky, Granot, Göğüş, 2020, in prep)**
  Yuri Lyubarsky played a crucial role in guiding the project. Jonathan Granot significantly provided useful comments and suggestions on the early manuscript, which improved the formulation of the model proposed in this chapter. Ersin Göğüş performed the spectral and temporal analysis of the SGR 1900+14 bursts.

Part I

Fast Radio Bursts

Chapter 2

Repeating and Non-repeating FRBs from BNS Mergers

This chapter was adapted from a paper published in the Publications of the Astronomical Society of Japan called "*Repeating and Non-repeating Fast Radio Bursts from Binary Neutron Star Mergers*" (Yamasaki et al. 2018). It might be worth noting that this paper was written and submitted before the discovery of the first binary neutron star merger event GW 170817 by LIGO/VIRGO (Abbott et al. 2017). Our model explicitly predicts repeating and non-repeating FRBs from early-type/passive host galaxies, which had not been observed when the paper was published. In order to make the motivation for this work clear, we have left the language as it is, even though some parts of it (e.g., Section 2.1) appear to be obsolete in contrast to the recent unfolding discoveries introduced in Section 1.2.4.

2.1   Introduction

The enigmatic millisecond-duration radio transients, the fast radio bursts (FRBs) were first discovered by Lorimer et al. (2007), then confirmed with additional four bursts by Thornton et al. (2013), and now it is an intensive field of research in astronomy. About 20 FRBs have been reported to date (Petroff et al. 2016), but their origin and physical mechanism still remain mysterious. Their dispersion measures (DMs) $\mathrm{DM} \equiv \int n_e dl = 300\text{–}1500$ pc cm^{-3} (Petroff et al. 2016) are much larger than those expected for objects in the Milky Way, and a cosmological distance scale of $z \sim 1$ is inferred if the dominant contribution to DMs is from electrons in ionized intergalactic medium (IGM). Counterparts in other wavelengths (e.g., Yamasaki et al.

2016) or host galaxies have not yet been detected in most cases. Keane et al. (2016) reported a radio afterglow of FRB 150418 and identification of an elliptical host galaxy at $z = 0.492$, but there is a claim that the radio afterglow may be an AGN activity that is not related to the FRB (Williams & Berger 2016). Further radio monitoring with high resolution will be needed to settle these disputes (Bassa et al. 2016).

The majority of FRBs do not show evidence for repetition, in spite of the fact that some of them have been intensively monitored to search possible repeating bursts (Lorimer et al. 2007; Petroff et al. 2015). The only exception is FRB 121102, which is the only FRB discovered by the Arecibo observatory (Spitler et al. 2014) and later found to repeat (Spitler et al. 2016; Scholz et al. 2016). The repetition allowed sub-arcsecond localization and the first unambiguous identification of the host galaxy (Chatterjee et al. 2017; Marcote et al. 2017; Tendulkar et al. 2017; Bassa et al. 2017). FRB 121102 was discovered by a high-sensitivity search of Arecibo, and its burst flux (~ 0.02–0.3 Jy) is smaller than that of other FRBs (~ 0.2–2 Jy) mostly detected by the Parkes observatory (Spitler et al. 2016). If we take into account the distance ($z = 0.193$ for FRB 121102 and the DM-inferred redshifts of $z = 0.5$–1.0 for other FRBs), the absolute luminosity of FRB 121102 is two orders of magnitude smaller than other FRBs. This implies a possibility that FRB 121102 belongs to a different population from other FRBs.

In this chapter we consider mergers of binary neutron stars (BNS, i.e., a binary of two neutron stars) as a possible source of FRBs. Apparently non-repeating FRBs can be explained by radio emission at the time of merger. The exceptionally bright FRB 150807 shows a small amount of rotation measure (RM) implying negligible magnetization in the circum-burst plasma (Ravi et al. 2016), which may favor the clean environment expected around BNS mergers. There is still a large uncertainty in both FRB and BNS merger rates, but the FRB event rate is close to the high end of the plausible range of BNS merger rate, 1×10^4 Gpc^{-3} yr^{-1} (Abadie et al. 2010). The latest upper bound on the BNS merger rate by LIGO (Abbott et al. 2016) is also close to this: 1.26×10^4 Gpc^{-3} yr^{-1} (90% C.L.), indicating that a BNS merger should be detected soon if non-repeating FRBs are produced by BNS mergers[1]. The observed FRB flux can be explained by magnetic braking luminosity and a radio conversion efficiency similar to pulsars (Totani 2013). Wang et al. (2016) investigated radio emission based on the unipolar inductor model (Piro 2012; Lai 2012, see also Hansen & Lyutikov 2001).

---

[1]Shortly after the submission of this work, the first gravitational wave event GW170817 from a binary neutron star merger was reported, and the BNS merger rate is estimated to be 1540^{+3200}_{-1220} Gpc^{-3} yr^{-1} (Abbott et al. 2017), see also Section 1.2.5.

A theoretical concern of the BNS merger scenario is, however, that the environment around the merger would be polluted by matter dynamically expelled during the merger process, which may prohibit the radio signal to be transmitted. The first aim of this work is to investigate this issue by using a numerical-relativity simulation of a BNS merger. We will compare the rise of rotation power that may produce an FRB and the timing of dynamical matter ejection, and examine whether there is a time window in which an FRB is produced and transmitted to an observer.

It is obvious that a radio burst at the time of a BNS merger cannot explain the repeating FRB 121102. A young neutron star possibly with strong magnetic field (i.e., a magnetar) is then popularly discussed as the source of FRB 121102, which is surrounded by a pulsar wind nebula (PWN) that is responsible for the observed persistent radio emission. Therefore, a core-collapse supernova, especially in the class of superluminous supernovae (SLSNe), is discussed as the progenitor of FRB 121102, because formation of a rapidly rotating magnetar is one of the possible explanations for the extreme SLSN luminosity, and because of the host galaxy properties (dwarf and low metallicity; Kashiyama & Murase 2017; Metzger et al. 2017).

However, a fraction of BNS mergers may leave a massive neutron star which is indefinitely stable or temporarily stable by a rotational support (e.g., Gao et al. 2013; Metzger & Piro 2014; Piro et al. 2017). The fraction strongly depends on the equation of state (EOS) for nuclear matter as well as neutron star mass distribution, which may be either negligible or the majority[2]. The latter requires that EOS is stiff enough to support a spherical neutron star with the maximum mass of $\gtrsim 2.7\,M_\odot$. Such remnant neutron stars should be rapidly spinning by the large angular momentum of the original binary, and their magnetic field can be amplified by the merger process (e.g., Kiuchi et al. 2014), possibly to the magnetar level. The ejecta mass from a BNS merger is much smaller than SLSNe, making the transmission of radio signal easier. The estimated event rate of BNS mergers is higher than that of SLSNe by 1–2 orders of magnitude (Abadie et al. 2010; Quimby et al. 2013), and hence the production rate of rapidly rotating neutron stars by BNS mergers may be higher than that by SLSNe.

The second aim of this work is to examine merger-remnant neutron stars as the origin of repeating FRBs like FRB 121102. We make order-of-magnitude estimates of various physical quantities and compare with the observational constraints for FRB 121102. We then propose a unified scenario for repeating and non-repeating FRBs

---

[2]After the detection of GW 170817, there have been several attempts to constrain the nature of the merger remnant and the maximum mass of neutron stars, but an unambiguous conclusion has not yet been obtained and the fraction of merger events leaving a long-lived neutron star is still highly uncertain.

from BNS mergers. Non-repeating and bright FRBs are produced as a single catastrophic event at the time of merger, while repeating and faint FRBs are produced by young and rapidly rotating neutron stars left after BNS mergers. We then present an FRB rate evolution model including these two populations, and examine the relative detection rate as a function of search sensitivity. This may give a hint to explain the fact that the only repeating FRB was detected as the faintest FRB.

The outline of this chapter is as follows. In Section 2.2, we describe the details of the BNS simulation used in this work. We then examine ejecta formation by the merger and discuss the possibility of producing a non-repeating FRB in Section 2.3. The merger-remnant neutron star scenario for repeating FRBs is compared with the available observational constraints in Section 2.4, and the FRB rate evolution model is presented in Section 2.5. Conclusions will be given with some discussions in Section 2.6. The adopted cosmological parameters for a flat universe are $H_0 = 67.8 \text{ km s}^{-1} \text{ Mpc}^{-1}$, $\Omega_\text{M} = 0.308$, and $\Omega_\Lambda = 0.692$ (Planck Collaboration et al. 2016).

2.2 BNS Merger Simulation

Methods of the BNS merger simulation used in this work are presented in Kiuchi et al. (2014). The simulation employs the moving puncture gauge, and the spatial coordinates (denoted by xyz) are defined so that they asymptotically become the Cartesian coordinate system towards a point at infinity from the center. The simulation is performed in a cubic box and the centers of two neutron stars are located in the $z = 0$ plane. A reflection symmetry with respect to the $z = 0$ plane is assumed. A fixed mesh-refinement algorithm with seven levels is adopted for the spatial coordinates to resolve the wide dynamic range of a BNS merger. The outermost (i.e., the first level) box has $469 \times 469 \times 235$ grids in x-y-z, with a grid size of ~ 9.6 km. (the number of z-direction grids is only for the upper half of the cube). In the second level, the box of half size (i.e., $1/8$ in volume) with the same box center is simulated with a two times finer grid size, while the grid number is the same. This is repeated in the same way to the seventh level where the mesh size is $1/2^6$ of the first level (~ 150 m).

We employ the H4 EOS of Glendenning & Moszkowski (1991), with which the maximum mass of neutron stars is $2.03 \, M_\odot$. Two neutron stars have the same ADM mass of $1.35 \, M_\odot$ when they are isolated. This simulation does not include magnetic fields; there are no known BNS simulations in which dynamical ejecta mass is significantly changed by the effects of magnetic fields. The simulation starts with an orbital angular velocity $\Omega_\text{orb} \sim 1.7 \times 10^3 \text{ s}^{-1}$ and a binary separation of ~ 50 km, and the merger occurs after several in-spiral orbits. The simulation finishes at 15 ms

after the merger, and at that time the merged hypermassive neutron star (HMNS) is still rotationally supported against a gravitational collapse.

Our purpose is to investigate the time evolutionary properties of matter ejected to outer regions, and we do not have to examine quantitatively the general relativistic effects that are important around the merger center. Therefore in this work we present physical quantities assuming that the simulation grids are on the classical Cartesian coordinate system throughout the box, and the simulation time grids are on the classical time coordinate.

For computational reasons, numerical simulations of a BNS merger usually set an artificial atmosphere around stars, and in our simulation the density of atmosphere is 10^3 g cm^{-3} within $r \leq 70$ km and it decreases as $\propto r^{-3}$ in outer regions, where r is the radius from the simulation center. The central density of the atmosphere is 10^{12} times smaller than the nuclear matter density found inside the neutron stars. Furthermore, the minimum density that the simulation can reliably resolve is $\sim 10^8$ g cm^{-3}. Therefore we consider only matter whose density is higher than the threshold value, $\rho_{\rm th} = 10^8$ g cm^{-3}, when calculating the rest-mass column density of ejecta. Even if calculated column density allows transmission of FRB signals, we cannot exclude a possibility that lower density material than $\rho_{\rm th}$ absorbs FRB signals. However, our results shown below indicate that the matter density rapidly drops at a certain radius from the HMNS, and material of $\rho < \rho_{\rm th}$ would unlikely affect our main conclusions.

2.3   Circum-merger Environment and FRB Visibility

2.3.1   Orbital Evolution and Neutron Star Spin-up

Figure 4.1 presents time snapshots of density contours and velocity fields of the simulation, spanning from 0.71 ms before to 4.26 ms after the merger, where the merger time $t_{\rm merge}$ is defined as the time when the density peaks of the two neutron stars merge into one.

FRBs are expected to be generated by rotation, either the orbital motion of the two neutron stars or spins of individual neutron stars. The rotation angular velocity of the orbital motion ($\Omega_{\rm orb}$) and that of the individual neutron star spin ($\Omega_{\rm spin}$) are shown as a function of time in Figure 2.2. For this calculation, we first calculate the angular velocity at each grid from the rotation-direction component of fluid velocity,

as

$$\Omega(\mathbf{r}) = \frac{1}{|\mathbf{r}_{xy}|} \mathbf{v} \cdot \left(\frac{\mathbf{n}_z \times \mathbf{r}}{|\mathbf{n}_z \times \mathbf{r}|} \right) \ , \tag{2.1}$$

where $\mathbf{r}$ is the position vector measured from the rotation center on the $z = 0$ plane, $\mathbf{v}$ the three velocity of fluid, $\mathbf{n}_z$ the unit spatial vector to the z direction, and $\mathbf{r}_{xy}$ the projection of $\mathbf{r}$ onto the xy plane. Then the average rotation velocity is calculated as the mass-weighted mean:

$$\Omega_{\mathrm{av}} = \frac{\int \Omega(\mathbf{r})\rho(\mathbf{r})d\mathbf{r}}{\int \rho(\mathbf{r})d\mathbf{r}} \ , \tag{2.2}$$

where ρ is the rest-mass density. The orbital rotation velocity Ω_{orb} is simply calculated by setting the rotation center at the center of the simulation box and integration over the whole simulation box. The spin of each neutron star Ω_{spin} is calculated by setting the rotation center at the density peak of one of the two neutron stars. For the integration region of Ω_{spin}, we separate the simulation box into two by a plane including the simulation box center and perpendicular to the line connecting the two centers of the neutron stars. Then the integration of Ω_{spin} is performed only over the half side including the neutron star considered. As expected, Ω_{spin} of the two neutron stars are almost the same, and it becomes the same as Ω_{orb} after the merger.

Though the calculation of Ω_{orb} is completely Newtonian, we compare this with the angular frequency of the dominant quadrupole mode of gravitational wave radiation (Ω_{gw}) calculated from the simulation by a relativistic method using the Weyl scalar (Yamamoto et al. 2008). We then confirmed that the expected relation, $\Omega_{\mathrm{orb}} = \Omega_{\mathrm{gw}}/2$, holds within a 10% accuracy.

It can be seen in Figure 2.2 that Ω_{orb} gradually increases to the merger, but Ω_{spin} suddenly rises up at ~0.5 ms before the merger. Our simulation does not include viscosity, and hence a tidal lock by viscosity does not occur. A tidal lock is not expected to occur even if viscosity is taken into account (Bildsten & Cutler 1992). After the sharp rise, Ω_{spin} is almost the same as Ω_{orb}, and energy for FRBs can be extracted by the spin of magnetic fields of the merging star with a rotation period of about 1 ms. A coherent dipole magnetic field may be that of neutron stars before the merger, or may be formed during the merger process. The energy loss rate of the dipole emission formula is proportional to Ω_{spin}^4, and hence the chance of producing an FRB rapidly increases at ~0.5 ms before the merger.
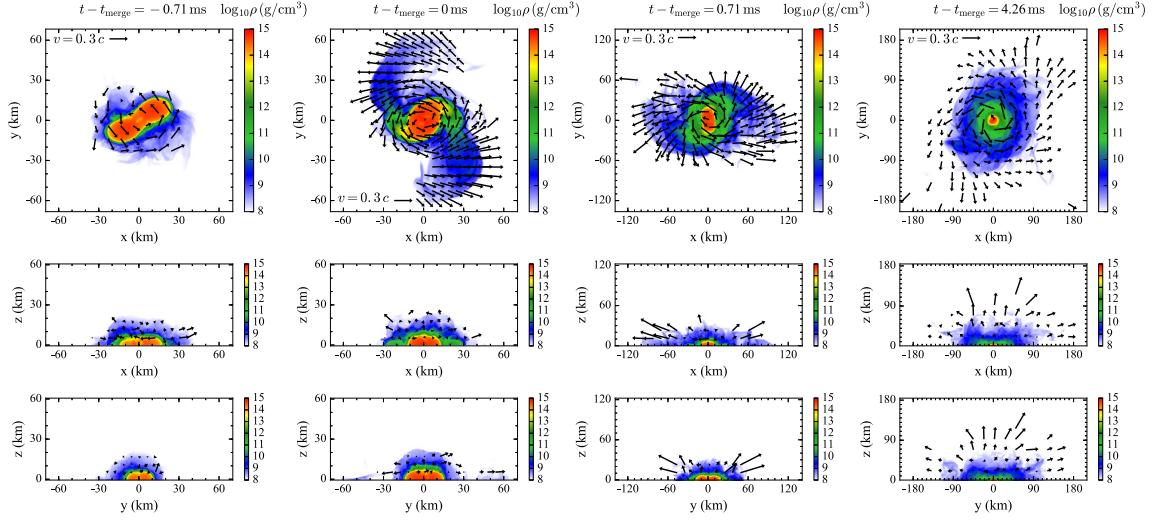
Figure 2.1: Time snapshots of density contours for the binary neutron star merger simulation used in this work, in the xyz coordinates which are approximately the classical Cartesian coordinates. The velocity fields are also shown by black vectors.
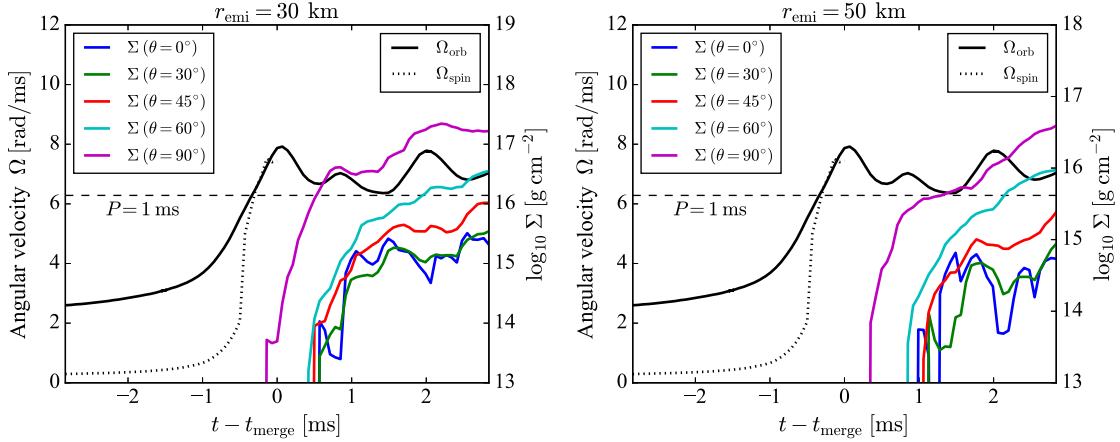
Figure 2.2: Evolution of angular velocities of orbital motion ($\Omega_{\rm orb}$) and spin of each neutron star ($\Omega_{\rm spin}$) are shown by solid and dotted black curves, respectively (see the left-hand ordinate for labels). The horizontal dashed line indicates Ω corresponding to a rotation period of 1 ms. Color curves show rest-mass column density Σ in regions of $r > r_{\rm emi}$ towards the direction polar angle θ from the z axis, for several values of θ. The left and right panels are for $r_{\rm emi} = 30$ and 50 km, respectively, and a median about the azimuth angle ϕ is taken for Σ.

2.3.2   Ejecta Formation

Next we consider ejecta distribution. Figure 2.2 shows the time evolution of the rest-mass column density,

$$\Sigma(\theta, \phi \, ; \, r_{\mathrm{emi}}) = \int_{r_{\mathrm{emi}}}^{\infty} \rho(\mathbf{r}) dr \, , \tag{2.3}$$

which is integrated over the radial direction from the simulation center excluding the inner region of $r < r_{\mathrm{emi}}$, where r, θ, ϕ are spherical coordinates. As mentioned in Section 2.2, low density grids with $\rho < \rho_{\mathrm{th}}$ are excluded from this calculation. We show the cases of $r_{\mathrm{emi}} = 30$ and 50 km, for several values of polar angle θ from the z direction. The light cylinder radius becomes $\sim$50 km for a rotation period of 1 ms, and hence it is reasonable to expect that FRB radiation occurs at 30–50 km from the center. The column density also depends on the azimuth angle ϕ, and here we take the median of $\Sigma(\phi_i)$ to show a typical column density, where ϕ_i is the 360 grids in $\phi = 0$–2π to calculate Σ. (We avoid a simple mean because it is biased when a high density ejecta exist into one direction, though its covering fraction on the sky is small.)

This figure shows that Σ significantly increases 0–1 ms after the merger. Ejecta to the equatorial directions ($\theta \sim 90°$) appear earlier, because dynamical mass ejection is driven first by tidal force, and then shock heated components are ejected to the polar direction from the HMNS (Sekiguchi et al. 2015). Since the minimum density resolved in the simulation is 10^8 g cm^{-3}, column density of $\Sigma \lesssim 10^{14}$ g cm^{-2} cannot be resolved on the scale of 30–50 km. Once Σ becomes larger than this, there is no chance for an FRB emission to escape, because the optical depth of electron scattering is many orders of magnitudes larger than unity. The rapid increase of Σ by many orders of magnitude occurs at about 1 ms after the merger to most directions, implying that the environment before this is similar to that of isolated neutron stars.

Figure 2.3 shows time snapshots of radial profiles of rest-mass density and velocity. Here, again the median is plotted about the azimuth angle. Except for the equatorial ($\theta = 90°$) direction, the density sharply drops from 10^{14} to $\sim 10^9$ g cm^{-3} at the surface of newly born HMNS. An extended tail of the density profile at $\rho \sim 10^8$ g cm^{-3} is seen, but it may be an artifact because this low density is close to the simulation resolution. Well-resolved ejecta with $\rho \gg 10^8$ g cm^{-3} and positive radial velocity are seen only into the equatorial direction at the time of merger, and those into other directions appear a few ms after the merger. The ejecta velocity is at most 0.1–0.2 c, and it takes about 1 ms for such an ejecta to expand into the outer regions of $r > r_{\mathrm{emi}} \sim 30$–50 km.

These results imply that a significant ejecta formation and expansion to the scale of 30–50 km occurs about 1 ms after the merging neutron stars start to rapidly spin. Therefore there is a short time window of $t - t_{\mathrm{merge}} \sim -0.5$ to 0.5 ms in which the ejecta is not yet formed but the magneto-rotational energy production rate is sufficiently high to produce an FRB emission. This also gives a possible explanation for the observed ~ 1 ms duration of non-repeating FRBs.

2.4 Repeating FRBs from a Post-merger Remnant

2.4.1 Formation of the Remnant Neutron Star and Its Consequence

Hereafter we consider the case that a BNS merger leaves a merged neutron star that is indefinitely stable without rotation or rotationally supported for a time scale longer than the repeating FRB lifetime. Its initial spin period is $P_i = 2\pi/\Omega_i \sim 1$ ms, mass $\sim 2.6\, M_\odot$, and radius $R \sim 15$ km. If there is a loss of rotation energy by e.g. gravitational wave emission, initial rotation period may be larger. The rotational energy of the star is

$$E_{\mathrm{rot}} = \frac{1}{2} I \Omega_i^2 \approx 9.2 \times 10^{52} \quad \mathrm{erg}, \tag{2.4}$$

where I is the momentum of inertia of the star. The spin-down timescale by magnetic breaking is given as

$$t_{\mathrm{sd}} = \frac{3 c^3 I P_i^2}{4 \pi^2 B_*^2 R^6} \sim 2.7\, B_{12.5}^{-2} \quad \mathrm{yrs}, \tag{2.5}$$

where $B_{12.5} = B_*/(10^{12.5}\ \mathrm{G})$ is the strength at the star surface. We adopt $10^{12.5}$ G as a reference value that is typical for isolated pulsars, but the magnetic field strength may be enhanced by the merger process to $B \gtrsim 10^{13}$ G as suggested by numerical simulations (e.g., Kiuchi et al. 2014), and in such a case t_{sd} could be smaller.[3]

Consider ejecta mass $M_{\mathrm{ej}} = 10^{-2}\, M_\odot$ and velocity $\beta_{\mathrm{ej},0} = v_{\mathrm{ej},0}/c = 0.1$, which are within the typical ranges for a BNS merger. The dynamical ejecta mass decreases

---

[3]It should be noted that the rotation energy E_{rot} is quickly converted into pulsar wind if magnetic field is as strong as magnetars (10^{15} G) and the neutron star survives longer than the spin-down time. This is excluded for the particular case of GW 170817, because such a large energy is not observed. However, a low magnetic field of $\lesssim 10^{12.5}$ G is not excluded because of the longer spin-down time.
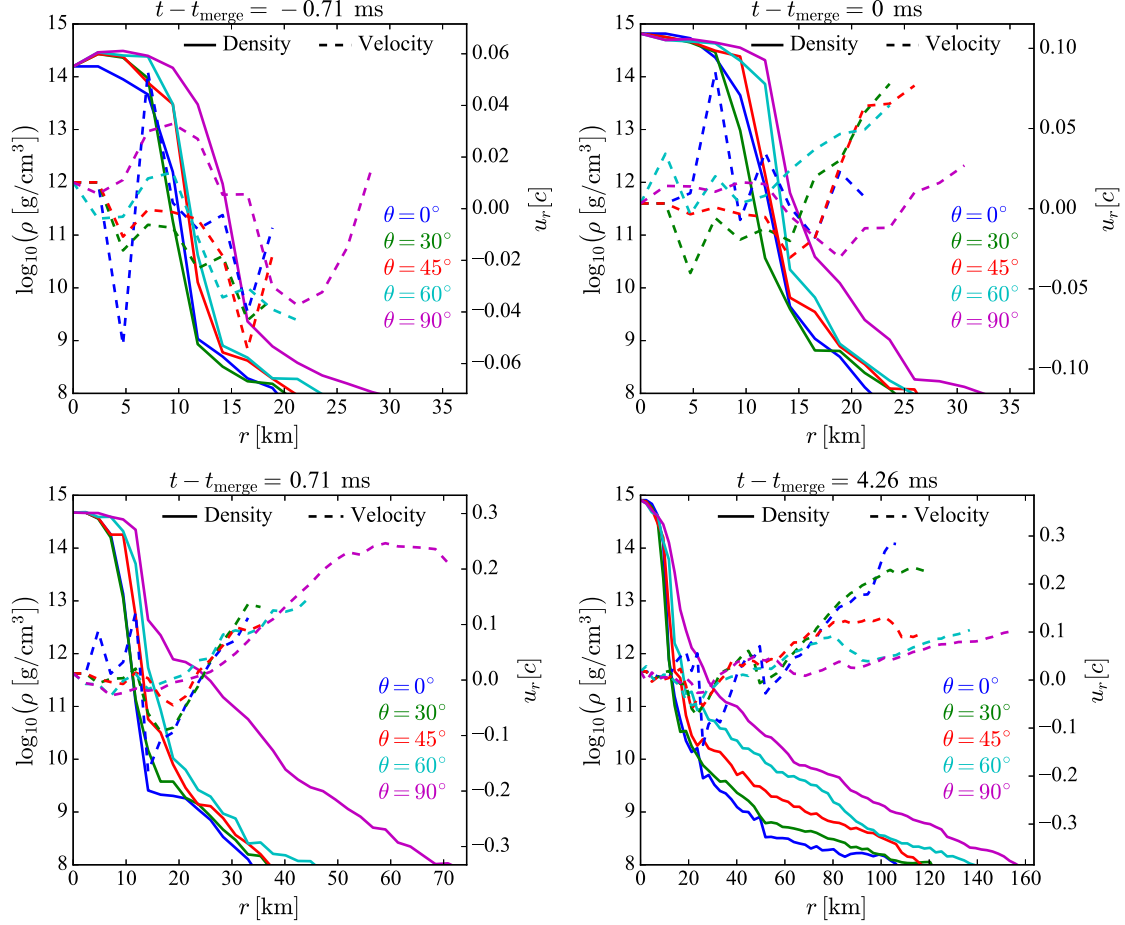
Figure 2.3: Time snapshots (corresponding to Figure 4.1) of radial profiles of rest-mass density (solid colored lines) and radial fluid velocity (dashed colored lines), for several values of polar angle θ from the z axis. These quantities are the median about the azimuthal angle ϕ. The radius is measured from the merger center.

with stiffer EOS (Hotokezaka et al. 2013), and the ejecta mass may be enhanced by disk wind (Shibata et al. 2017). The ejecta kinetic energy would be changed when the rotation energy of the newly born massive neutron star is injected into the merger ejecta in the form of pulsar wind, within a time scale of t_{sd}. Assuming that an energy of E_{rot} is injected as relativistic particles or Poynting flux at a radius $r_{\mathrm{inj}} = v_{\mathrm{ej},0}\, t_{\mathrm{sd}}$, we can estimate the accelerated velocity and internal energy of ejecta (pulsar wind nebula) to be $\beta_{\mathrm{PWN}} = 0.85$ and $U_{\mathrm{inj}} = 4.0 \times 10^{52}$ erg, respectively, from energy and momentum conservation. This bulk motion speed is mildly relativistic, but we ignore the relativistic effect for simplicity in the order-of-magnitude analysis. We assume that ejecta is freely expanding except for the velocity change at $r = r_{\mathrm{inj}}$. The expanding ejecta would be decelerated by interstellar medium (ISM) when a comparable ISM has been swept up, but this effect can be ignored if we consider evolution before the deceleration time $t_{\mathrm{dec}} \sim 15\; M_{\mathrm{ej},-2}^{1/3}\; n_{\mathrm{ISM},-3}^{-1/3}\; \beta_{\mathrm{PWN}}^{-1}$ yr, where $n_{\mathrm{ISM}} = 10^{-3}\; n_{\mathrm{ISM},-3}$ cm^{-3} is the ISM density. In this work we do not consider the interaction with ISM for simplicity.

The energy injection by pulsar wind would heat up the ejecta matter and also generate magnetic fields in the ejecta, B_{ej}. We assume that a fraction ϵ_{B} of the internal energy density $u_{\mathrm{inj}} = U_{\mathrm{inj}}/(4\pi r_{\mathrm{inj}}^3/3)$ is converted into magnetic fields at the time of energy injection, as $B_{\mathrm{ej,inj}}^2/(8\pi) \approx \epsilon_{\mathrm{B}}\, u_{\mathrm{inj}}$. After the injection B_{ej} evolves by adiabatic expansion and conserved magnetic flux, i.e., $B_{\mathrm{ej}} = B_{\mathrm{ej,inj}}(r/r_{\mathrm{inj}})^{-2}$. This reduces to

$$B_{\mathrm{ej}} = 5.6 \times 10^{-2}\; \epsilon_{\mathrm{B},-2}^{1/2}\; B_{12.5}^{-1}\; \beta_{\mathrm{PWN}}^{-2}\; t_{\mathrm{yr}}^{-2}\;\; \mathrm{G}\;, \tag{2.6}$$

where $t_{\mathrm{age}} = t_{\mathrm{yr}}$ yr is the time elapsed from the merger, and we use $\epsilon_{\mathrm{B},-2} = \epsilon_{\mathrm{B}}/10^{-2}$ that is inferred from the magnetization parameter of the Crab nebula (Kennel & Coroniti 1984). Here we assumed the shell thickness $\Delta r \sim r$ to calculate u_{inj}. The dependence on B_* appears by t_{sd} (smaller r_{inj} for stronger B_*). Note that we made an approximation of $t_{\mathrm{age}} \sim r/v_{\mathrm{PWN}}$, which is exactly valid only when $t_{\mathrm{age}} \gg t_{\mathrm{sd}}$. This does not affect the conclusions in this section from order-of-magnitude estimates. This magnetic field strength will be used in the next section to discuss the energetics of synchrotron radiation and rotation measure.

2.4.2 Comparison with FRB 121102 Observations

Free-free absorption

First we estimate the time scale for the ejecta to become transparent to the free-free absorption of radio signals. Before energy injection by pulsar wind, the opacity becomes less than unity at a time

$$
\begin{aligned}
t_{\mathrm{tr}}^{\mathrm{ff}} \quad \sim \quad & 4.2 \,(Z/26)\, f_{\mathrm{ion}}^{1/5}\, \nu_9^{-2/5} T_{\mathrm{e},3}^{-3/10} \\
& \times\, M_{\mathrm{ej},-2}^{2/5}\, (\beta_{\mathrm{ej},0}/0.1)^{-6/5} \ \mathrm{yr}
\end{aligned}
\tag{2.7}
$$

after the merger, where $\nu_9 \equiv \nu/(\mathrm{GHz})$ is the frequency of the radio signal, f_{ion} is the ionization fraction, Z the mean atomic number of matter in ejecta, and $T_{e,3} = T_e/(10^3\ \mathrm{K})$ the temperature of ejecta. Here we used $\beta_{\mathrm{ej},0} = 0.1$ as the ejecta velocity before the energy injection by the pulsar wind, which is valid when $t_{\mathrm{sd}} > t_{\mathrm{tr}}^{\mathrm{ff}}$. Therefore this $t_{\mathrm{tr}}^{\mathrm{ff}}$ is a conservative upper-limit, and $t_{\mathrm{tr}}^{\mathrm{ff}}$ can be smaller by the accelerated ejecta speed when $t_{\mathrm{sd}} < t_{\mathrm{tr}}^{\mathrm{ff}}$. After the energy injection by pulsar wind, electrons in the ejecta may have relativistic energies if energy conversion from ions to electrons is efficient. Since the free-free opacity of relativistic electrons is reduced compared with non-relativistic ones (Kumar et al. 2017), the environment would be transparent after the energy injection.

Synchrotron self-absorption

High energy electrons and positrons produced as the pulsar wind would form a nebular after interaction with the ejecta. Synchrotron self-absorption by these electrons and positrons may prohibit early radio signal to transmit (Murase et al. 2016; Yang et al. 2016). Following Murase et al. (2016), we assume the injected electron energy spectrum of the nebula to be a broken power-law, $dN_{\mathrm{inj}}/d\gamma_e \propto \gamma^{-q}$ with $q = q_1 \,(< 2)$ at $\gamma_{\mathrm{m}} \leq \gamma_e \leq \gamma_{\mathrm{b}}$ and $q = q_2 \,(> 2)$ at $\gamma_{\mathrm{b}} \leq \gamma_e \leq \gamma_{\mathrm{M}}$, where γ_e is the Lorentz factor of injected electrons. This is motivated by observations of Galactic pulsar wind nebulae. The break Lorentz factor is typically $\gamma_{\mathrm{b}} \sim 10^4$–$10^6$, and $\gamma_m \sim 100 \ll \gamma_b \ll \gamma_M$.

At sufficiently late times, the radiative cooling is governed by the synchrotron radiation with its timescale

$$
t_{\mathrm{syn}} = \frac{3\,m_e c}{4\sigma_{\mathrm{T}}\,U_{\mathrm{B}}\,\gamma_e} \sim 10^{12}\ \mathrm{s}\ \gamma_e^{-1}\, B_{12.5}^2\, \beta_{\mathrm{PWN}}^4\, t_{\mathrm{yr}}^4\, \epsilon_{B,-2}^{-1}\ ,
\tag{2.8}
$$

where $U_{\mathrm{B}} = B_{\mathrm{ej}}^2/(8\pi)$ is the magnetic energy density at a given time. Equating

the synchrotron cooling time given by Equation (2.8) with the dynamical timescale $t_{\rm dyn} \sim r/v_{\rm PWN}$, the cooling break Lorentz factor is found as

$$\gamma_c = 3.2 \times 10^4 \ B_{12.5}^2 \, \beta_{\rm PWN}^4 \, t_{\rm yr}^3 \, \epsilon_{B,-2}^{-1} \ . \tag{2.9}$$

Therefore, electrons are in the slow cooling regime ($\gamma_m \ll \gamma_c$) for typical timescales of interest ($\gtrsim$ yr) due to the large velocity of the ejecta, which is in contrast to the fast cooling case expected for the SN scenario (e.g., Kashiyama & Murase 2017). The injection electron spectrum is then conserved at $\gamma_e < \gamma_c$, and the synchrotron absorption is dominated by electrons with $\gamma_m < \gamma_e < \gamma_c$. The spectrum is normalized so that a fraction $\epsilon_e \sim 1$ of the total internal energy $U \ [= U_{\rm inj}(r/r_{\rm inj})^{-1}]$ is carried by relativistic electrons and positrons, since it is generally believed that the pulsar wind is dominated by $e^\pm$ (Kennel & Coroniti 1984; Tanaka & Takahara 2013). We numerically calculated the absorption optical depth

$$\tau_\nu^{\rm sa} = \frac{r}{8\pi m_{\rm e} c \, \nu^2} \int_{\gamma_{\rm m}}^{\gamma_{\rm M}} \frac{1}{\gamma_e^2} \frac{d}{d\gamma_e} \left[\gamma_e^2 P_{\rm s}(\nu, \gamma_e) \right] \, n_e(\gamma_e) \, d\gamma_e \ , \tag{2.10}$$

where $P_{\rm s}(\nu, \gamma_e)$ is the synchrotron emitting power and $n_e(\gamma_e)$ is the emergent electron energy spectrum in the steady state which is the same as the injected spectrum at $\gamma_e < \gamma_c$. For a parameter range of $q_1 = 1$–1.5, we find that the nebula becomes transparent to 1 GHz radio emission at $t_{\rm tr}^{\rm sa} \sim 1$ yr. See Appendix A for the details of assumption and calculation.

Therefore the environment around a BNS merger would become transparent for a repeating FRB with a time scale of order years, though the uncertainty is more than one order of magnitude. After the appearance of a repeating FRB for an observer, the activity would decrease with time if the neutron star is already in the spin-down phase. Then the highest activity of a repeating FRB would last on a time scale similar to that of the appearance, i.e., of order years. It should be noted that the spin down time would become shorter if B_* is stronger, but a repeater FRB can be formed even in the case of $t_{\rm sd} < t_{\rm tr}$, if the remnant neutron star exists on a time scale longer than $t_{\rm sd}$ and FRBs are produced using e.g. magnetic field energy.

The persistent radio source

The source size of the persistent radio emission from FRB 121102 is limited to $\lesssim 0.7$ pc (Marcote et al. 2017), and this gives an upper limit on the age $t_{\rm age}$ of this source. Assuming that the ejecta is expanding with $\beta_{\rm PWN}$ from the beginning (i.e., $t_{\rm sd} \ll t_{\rm age}$),

we find

$$t_{\mathrm{age}} < 2.7 \left(\frac{\beta_{\mathrm{PWN}}}{0.85} \right)^{-1} \; \mathrm{yr}, \tag{2.11}$$

which is comparable with the minimum age ~ 5 yr of FRB 121102. Therefore, expanding size evolution of the persistent radio source may be observed in the near future, though a realistic morphology must be considered for a more quantitative prediction. The source size may be smaller if β_{PWN} is smaller by a larger ejecta mass, or t_{sd} is comparable to the age. Another possibility to make the size smaller is a confinement by dense ISM.

The observed luminosity of the persistent radio emission from FRB 121102 (1.9×10^{39} erg s^{-1} at 10 GHz, Chatterjee et al. 2017) can be used to estimate the minimum electron energy emitting synchrotron radiation. Following the formulation of Kashiyama & Murase (2017) and the magnetic field strength estimated above, we find the minimum electron energy as $\sim 1.2 \times 10^{49} t_{\mathrm{yr}}^3 \, \epsilon_{B,-2}^{-1/2} \, \beta_{\mathrm{PWN}}^{3/2}$ erg. This is sufficiently smaller than the maximum energy available by the rotation of the merged neutron star, $E_{\mathrm{rot}} \sim 10^{53}$ erg, if the age is less than ~ 10 yrs. Even if there is a significant loss of rotation energy at the stage of the merger, the rotation energy is still sufficiently larger if $P_i \lesssim 10$ msec.

Dispersion and rotation measures

Next we consider dispersion measure (DM) around the remnant neutron star. DM of ejecta matter (after energy injection by the pulsar wind) using the standard formula becomes

$$\mathrm{DM}_{\mathrm{ej}} \approx 5.2 \times 10^{-1} \; M_{\mathrm{ej},-2} \, f_{\mathrm{ion}} \, \beta_{\mathrm{PWN}}^{-2} \, t_{\mathrm{yr}}^{-2} \; \mathrm{pc} \; \mathrm{cm}^{-3}. \tag{2.12}$$

The DM contribution from the host galaxy of FRB 121102 is estimated as $\mathrm{DM}_{\mathrm{host}} < 55$–225 pc cm^{-3} (Tendulkar et al. 2017; Kokubo et al. 2017), and the DM changing rate is constrained as < 2 pc cm^{-3} yr^{-1} (Piro 2016). These constraints can be easily met in our model if the age is larger than ~ 1 yr.

Though rotation measure (RM) is not yet measured for the repeating FRB 121102,[4] it has been observed for some FRBs. Masui et al. (2015) found a rela-

---

[4]After the submission of this work, a high ($\sim 10^5$ rad m^{-2}) and variable (10% decrease on a half year) rotation measure of FRB 121102 has been reported (Michilli et al. 2018), which is a few orders of magnitude higher than our plausible estimate in eq. (2.13). However, the high RM

tively large RM contribution from the host galaxy ($\gtrsim 160$ rad m^{-2}) of FRB 110523, which favors a dense and magnetized environment like star forming regions or supernova remnants. On the other hand, small or negligible RMs from the host galaxy and IGM were observed for the exceptionally bright FRB 150807 ($\lesssim 2$ rad m^{-2}, Ravi et al. 2016) and FRB 150215 (< 25 rad m^{-2}, Petroff et al. 2017), which favor a cleaner environment.

We can calculate RM of the ejecta matter in our model assuming that the magnetic field is ordered along the line of sight to an observer, which becomes

$$
\begin{aligned}
\mathrm{RM_{ej}} \quad \sim \quad & 1.2 \times 10^4 \quad \epsilon_{\mathrm{B},-2}^{1/2} \, B_{12.5}^{-1} \\
& \times \, M_{\mathrm{ej},-2} \, f_{\mathrm{ion}} \, \beta_{\mathrm{PWN}}^{-4} \, t_{\mathrm{yr}}^{-4} \quad \mathrm{rad \ m^{-2}} \quad .
\end{aligned}
\tag{2.13}
$$

This can be consistent even with the low RMs of FRB 150807 and FRB 150215 if we take $t_{\mathrm{yr}} \sim 10$, though dependence on model parameters is large. Therefore it is possible that these apparently non-repeating FRBs are also remnant neutron stars after a BNS merger, and repeating has not yet been detected because of a search sensitivity and/or limited monitoring time. Of course, another possibility is that these FRBs were produced at the time of a BNS merger, for which we expect even smaller RM.

It should be noted that here we used the standard classical formulae for DM and RM calculations. However, electrons may have relativistic energy after the energy injection from pulsar wind. The relativistic effect reduces both DM and RM (Shcherbakov 2008), and hence this does not affect the consistency between our model and observations.

2.4.3   Comparison with the Supernova Scenarios

Supernovae, especially the class of SLSNe, have been proposed as the progenitor of a young and rapidly rotating neutron star to produce repeating FRBs (Kashiyama & Murase 2017; Metzger et al. 2017; Beloborodov 2017; Dai et al. 2017). Here we compare the SN scenario with our BNS merger scenario. Besides the event rate difference between SLSNe and BNS mergers mentioned in Section 2.1, a large difference is the ejecta mass of SLSNe that is much larger than that of BNS mergers. Here we discuss using typical parameter values of $M_{\mathrm{ej},1} \equiv M_{\mathrm{ej}}/(10 M_\odot)$ and $v_{\mathrm{ej},9} \equiv v_{\mathrm{ej}}/(10^9 \ \mathrm{cm/s})$

---

may be explained if we consider a highly clumpy density structure (e.g., dense nebula filaments), which would enhance magnetic fields. The observed short variability timescale may favor a young progenitor ($\lesssim 10$ yr). Further investigation should be done as future work.

(i.e., an explosion energy of 10^{52} erg) for a SLSN (Metzger et al. 2017). The difference would be smaller in the case of ultra-stripped SLSNe ($M_{\mathrm{ej}} \sim 0.1 M_{\odot}$, Kashiyama & Murase 2017), although the event rate and the ejecta mass are highly dependent on how to interpret the light curve of rapidly rising transients (e.g., Drout et al. 2014; Arcavi et al. 2016).

Because of the larger mass ejecta and slower speed, it would take a longer time for the environment to become transparent for radio signals. The previous studies about the SLSN scenario then considered a time scale of 10–100 yrs as the age of FRB 121102. Assuming that the spin-down time of a newly born neutron star is less than ~ 10 yrs, the rotation energy is decreasing with time and hence we expect that the BNS scenario has a larger available rotation energy to produce FRBs than the SLSN scenario. Therefore even if the event rate of the two populations is the same, we expect brighter and more active FRBs from neutron stars produced by a BNS merger, and hence a higher chance of detection.

DM, source size and energetics of persistent radio emission in the SLSN scenario have been discussed in the previous studies, and they are consistent with observational constraints of FRB 121102. Compared with the BNS merger scenario, DM is larger and hence DM variability would be stronger, while the persistent radio source size is smaller and hence the size upper limit is more easily met. RM in the SLSN scenario has not been discussed in the previous studies, and from our formulations we find

$$
\begin{aligned}
\mathrm{RM_{ej}} \quad \sim \quad & 1.7 \times 10^{11} \; \epsilon_{\mathrm{B},-2}^{1/2} \, B_{14}^{-1} \\
& \times M_{\mathrm{ej},1} \, f_{\mathrm{ion}} \, v_{\mathrm{ej},9}^{-4} \, t_{\mathrm{yr}}^{-4} \quad \mathrm{rad \; m^{-2}} \; .
\end{aligned}
\tag{2.14}
$$

Here we assumed that the ejecta has an internal energy of $\sim 10^{52}$ erg at the time of the energy injection from pulsar wind, but the velocity is not accelerated because the original supernova kinetic energy is comparable with the energy injected by the pulsar wind. This RM is much larger than the maximum RM found for FRB 110523, even if we assume an age of 100 yrs and a strong stellar magnetic field of $B_* = 10^{14}$ G. This implies that all FRBs cannot be a young neutron star produced by a SLSN, unless the net magnetization is largely cancelled by small scale fluctuations of magnetic field directions.

2.5 Rate Evolution of Repeating and Non-repeating FRBs

2.5.1 Cosmic BNS Merger Rate Evolution

In order to discuss the FRB detection rate as a function of a search sensitivity, we first determine the cosmic BNS merger rate as a function of redshift. The comoving volumetric BNS merger rate at a redshift z [corresponding to a cosmic time $t(z)$] is a convolution of the comoving star formation rate density Ψ_{SFR} and the delay time distribution (DTD) of BNS mergers from star formation:

$$\mathcal{R}_{\mathrm{BNS}}(z) = \int_0^{t(z)} \Psi_{\mathrm{SFR}}(t - \tau) f_{\mathrm{D}}(\tau) d\tau \ , \tag{2.15}$$

where τ is the delay time (the time elapsed from the formation of a stellar binary to the BNS merger), and $f_{\mathrm{D}}(\tau)$ is DTD normalized per unit mass of star formation.

We use a functional form of cosmic star formation history,

$$\Psi_{\mathrm{SFR}}(z) = 0.015 \, \frac{(1+z)^{2.7}}{1 + [(1+z)/2.9]^{5.6}} \ M_\odot \, \mathrm{yr}^{-1} \, \mathrm{Mpc}^{-3} \tag{2.16}$$

in $0 < z < 8$ derived by Madau & Dickinson (2014). DTD of compact object mergers generally becomes $f_D \propto \tau^{-\alpha}$ with $\alpha \sim 1$, when it is controlled by gravitational wave radiation as in the cases of BNS or binary white dwarfs (e.g., Totani et al. 2008). Here we set $f_D \propto \tau^{-1}$ at $\tau \geq \tau_{\mathrm{min}}$ and zero otherwise, with $\tau_{\mathrm{min}} = 10$ Myr, which is roughly consistent with that calculated by Belczynski et al. (2006) using a binary population synthesis model. The BNS merger rate is normalized as $\mathcal{R}_{\mathrm{BNS}}(0) = 1 \times 10^4 \, \mathrm{Gpc}^{-3} \, \mathrm{yr}^{-1}$, which is the "plausible optimistic" rate estimate for local BNS mergers by Abadie et al. (2010). It should be noted that the following results on the ratio of repeating to non-repeating FRB rates is not affected by this normalization. The calculated $\Psi_{\mathrm{SFR}}(z)$ and $\mathcal{R}_{\mathrm{BNS}}(z)$ are shown in Figure 2.4.

2.5.2 Repeating versus Non-repeating FRB Detection Rates

The FRB luminosity function is hardly known, and for simplicity we adopt the standard candle approximation both for the non-repeating and repeating populations. There is a large variation in radio spectral index of FRBs (e.g., Spitler et al. 2014), and here we simply assume $L_\nu \propto \nu^0$, and hence $S_\nu \propto (1+z) D_L(z)^{-2}$, where L_ν is

the absolute FRB luminosity per unit frequency, S_ν the observed flux density, and D_L the luminosity distance. The absolute luminosity is fixed so that $S_\nu = 1.0$ Jy at $z = 1$ for non-repeating FRBs based on fluxes and DMs observed by Parkes, while $S_\nu = 0.1$ Jy at $z = 0.19$ for repeating FRBs based on the case of FRB 121102.

Then the all-sky rates for single (i.e., non-repeating) FRBs (N_{sFRB}) and repeating FRBs (N_{rFRB}) that are brighter than a limiting flux density $S_{\nu,\mathrm{lim}}$ are calculated using $\mathcal{R}_{\mathrm{BNS}}(z)$ as:

$$N_{\mathrm{s}FRB}(> S_{\nu,\mathrm{lim}}) = \int_0^{z_{\mathrm{s}}} dz \frac{dV}{dz} \frac{\mathcal{R}_{\mathrm{BNS}}}{1+z} , \qquad (2.17)$$

$$N_{\mathrm{rFRB}}(> S_{\nu,\mathrm{lim}}) = \int_0^{z_{\mathrm{r}}} dz \frac{dV}{dz} \frac{\mathcal{R}_{\mathrm{BNS}}}{1+z} f_r N_r , \qquad (2.18)$$

where dV/dz is the comoving volume element per unit redshift, $(1+z)^{-1}$ is the cosmo-logical time dilation factor, and $z_s(S_{\nu,\mathrm{lim}})$ and $z_r(S_{\nu,\mathrm{lim}})$ are the redshifts corresponding to single and repeating FRBs with a flux $S_{\nu,\mathrm{lim}}$, respectively. In the case of repeating FRBs, the formation probability of a repeating FRB source after a BNS merger (f_r) and the number of repeating bursts during its lifetime (N_r) are multiplied. Here we assumed that all BNS mergers produce a non-repeating FRB at the time of merger, and assumed the same beaming factor for the two populations. These assumptions also affect the ratio $N_{\mathrm{sFRB}}/N_{\mathrm{rFRB}}$, and uncertainties about these can be included in the parameter f_r.

No repeating FRBs have been detected by Parkes, and it implies

$$\left. \frac{N_{\mathrm{rFRB}}}{N_{\mathrm{sFRB}}} \right|_{S_{\nu,\mathrm{lim}}=1 \ \mathrm{Jy}} \lesssim 0.1, \qquad (2.19)$$

which translates into an upper limit on the product $f_r N_r \lesssim 400$. The parameter N_r can be written as $N_r = \tau_{\mathrm{lt}} \, k \, \zeta$, where τ_{lt} is the lifetime of a repeating FRB source, k the repeat rate during the active FRB phase, and ζ the active duty cycle. Observationally inferred values are $k \sim 3 \ \mathrm{day}^{-1}$ and $\zeta \sim 0.3$ (Nicholl et al. 2017), and we get $f_r \tau_{\mathrm{lt}} \lesssim 1.2$ yr. In order for the lifetime to be consistent with that discussed in Chapter 2.4, a weak constraint of $f_r \lesssim 0.1$ is obtained, though there is a large dependence on model parameters.

In Figure 2.5, a $\log N$–$\log S$ plot for sFRBs and rFRBs is shown. Both popu-lations show the trend of $N(> S_{\nu,\mathrm{lim}}) \propto S_{\nu,\mathrm{lim}}^{-1.5}$ in the bright flux limit, as expected when cosmological effects are negligible. The curve of non-repeating FRBs becomes flat at $S_{\nu,\mathrm{lim}} \lesssim 200$ mJy by the cosmological effects (cosmic volume and the BNS rate evolution), but such a behavior is not seen for repeating FRBs because their redshifts

are lower and hence cosmological effects are small. The ratio $N_{\rm rFRB}/N_{\rm sFRB}$ is also plotted in Figure 2.5. This rapidly increases with improving sensitivity at $S_{\nu,\rm lim} \lesssim 1$ Jy, because the cosmological effects work only on non-repeating FRBs. This gives a possible explanation for the fact that the only repeating FRB was discovered by Arecibo that has a better flux sensitivity than Parkes.

2.6   Discussion and Conclusions

In this chapter, we investigated BNS mergers as a possible origin of both repeating and non-repeating FRBs.

Non-repeating and bright FRBs mostly detected by Parkes may be produced at the time of a BNS merger, but the environment around the merger may be polluted by dynamical ejecta, which would prohibit radio signals to propagate. We therefore investigated the BNS merger environment using a general-relativistic hydrodynamical simulation. It was found that a significant mass ejection that can be resolved by the current simulation occurs about 1 ms after the merger, and hence there is a time window of about 1 ms in which the magneto-rotational energy production rate has become the maximum to produce an FRB emission and the environment is not yet polluted. This also gives a possible explanation for the observed short duration ($\lesssim 1$ ms) of non-repeating FRBs.

A fraction of BNS mergers may leave a stable remnant neutron star, and such an object may produce faint and repeating FRBs like FRB 121102 detected by Arecibo, after the environment becomes clear for radio signals. We showed that the environment becomes clear on a time scale of order years, and after that FRB activities would become weaker on a similar time scale by the pulsar spin-down. The persistent radio emission of FRB 121102 can be explained by a pulsar wind nebula energized by the remnant neutron star. The expected radio source size is marginally consistent with the observational upper limit, implying that a source size evolution may be observed in the future. DM expected for the radio emitting nebula is smaller than the observational estimate of DM from the host galaxy of FRB 121102, and the nebula RM is not significantly larger than those measured in some FRBs. Compared with the supernova scenario for young neutron stars to produce repeater FRBs, the BNS merger scenario predicts a shorter time scale for the appearance after the merger (or supernova) and a shorter active lifetime as a repeating FRB source. The environment around the young neutron star is more transparent with smaller DM and RM, while the source size of persistent radio emission is larger. Especially, the expected large RM implies that the supernova scenario cannot be applied to all FRBs because some

FRBs show small RM.

We then constructed an FRB rate evolution model including these two popula-
tions. Requiring that the discovery rate of a repeating FRB source is less than 10%
of that for non-repeating FRBs at the search sensitivity of Parkes, the lifetime of
repeating FRB sources $\tau_{\rm lt}$ is constrained as $f_r \tau_{\rm lt} \lesssim 1.2$ yr, where f_r is the fraction
of BNS mergers leaving a remnant neutron star that is stable on a time scale longer
than $\tau_{\rm lt}$. Then we obtain $f_r \lesssim 0.1$ from $\tau_{\rm lt} \sim 1$–10 yrs obtained in Section 2.4, which
is not a strong constraint because it is an order-of-magnitude estimate. Since non-
repeating FRBs are brighter and hence more distant at a given sensitivity, the slope
of FRB source counts ($\log N$-$\log S$) is flatter than that of repeating FRBs. Therefore
the relative ratio of repeating to non-repeating FRB source counts should rapidly
increase with improving search flux sensitivity. This gives a possible explanation to
the fact that the only repeating FRB 121102 was discovered by the most sensitive
search using Arecibo, and such a trend can be confirmed with more FRBs detected
in the future. It should be noted that this trend is expected even if repeating FRBs
originate from supernovae rather than BNS mergers.

In addition to some predictions already mentioned above, the following predic-
tions can be made based on our hypothesis. Originating from BNS mergers, both
repeating and non-repeating FRBs should be found both in star-forming and elliptical
galaxies. FRB 121102 was found in a dwarf star forming galaxy with low metallic-
ity, and this may favor the SLSN scenario. However, a strong conclusion cannot be
derived from only one event; BNS mergers should also occur in such galaxies. It is
plausible that FRBs showing negligible RM (FRBs 150807 and 150215) occurred in
quiescent galaxies such as elliptical galaxies.

If non-repeating FRBs are produced at the time of BNS mergers, the BNS
merger rate must be close to the high end of the possible range discussed in the
literature, and gravitational wave from a BNS merger should be detected soon by
LIGO/VIRGO/KAGRA. A non-repeating FRB can in principle be detected coinci-
dentally with gravitational wave from a BNS merger, but a wide-field FRB search
covering a considerable fraction of all sky will be the key. If the location of a BNS
merger detected by gravitational wave is accurately determined by electromagnetic
wave counterparts, there is a good chance of discovering repeating FRBs ~ 1–10 years
after the merger, though the probability of leaving a stable neutron star depends on
EOS of nuclear matter. A repeating FRB may also be found 1-10 years after a
non-repeating FRB or a short gamma-ray burst (GRB), but they are generally more
distant than BNS mergers detected by gravitational waves and hence repeating FRBs
may be too faint to detect.

Though the fraction of BNS mergers leaving a stable neutron star is currently highly uncertain, gravitational wave observations may constrain the nuclear matter EOS in the near future (Lattimer & Prakash 2007). Such constraints would be useful to examine the validity of our scenario for repeating FRBs. If a repeating FRB is detected after a BNS merger, it would be an unambiguous proof of a surviving remnant neutron star, which would give an independent constraint on EOS. Another possible signature of a surviving neutron star is a persistent radio emission from the pulsar wind nebula like FRB 121102, or that from interaction between ejecta and ISM (Horesh et al. 2016).

Finally, we comment on some intriguing recent observational studies. Ofek (2017) reported 11 luminous radio sources in nearby ($<$ 108 Mpc) galaxies with offsets from the nucleus, whose luminosities are similar to the persistent source associated with FRB 121102. The number density of these is $\sim 5 \times 10^{-5}$ Mpc^{-3}. Using the typical lifetime of repeating FRBs (10 yrs) in our hypothesis, a birth rate of $\sim 5 \times 10^3$ yr^{-1} Gpc^{-3} is inferred, which is interestingly similar to the non-repeating FRB rate and the high end of the possible BNS merger rate range. Furthermore, 2 of the 11 sources are in the galaxies of old stellar population (passive and elliptical), which cannot be produced from young stellar populations.

Perley et al. (2017) reported a new radio source (Cygnus A-2) at a projected offset of 460 pc from the nucleus of Cygnus A ($z = 0.056$), which was detected in 2015 but was not present until 1997. The origin of this source is not yet clear, and a repeating FRB was not discussed as a possible origin in Perley et al. (2017). However we noticed that the unusually bright radio luminosity as a supernova, $\nu L_\nu \approx 6 \times 10^{39}$ erg s^{-1}, is interestingly similar (within a factor of a few) to that of the persistent radio emission of FRB 121102, while Cygnus A-2 is about three times closer to us. The luminosity and the appearance time scale imply that Cygnus A-2 may also be a pulsar wind nebula produced by a BNS merger remnant, and a radio monitoring of this may lead to a discovery of another repeating FRB source.
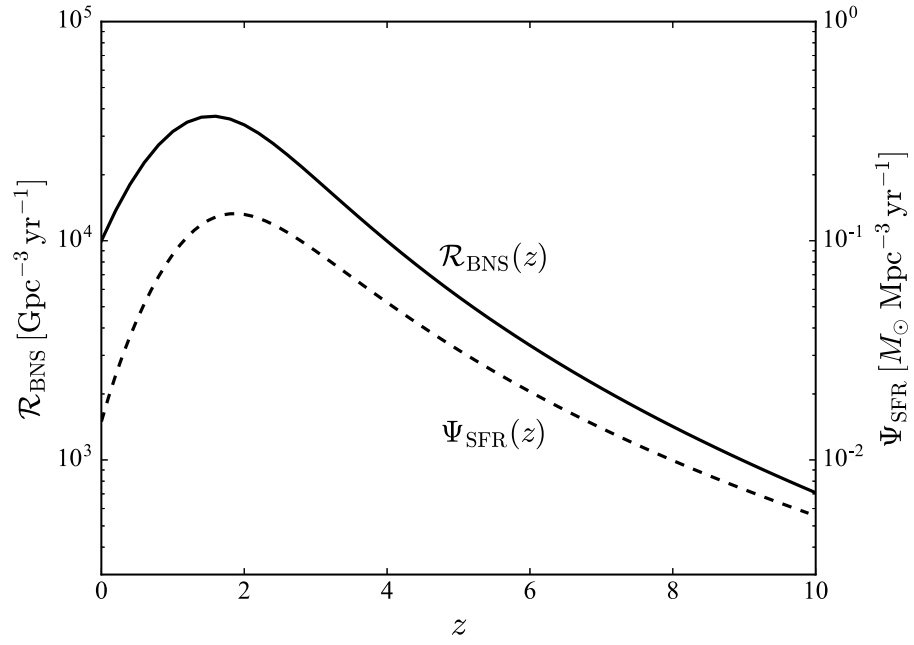
Figure 2.4: Cosmic star formation rate Ψ_{SFR} (dashed line, right-hand-side ordinate) and cosmic BNS merger rate $\mathcal{R}_{\mathrm{BNS}}$ (solid line, left-hand-side ordinate) per unit comoving volume in our model are shown as a function of redshift z.
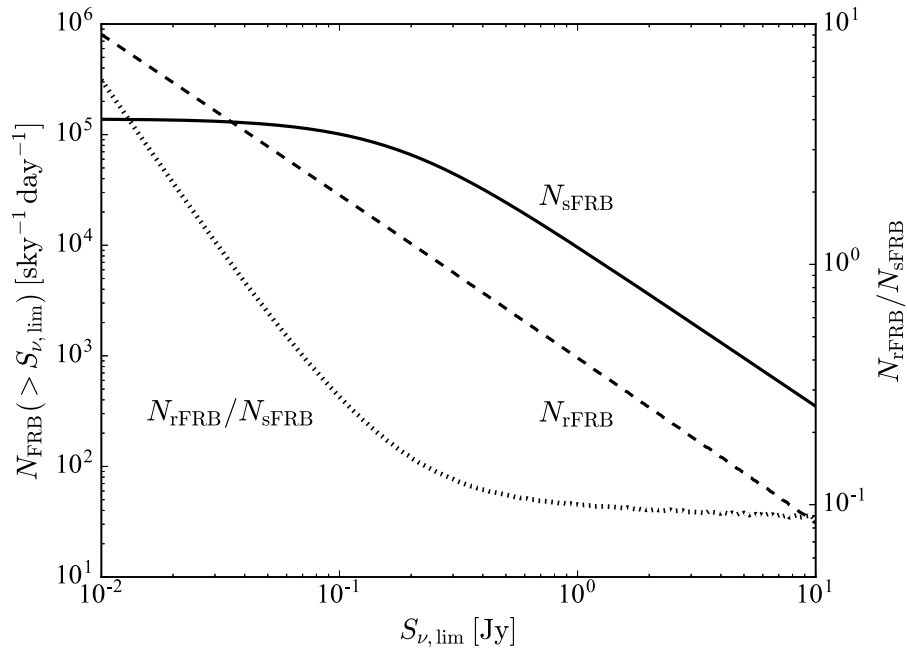
Figure 2.5: Occurrence rate of FRBs that are brighter than a search flux sensitivity limit, for non-repeating (single) FRBs (N_{sFRB}) and repeating FRBs (N_{rFRB}). The repeating FRB rate is normalized as 10% of non-repeating FRBs at $S_{\nu,\mathrm{lim}} = 1$ Jy (i.e., $f_r N_r = 400$). The ratio $N_{\mathrm{rFRB}}/N_{\mathrm{sFRB}}$ is also plotted (see ordinate on the right handed side).

Chapter 3

Galactic Halo Contribution to the Dispersion Measure of FRBs

The work presented in this chapter appeared in: *Yamasaki, S., & Totani, T. The Galactic Halo Contribution to the Dispersion Measure of Extragalactic Fast Radio Bursts. ApJ, 888, 105.*

3.1 Introduction

As introduced in Section 1.2.6, FRBs opened up an entirely new way to probe the diffuse hot gas halo in and outside the Galaxy. This thus motivates theoretical investigations of the extended hot gas halo distribution inside galaxies with FRBs in mind. Historically, the distribution of hot gas ($kT \sim 0.3$ keV) in the MW halo has been studied based on analytic gas density profile or numerical simulations, with observational constraints from oxygen absorption lines in UV or X-ray bands, emission measure (EM) of diffuse X-ray emission, and DM toward the Large Magellanic Cloud (LMC; Maller & Bullock 2004; Sommer-Larsen 2006; Yao et al. 2009; Fang et al. 2013; Nuza et al. 2014; Dolag et al. 2015; Tepper-García et al. 2015; Roca-Fàbrega et al. 2016; Faerman et al. 2017; Fielding et al. 2017; Li & Bregman 2017; Nakashima et al. 2018; Shull & Danforth 2018; Prochaska & Zheng 2019). The DM value estimated by these modelings is $\mathrm{DM_{halo}} \sim 30$–$80 \, \mathrm{pc \, cm^{-3}}$. Most of these studies considered a spherically symmetric halo, but recent X-ray observations of diffuse halo gas revealed a significant directional dependence of the EM, which motivated several studies to introduce a disk-like halo gas distribution (Yao et al. 2009; Fang et al. 2013; Li & Bregman 2017; Nakashima et al. 2018). It should be noted that this hot disk-like

halo component is completely different in physical properties (such as temperature and geometrical shape) from the so-called "warm thick disk", which is included in the warm ISM models and generally constrained by Galactic pulsar DM measurements (see Section 3.5.1).

However, such a disk-like model results in a scale radius of less than 10 kpc and the associated gas mass much smaller than that of total halo gas expected from the total dark matter mass of the MW halo and the cosmic ratio of baryons to dark matter. This indicates that we need to incorporate two components for a realistic model of MW halo gas distribution: a spherical component extending up to the virial radius ($\sim$200 kpc) and a more compact disk-like component responsible for the diffuse X-ray emission[1]. Both components may have significant contribution to the DM, and the purpose of this work is to construct such a two-component, direction-dependent model of the MW halo gas distribution and DM.

This chapter is organized as follows. In Section 3.2, we describe the framework of our model for spatial distribution of the hot gas halo. The modeled EM and DM are compared with observational constraints in Section 3.3. We then provide a fitting formula of the halo DM as a function of the Galactic coordinate for a convenient use in FRB observations in Section 3.4, and discussion on our newly proposed model is given in Section 3.5, followed by conclusions in Section 3.6. The adopted cosmological parameters for a flat universe are $H_0 = 67.8 \, \mathrm{km \, s^{-1} \, Mpc^{-1}}$, $\Omega_m = 0.308$, $\Omega_\Lambda = 0.692$ and $\Omega_b = 0.0483$ (Planck Collaboration et al. 2016). Our choice of the Galactocentric distance of the Sun is $D_\odot = 8.5$ kpc (Kerr & Lynden-Bell 1986). When calculating the number density of gas particles, we take a mean molecular mass per electron, $\mu_e \equiv \rho/(m_p n_e) = 1.18$ (ρ, m_p and n_e are gas mass density, the proton mass and electron number density, respectively), a mean particle mass $\mu \equiv \rho/(m_p n) = 0.62$ (n denotes the number density of all particles, including baryonic particles and free electrons, that contribute to the gas pressure), and a number density ratio of hydrogen to electron $\chi_H = 0.82$ (independent of gas metallicity, see Appendix B). These were calculated assuming fully ionized hydrogen and helium with a helium mass abundance of 30%.

---

[1]Fang et al. (2013) explored the Galactic gas distribution by combining warm thick disk and hot spherical halo, which is in contrast to our idea of combining two hot gas halo components.

3.2   A Model for the Hot Gas Halo

Hot gas existing in the MW halo can be probed by EM (EM $\equiv \int n_e n_{\rm H} ds$) of diffuse X-ray emission, where $n_{\rm H}$ is the hydrogen number density and s is a coordinate along the line of sight (e.g., Snowden et al. 1997; McCammon et al. 2002; Yao & Wang 2007; Yao et al. 2009; Gupta et al. 2012; Yoshino et al. 2009; Hagihara et al. 2010; Henley & Shelton 2013; Nakashima et al. 2018). Most recently, Nakashima et al. (2018) (hereafter N18) have estimated EM to 107 sightlines by the *Suzaku* X-ray observations at $75° < l < 285°$ and $|b| > 15°$. They found that the observed EM distribution over the entire sky cannot be described by a spherically symmetric electron density distribution, but can be reproduced by a disk-like distribution

$$n_e^{\rm disk}(R, z) = n_0^{\rm disk} \exp\left[-\left(\frac{R}{R_0} + \frac{|z|}{z_0}\right)\right], \qquad (3.1)$$

where R and z are the cylindrical coordinates, and $n_0^{\rm disk} = 3.8^{+2.2}_{-1.2} \times 10^{-3} (Z_{\rm halo}/Z_\odot)^{-1}$ cm^{-3} ($Z_{\rm halo}$ denotes the halo hot gas metallicity), $R_0 = 7.0^{+2.1}_{-1.7}$ kpc, and $z_0 = 2.7^{+0.8}_{-0.7}$ kpc. The metallicity dependence appears because X-ray emissivity is dominated by oxygen ions.

However, the total mass of this disk-like component is only $\sim 2 \times 10^8 (Z_{\rm halo}/Z_\odot)^{-1} M_\odot$, which is much smaller than the total halo gas mass expected by the MW dark halo mass and the cosmic mass ratio of dark to baryonic matter (e.g., Yao & Wang 2007; Fang et al. 2013; Miller & Bregman 2015; Li & Bregman 2017). Although such a more massive, more spherical, and more extended (up to the virial radius) halo may not significantly contribute to the observed EM of diffuse X-ray emission, it should exist theoretically (e.g., Spitzer 1956; Cen & Ostriker 1999) and it is also supported by observations of absorption lines (e.g., Nicastro et al. 2002; Tumlinson et al. 2011). Therefore in this work we perform a new fit to the observed EM of N18 with the two components of the compact disk-like halo and the extended spherical halo.

For the spherical component, we therefore introduce a theoretical density profile that is modeled as the isothermal gas in hydrostatic equilibrium with a Galactic dark matter halo. In our model, MW's dark matter halo has a virial mass of $M_{\rm vir} = 10^{12}\, M_\odot$ and a virial radius of $r_{\rm vir} = 260$ kpc according to the model by Klypin et al. (2002). We assume that the dark matter distribution follows the Navarro–Frenk–White (NFW) profile gravitational potential Φ with a concentration of $c_{\rm vir} \equiv r_{\rm vir}/r_s = 12$ with r_s being an NFW scale radius (Navarro et al. 1997; Bullock et al. 2001). The gravitational potential of the Galactic stellar disk is neglected since it has little effect on the resulting density profile. Assuming the ideal gas with a constant temperature $T_{\rm halo}$, gas pressure is given by $P/\rho = kT_{\rm halo}/(\mu m_p)$ and hydrostatic equilibrium (HE)

$\nabla P = -\rho \nabla \Phi$ reduces to

$$n_e^{\text{sphe}}(r) = n_0^{\text{sphe}} \exp\left\{ -\Upsilon \left[1 - \frac{\ln\left(1 + r/r_s\right)}{r/r_s} \right] \right\}, \tag{3.2}$$

where $\Upsilon = 4\pi G r_s^2 \rho_s \mu m_p / (kT_{\text{halo}})$ is a dimensionless constant with $\rho_s = \rho(r_s)$ being the NFW scale density. We assume the same temperature for the disk-like and spherical components as $kT_{\text{halo}} = 0.3$ keV based on the X-ray observation (N18). The central electron density n_0^{sphe} is determined so that the enclosed gas mass of the spherical component within r_{vir} is equal to the Galactic baryon mass M_b:

$$\int_0^{r_{\text{vir}}} 4\pi r^2 \mu_e m_p \, n_e^{\text{sphe}}(r) \, dr = M_b. \tag{3.3}$$

We choose the fiducial total baryon mass to be $M_b = 1.2 \times 10^{11} \, M_\odot$, assuming the baryon fraction M_b/M_{vir} of the MW is $\sim 75\%$ of the cosmic mean $\Omega_b/\Omega_m \sim 0.16$, which is the same value as adopted by Prochaska & Zheng (2019). These figures are roughly consistent with an estimate that $\sim 26\%$ of galactic baryons reside in the stars and ISM (Fukugita et al. 1998), if the remaining $\sim 74\%$ of baryons are in the galactic halo. Combining the above assumptions, we obtain $\Upsilon = 2.6$ and $n_0^{\text{sphe}} = 3.7 \times 10^{-4}$ cm^{-3} as fiducial values for our model.

3.3 Observational Constraints

Here we construct our nonspherical hot gas halo models by fitting to the observed X-ray EM. Then we present our model in comparison with existing theoretical models, and examine its consistency with DM of LMC pulsars and absorption line observations.

3.3.1 Fit to X-Ray EM

Observations of the diffuse X-ray EM have benefits of a large number of sightlines. To construct a direction-dependent model of the MW halo DM, we utilize the measurements of halo gas EM, $\text{EM}_{\text{N18},\odot}$, which are presented as EM_{halo} in Table 1 of N18. The $\text{EM}_{\text{N18},\odot}$ for each siteline was determined, along with gas temperature and [O/Fe], by spectral fittings. The medians of temperature and [O/Fe] over all sitelines are 0.26 keV and 0.25, respectively (N18). The metallicity of the halo gas is not well constrained by the X-ray data, and it was fixed to the solar abundance. However, X-ray emissions are dominated by continuum recombination emission from oxygen
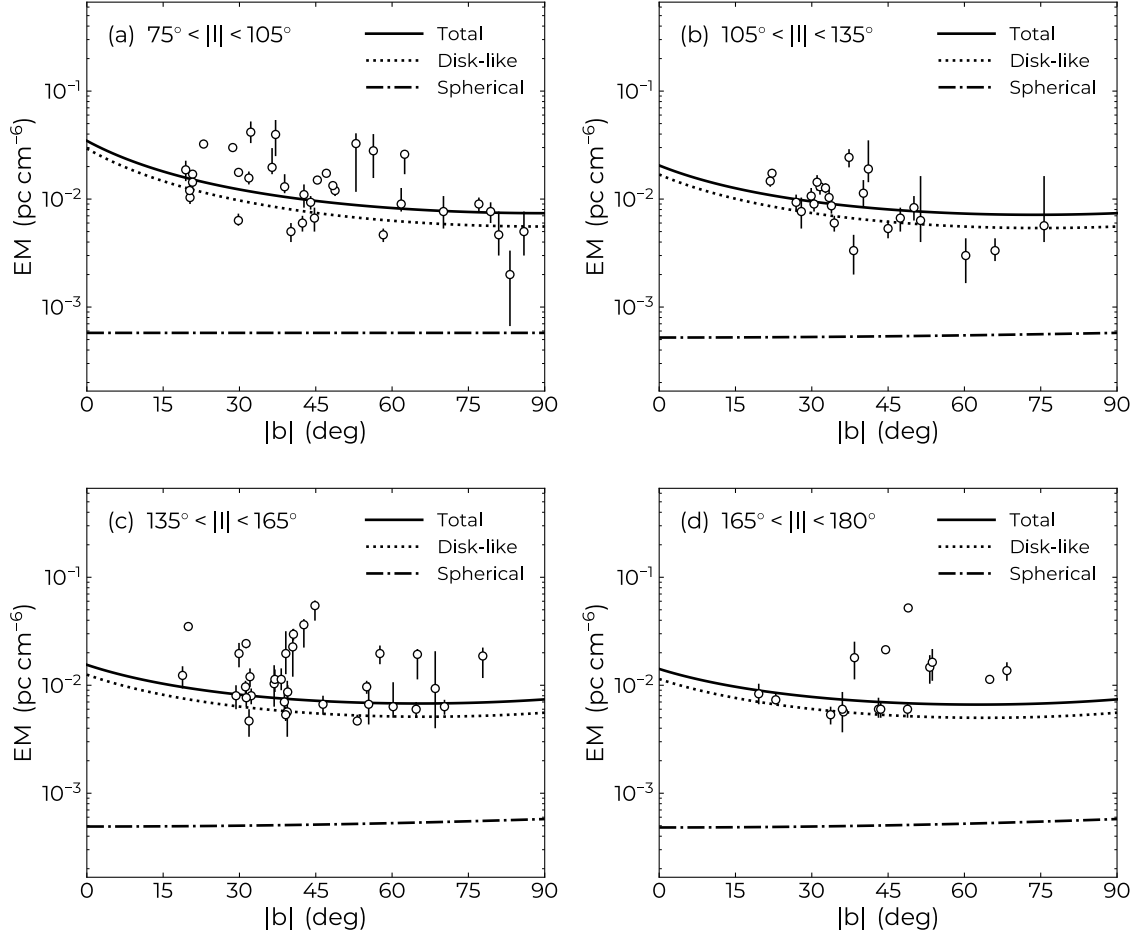
Figure 3.1: Emission measures of the hot halo gas as a function of Galactic latitude. Each panel corresponds to four different regions in Galactic longitude. The halo gas metallicity is assumed to be $Z_{\mathrm{halo}} = 0.3 Z_\odot$ for the observed EM data points. Two data points in 107 sightlines in Table 1 of Nakashima et al. (2018) with an upper limit are removed in this figure and model fitting. Model predictions are plotted for (a) $|l| = 90°$; (b) $|l| = 120°$; (c) $|l| = 150°$; (d) $|l| = 180°$. Here $|l|$ is defined such that $|l| = l$ ($0° \leq l \leq 180°$) and $|l| = 360° - l$ (otherwise).
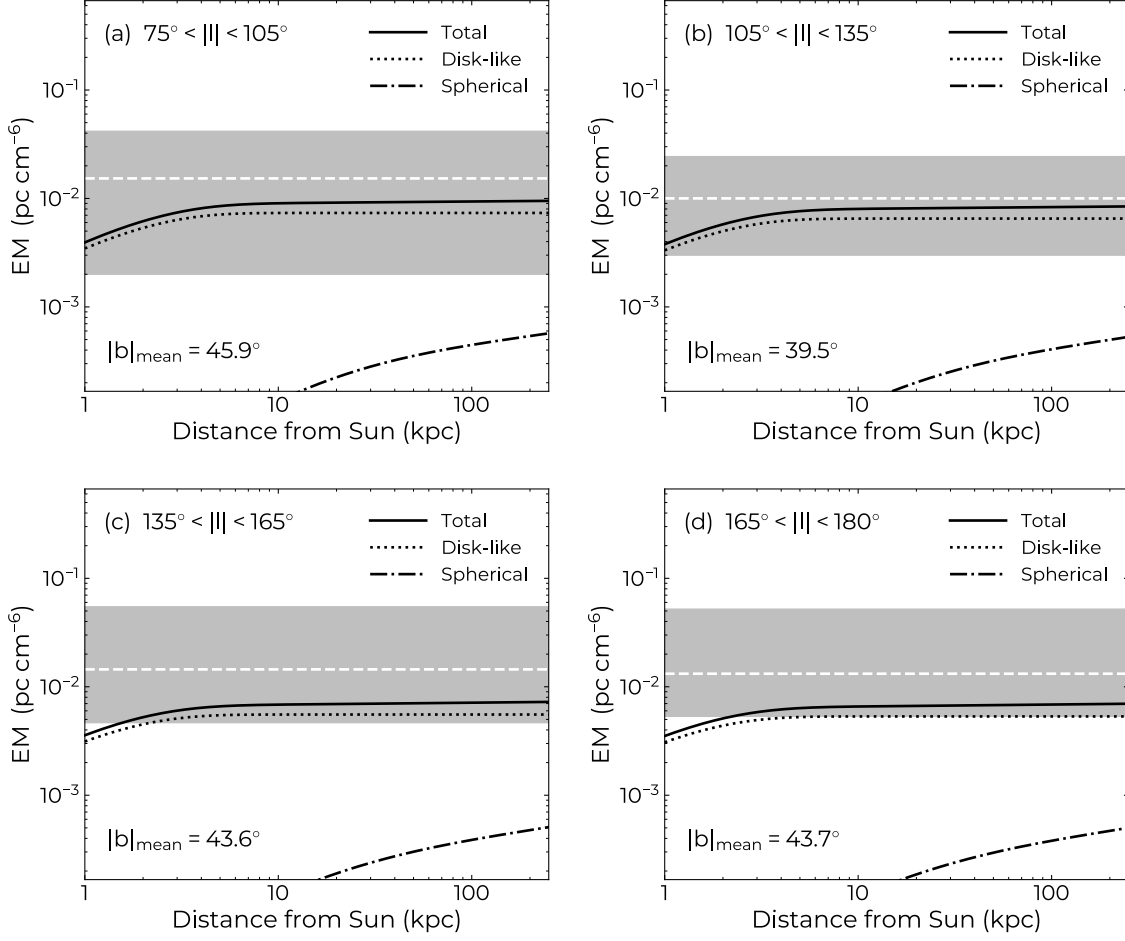
Figure 3.2: Emission measures of the hot gas halo as a function of radius. The grey shaded region denotes the full range of variation in data, and the horizontal dashed line is the mean. Model predictions are plotted for the same Galactic longitude as Figure 3.1 with Galactic latitude chosen to the mean of data $|b|_{\mathrm{mean}}$ as shown in each panel.

ions. Therefore the true EM should scale with the halo gas metallicity as:

$$\text{EM}_{\text{N18}} = \left(\frac{Z_{\text{halo}}}{Z_\odot} \right)^{-1} \text{EM}_{\text{N18},\odot} . \tag{3.4}$$

Throughout this work, we adopt $Z_{\text{halo}} = 0.3 \, Z_\odot$ as suggested by cosmological simulations (Cen & Ostriker 2006) and observations of high velocity clouds (e.g., Gibson et al. 2000; Fox et al. 2005). Distribution of EM_{N18} is shown in four panels of Figure 3.1 as a function of Galactic latitude. Despite the large scatter seen in the data, N18 statistically confirm the trend of decreasing EMs as Galactic latitudes increase.

We construct an empirical model for the entire electron density distribution of the hot gas by combining Equations (3.1) and (3.2): $n_e = n_e^{\text{disk}} + n_e^{\text{sphe}}$. Since the mass ratio between the disk-like and spherical halo components within r_{vir} is expected to be small, a naive summation of these barely affects the HE assumption. The modeled EM of the halo gas toward a given Galactic coordinate (l, b) is computed by

$$\text{EM}_{\text{model}}(l, b) \equiv \int_0^{s_{\text{max}}} n_e(s) \, n_{\text{H}}(s) \, ds, \tag{3.5}$$

where $n_{\text{H}} = \chi_{\text{H}} \, n_e$ is the hydrogen number density, and we integrate the hot gas halo density profile along the line of sight from the solar system out to the maximum distance $s_{\text{max}}(l, b)$ corresponding to the virial radius of the MW halo.

Since the spherical component is already fixed by Equation (3.3), the remaining parameters to be determined are n_0^{disk}, R_0 and z_0 that characterize the disk-halo component. These are determined by fitting EM_{model} to EM_{N18} using Markov Chain Monte Carlo (MCMC) sampling with emcee, a Python based affine invariant sampler (Foreman-Mackey et al. 2013). The likelihood function is $\ln(\mathcal{L}) = -\chi^2/2$, where the standard deviation associated with each data is defined by the geometric mean of the asymmetric errors. We adopt a flat prior distribution for all of our parameters in the $n_0^{\text{disk}}/(10^{-3} \text{ cm}^{-3}) \in [0.1, 100]$, $R_0/(\text{kpc}) \in [0.1, 100]$, and $z_0/(\text{kpc}) \in [0.1, 100]$. We generate 10^5 samples and obtain the best set of parameters with $n_0^{\text{disk}} = 7.4^{+2.2}_{-1.6} \times 10^{-3}(Z_{\text{halo}}/Z_\odot)^{-1} \text{ cm}^{-3}$, $R_0 = 4.9^{+0.6}_{-0.5}$ kpc, and $z_0 = 2.4^{+0.4}_{-0.4}$ kpc, where errors are estimated by the 16th and 84th percentile of the MCMC realizations.

The EMs predicted with best-fit parameters as a function of Galactic latitude and distance are presented in Figure 3.1 and Figure 3.2, respectively. In Figure 3.1 we see that the modeled EM is dominated by the disk-like component, and our model matches the trend of EM against spatial directions. Figure 3.2 indicates that the total EM reaches the observed EM at $\lesssim 5$ kpc from the Sun, reflecting the dominance of the disk-like halo. The large scatter of the data from the mean might be due to a

density fluctuation in the disk-like halo.

3.3.2 Comparison with Previous Studies

Here we compare our model with three models of previous studies in the literature: (1) an isothermal model with multiple gas phases (the fiducial model with $Z_{\mathrm{halo}} = 0.5\,Z_\odot$ of Faerman et al. 2017; hereafter F17), (2) an adiabatic gas model with polytropic index 5/3 (Fang et al. 2013, hereafter F13, see also Maller & Bullock 2004) and (3) a modified NFW profile with $\alpha = y_0 = 2$ of Mathews & Prochaska (2017) and Prochaska & Zheng (2019) (hereafter PZ19). Figure 3.3 shows density (left panel) and mass (right panel) profile of the hot gas for different models. Since the disk-like component in our model has directional dependence, profiles to two directions (along R- and z-axis) are shown. The spherical component of our model is quantitatively similar to the F13 model.

3.3.3 LMC Pulsar Dispersion Measure

The dispersion measurements of pulsars outside the Galactic disk provide us the most direct tool to reveal the gas distribution in the MW. While most Galactic pulsars lie in the Galactic disk, some of them have been found in the LMC at a distance of 49.97 ± 1.3 kpc (Pietrzyński et al. 2013) from the Sun. Because of the large offsets from the Galactic disk, LMC pulsars have been used to probe the hot halo gas distribution in the literature (e.g., Anderson & Bregman 2010; F13). Here we focus on three LMC pulsars with the lowest DMs of 65, 68, 69 pc cm^{-3} (McConnell et al. 1991; Manchester et al. 2006). To estimate the hot gas halo contribution to LMC pulsar DMs, we need to subtract the contribution from the ISM in the MW disk and spiral arms. We find $\mathrm{DM_{ISM}} = 53$ pc cm^{-3} for NE2001 model (48 pc cm^{-3} for YMW16 model), thereby obtaining upper limits on the hot gas halo DM at the LMC location as $\mathrm{DM_{halo}} = \mathrm{DM_{PSR}} - \mathrm{DM_{ISM}} = 12\text{–}16$ pc cm^{-3} for NE2001 (17–21 pc cm^{-3} for YMW16). Here we assume that the measurement uncertainty and the DM contribution from local gas within the LMC are both negligible. The uncertainty arising from $\mathrm{DM_{ISM}}$ models is conservatively taken to be 20% (Cordes & Lazio 2002).

Figure 3.4 shows the hot gas halo DM profiles along the LMC sightline ($l = 280°$, $b = -32.9°$) for different halo gas models. Given the large uncertainty of warm ISM models, most of the models are marginally consistent with the upper-limits established by the LMC pulsar DM. It should be noted that the DM predicted by our model is dominated by the disk-like component, which is not taken into account
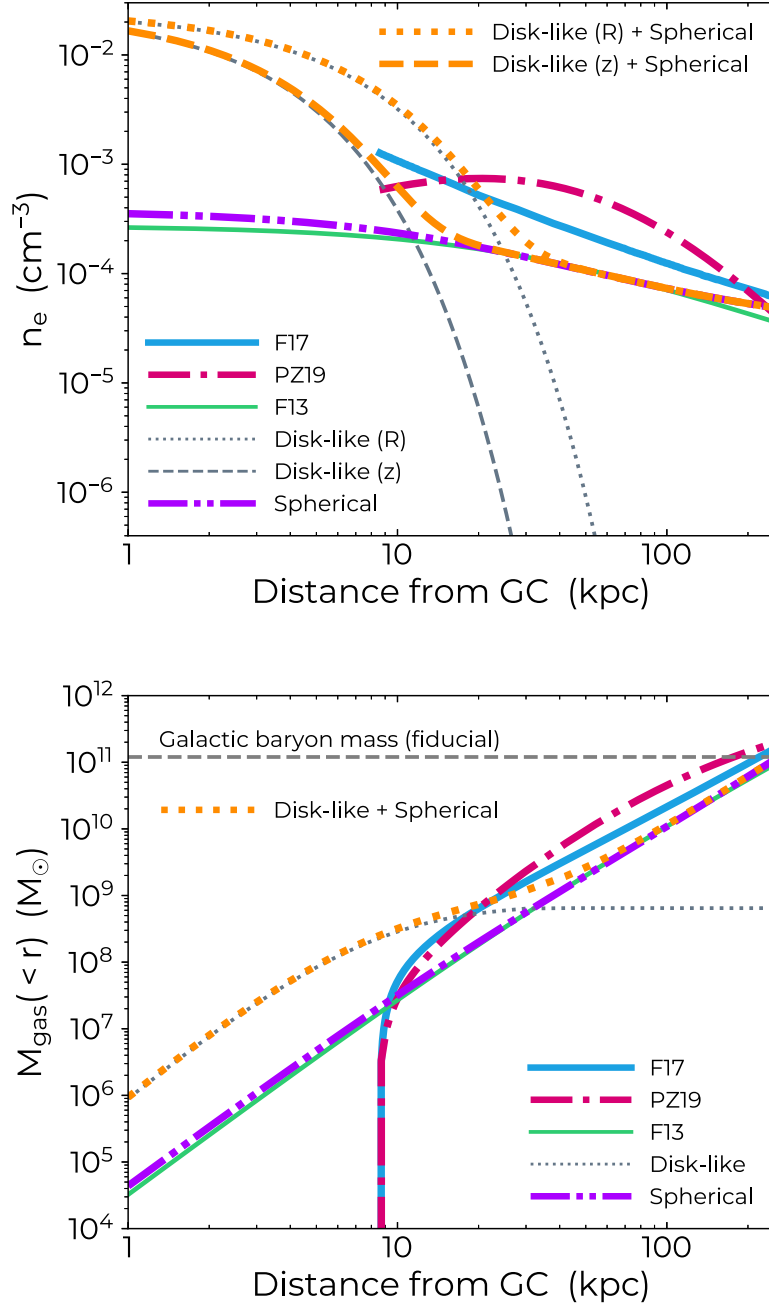
Figure 3.3: Hot gas profile as a function of Galactocentric radius. *Upper panel*: electron density; *lower panel*: enclosed hot gas mass within Galactocentric radius $< r$. For density profiles of the disk-like halo component of our model, two profiles into vertical (z-axis) and in-plane (R-axis) directions are shown. The density profiles of F17 and PZ19 are shown only at $r > D_\odot$, according to their definitions. The horizontal gray dashed line shown in the lower panel indicates the fiducial baryon mass of the MW.
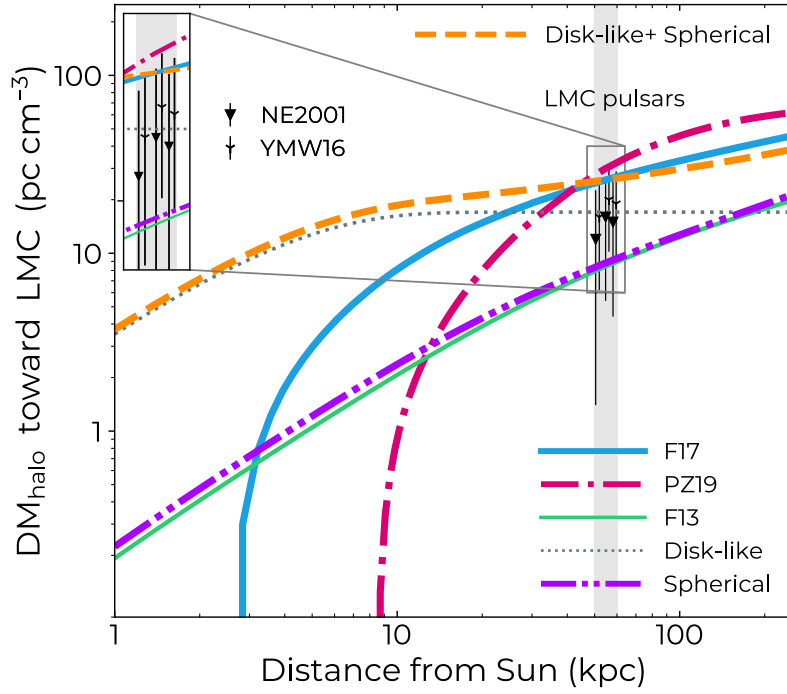
Figure 3.4: Hot gas halo dispersion measure as a function of distance in the LMC direction. LMC pulsar data are randomly distributed at $s \in [50, 60]$ kpc (denoted by the gray shaded region) for display purposes. The two data points for the same pulsar but assuming the two different DM models of the Galactic disk are placed next to each other. The region around the data points is also shown as inset zoom-in.

in previous models. This implies that gas density of the previous models by F17 and PZ19 is too high compared to that of the spherical component of our model.

3.3.4   Absorption Line Measurements

Another observational constraint comes from the X-ray absorption lines of highly ionized oxygen (O VII and O VIII) and a UV absorption line (O VI) by MW halo gas seen in distant active galactic nuclei (AGN) or blazar spectra (e.g., Nicastro et al. 2002; Fang et al. 2002, 2003; Rasmussen et al. 2003; Sembach et al. 2003; Collins et al. 2004; McKernan et al. 2004; Wang et al. 2005; Bregman 2007; Bregman & Lloyd-Davies 2007; Hagihara et al. 2010; Gupta et al. 2012; Miller & Bregman 2013, 2015; Fang et al. 2015). These observations have been used to constrain the MW halo gas models (e.g., F17 and PZ19).

However, we only utilize data of the diffuse X-ray EM in this study for the following reasons. First, since the absorption lines are not fully resolved with grating spectrometers, the same line velocity width often needs to be assumed for different sitelines, and thus the inferred ionic column density (i.e., DM) strongly depends on the assumed gas kinematics. The other reason is that absorption line measurements tend to be limited to the direction of bright AGNs or blazars, which would lead to a smaller size of sample per each measurement ($N \lesssim 30$, Gupta et al. 2012; Miller & Bregman 2013, 2015; Fang et al. 2015) compared to diffuse X-ray observations ($N \gtrsim 100$, Henley & Shelton 2013; N18). Therefore we chose to fix the spherical component of our model by the total gas mass theoretically expected from the MW dark mass.

One of the most recent study of OVII absorptions toward nearby AGNs at high Galactic latitudes $|b| \gtrsim 30°$ (Fang et al. 2015) suggests that typical column densities through the Galactic halo are $N_{\mathrm{OVII}} = 10^{15.5}$–$10^{17}\,\mathrm{cm}^{-2}$ with large scatters likely due to the measurement uncertainties. Assuming that O VII is the dominant state among ionized oxygens with the hot gas metallicity of $Z_{\mathrm{halo}} = 0.3 Z_\odot$, this translates into a dispersion measure of

$$\mathrm{DM_{OVII}} = 82\,\mathrm{pc\,cm^{-3}} \left(\frac{N_{\mathrm{OVII}}}{10^{16.5}\,\mathrm{cm^{-2}}} \right) \left(\frac{Z_{\mathrm{halo}}}{0.3 Z_\odot} \right)^{-1}, \qquad (3.6)$$

where we adopt a rough median value for N_{OVII} (see also Shull & Danforth 2018 and PZ19 for similar estimates). Meanwhile, our model predicts $\mathrm{DM_{halo}} = 30$–$70\,\mathrm{pc\,cm^{-3}}$ over the same region of the sky. Therefore, the difference between F17, PZ19, and the spherical component of our model is within the uncertainty in using absorption

lines, and hence our model is fully consistent with the absorption line observations.

3.4 Analytic Formula for MW Halo DM

Based on our new hot gas halo model, here we aim to provide a convenient analytic formula of the hot gas halo DM to any given direction to an extragalactic object. We calculated a full-sky map for $\mathrm{DM_{halo}}$ by integrating n_e until the sightline intersects the sphere of the virial radius $r = r_{\mathrm{vir}}$. Figure 3.5 describes the derived DM profile for selected Galactic latitudes. The halo DM of our model spans the range $\mathrm{DM_{halo}} = 30$–245 pc cm^{-3} over the whole sky, with a mean of 43 pc cm^{-3}. A choice of larger integration limits corresponding to $r = 1.5\,r_{\mathrm{vir}}$–$2.0\,r_{\mathrm{vir}}$ increases the mean $\mathrm{DM_{halo}}$ value only by 14%–26%. If we attribute the scatter seen in the X-ray EM data (0.4 dex) to the fluctuation of the hot gas density, DM should have a scatter of 0.2 dex as $\mathrm{DM} \propto n_e$ and $\mathrm{EM} \propto n_e^2$. Figure 3.6 shows the ratio of the two components of the halo DM, disk-like to spherical, and it ranges in 0.4–9 over the full-sky region, which demonstrates the highly nonspherical nature of our model.
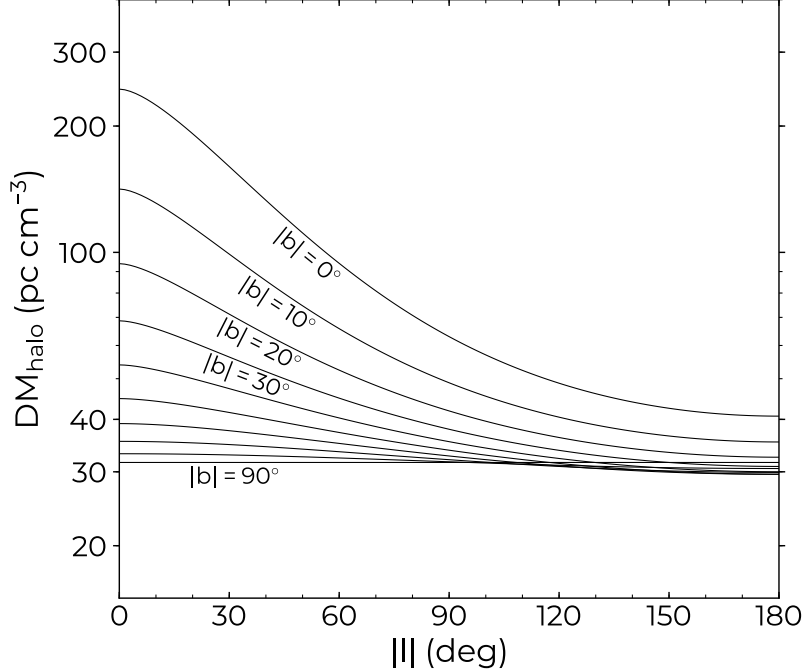
Figure 3.5: Hot gas halo DM (disk-like halo plus spherical) as a function of the Galactic longitude. Ten curves are shown corresponding to the Galactic latitude of $|b| = 0°$ to 90° with a step of 10°.
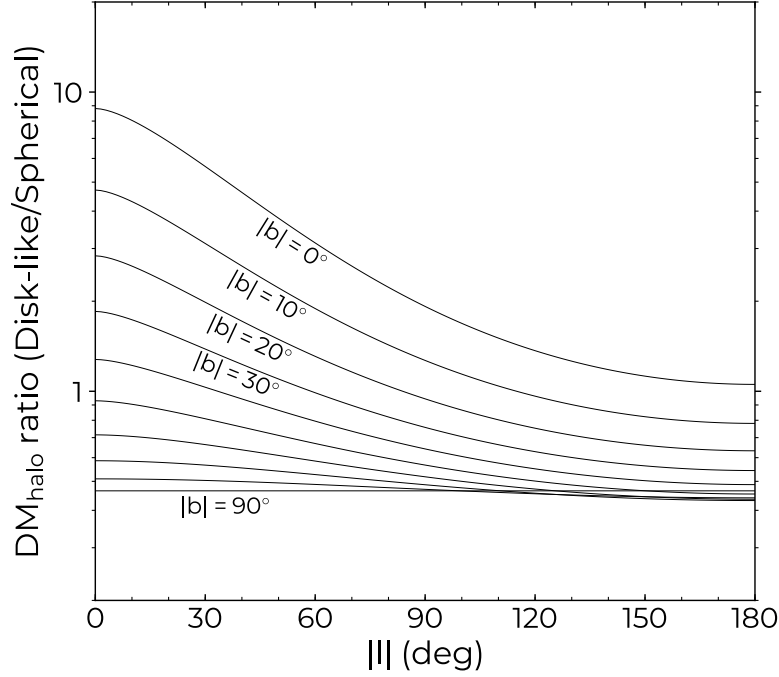
Figure 3.6: Same as Figure 3.5, but the DM ratio of the disk-like halo to the spherical component is shown.

The fitting formula of the halo DM as a function of the Galactic coordinate is obtained with the 7th-order polynomial as

$$\mathrm{DM}_{\mathrm{halo}} = \sum_{i,\,j=0}^{n} c_{ij}\, |l|^{i}\, |b|^{j} \; , \tag{3.7}$$

where c_{ij} is the fitting coefficient in units of pc cm^{-3}, l and b are Galactic coordinates measured in radians, and $n = 7$. The fitting result is summarized in Table 3.1. We confirm that this formula reproduces the theoretical prediction within 4% accuracy, and the regions of an accuracy better than 1% amount to 98% of the entire sky. This formula for $\mathrm{DM}_{\mathrm{halo}}$ can be used in combination with existing $\mathrm{DM}_{\mathrm{ISM}}$ models (NE2001 and YMW16) to estimate the total DM by electrons in the MW. In order to separate the $\mathrm{DM}_{\mathrm{halo}}$ contributions by disk-like and spherical component, we also show a fitting result only for the spherical halo component with $n = 3$ in Table 3.1, which achieves a higher model accuracy (within 2%) due to a smaller directional dependence of the spherical halo.

3.5   Discussion

3.5.1   Relation to the Warm Electron Models

The spatial distributions of WIM in the Galactic ISM have been modeled by the observed DMs toward Galactic radio pulsars (Taylor & Cordes 1993; Cordes & Lazio 2002, 2003; Yao et al. 2017), and the diffuse component of WIM is known to distribute in the so-called "warm thick disk" with a vertical scale height of $\lesssim 2$ kpc and a mid-plane electron number density of $\sim 0.01\,\mathrm{cm}^{-3}$ (see, e.g., Readhead & Duffett-Smith 1975; Reynolds 1989; Gaensler et al. 2008; Savage & Wakker 2009). Figure 3.7 illustrates the density profile of warm thick disks (NE2001 and YMW16) in comparison with our hot disk-like halo. Since the gas distribution of the hot disk-like halo component evidently overlaps with those of thick disk models, there is a possibility that the hot disk-like halo has already been taken into account partly in the modeling of the thick disk by NE2001 and YMW16.

In Figure 3.8 we show the spatial distribution of 189 Galactic pulsars having independent distance constraints (mostly by parallax measurements) that have been used to model the warm thick disks (YMW16, see also the ATNF Pulsar Catalogue documented in Manchester et al. 2005). The average distance from the Sun to those pulsars is 3.4 kpc, and most of them lie in the vicinity of the Galactic plane ($|z| \lesssim 2$ kpc and 5 kpc $\lesssim R \lesssim 15$ kpc). Figure 3.9 compares the predicted DM for these pulsars by the warm thick disks and the hot disk-like halo. It clearly indicates that for the majority of these pulsars, DM contribution from warm thick disks is at least a few times larger than that from the hot disk-like halo. The geometrical shapes of the thick disks and our disk-like halo are significantly different, and it is unlikely that the disk-like halo is properly taken into account in the warm disk models. Therefore, we recommend to simply add $\mathrm{DM_{halo}}$ of our model (presented in Chapter 3.4) to $\mathrm{DM_{ISM}}$ of NE2001 or YMW16 to estimate the total DM of the MW.

3.5.2   Model Uncertainties

Based on our fiducial hot gas halo model, we estimate the mean halo DM of $\mathrm{DM_{halo}} = 43$ pc cm^{-3}. We note that this number should only be considered as a benchmark due to the following systematic uncertainties. First, since the observed EMs can be almost fitted with the disk-like halo component alone, the major source of uncertainty originates from the modelling of spherical halo component (i.e., the total gas mass of the spherical halo within the virial radius M_b). We find that the fraction of the cosmic baryons in the Galactic halo f_b, defined as $M_b/M_{\mathrm{vir}} = f_b(\Omega_b/\Omega_m)$, needs to be

less than unity (a fiducial value of $f_b = 0.75$) to be consistent with the DM toward the LMC with the best-fit disk-like halo component being unchanged. If we consider the possible range of $f_b \in [0, 1]$ (although $f_b = 0$ is a rather extreme limit), the mean halo DM over the whole sky ranges $\mathrm{DM_{halo}} = 21$–50 pc cm^{-3}. This means that a choice of different f_b (or M_b) change the estimate of $|\mathrm{DM_{halo}}|$ by at most $\lesssim 20$ pc cm^{-3}. By contrast, statistical uncertainties in the best-fit parameters of the disk-like halo component is negligible. Secondly, it is found that a choice of larger integration limits corresponding to $r = 1.5\,r_{\mathrm{vir}}$–$2.0\,r_{\mathrm{vir}}$ increases the mean $\mathrm{DM_{halo}}$ value only by 14%–26%. Lastly, if we attribute the scatter seen in the X-ray EM data (0.4 dex) to the fluctuation of the hot gas density, $\mathrm{DM_{halo}}$ should have a scatter of 0.2 dex over the whole sky, as $\mathrm{DM} \propto n_e$ and $\mathrm{EM} \propto n_e^2$.

3.5.3 Application to Host-identified FRBs

Here we focus on two non-repeating sources FRB 180924 (Bannister et al. 2019) and FRB 190523 (Ravi et al. 2019) for which the redshifts are known. In order to discuss the DM budget for these sources, we utilize the $\mathrm{DM_{IGM}}$-z relation (Ioka 2003; Inoue 2004; Deng & Zhang 2014):

$$\mathrm{DM_{IGM}}(z) = \Xi_{\mathrm{IGM}} \int_0^z \frac{f_e(z')(1+z')dz'}{\sqrt{\Omega_m(1+z')^3 + \Omega_\Lambda}},$$

$$\Xi_{\mathrm{IGM}} \equiv \frac{3cH_0\Omega_b f_{\mathrm{IGM}}}{8\pi G m_p} \approx 1100\,f_{\mathrm{IGM}} \text{ pc cm}^{-3}. \tag{3.8}$$

Here $f_e = 1/\mu_e$ is the ionization factor, and we neglect the redshift dependence, and f_{IGM} denotes the fraction of baryons that reside in the ionized IGM, which has yet to be constrained well. The current cosmic baryon census suggests that $f_{\mathrm{IGM}} \gtrsim 0.6$ (Shull et al. 2012) and f_{IGM} could be as high as ~ 0.9 (e.g., Fukugita & Peebles 2004) provided that all the missing baryons ($\sim 30\%$) exist as a form of diffuse IGM. Here we set $f_{\mathrm{IGM}} \in [0.6, 0.9]$ as a plausible range. The systematic errors in our halo model is conservatively taken to be ± 20 pc cm^{-3} (see Section 3.5.2).

FRB 180924.—The host is an massive galaxy with stellar mass of $M_* \sim 2.2 \times 10^{10}\,M_\odot$ at $z \sim 0.32$ (Bannister et al. 2019). The total DM is reported to be $\mathrm{DM_{obs}} = 361$ pc cm^{-3} (Bannister et al. 2019), and an upper limit on $\mathrm{DM_{IGM}}$ is obtained by $\mathrm{DM_{IGM}} \leq \mathrm{DM_{obs}} - \mathrm{DM_{ISM}} - \mathrm{DM_{halo}}$, where the equality holds when $\mathrm{DM_{host}} = 0$. The ISM contribution to this direction $[(l, b) = (0.74°, -49°)]$ is estimated as $\mathrm{DM_{ISM}} = 41$ (NE2001) or 28 pc cm^{-3} (YMW16) by the two different models. The MW halo contribution to this direction by our model is $\mathrm{DM_{halo}} = 46^{+20}_{-20}$ pc cm^{-3}, compared to 50–80 pc cm^{-3} estimated by PZ19. Compared with the theoretical value of $\mathrm{DM_{IGM}} =$

$320\,f_{\mathrm{IGM}}\,\mathrm{pc\,cm^{-3}}$ from Equation (3.8), the observation gives a constraint on f_{IGM}. Our $\mathrm{DM_{halo}}$ model predicts a lower value than PZ19, and hence a weaker constraint of $f_{\mathrm{IGM}} < 0.79$–0.96 depending on the $\mathrm{DM_{ISM}}$ models, which should be compared with $f_{\mathrm{IGM}} < 0.75$–0.79 when the high end value of PZ19 is adopted.

FRB 190523.—The host is a massive ($M_* \sim 5.0 \times 10^{11}\,M_\odot$) galaxy at $z \sim 0.66$ (Ravi et al. 2019). The total DM is reported to be $\mathrm{DM_{obs}} = 761\,\mathrm{pc\,cm^{-3}}$ (Bannister et al. 2019), with warm ISM contribution averaged over two models $\mathrm{DM_{ISM}} = 37$ (NE2001) and $30\,\mathrm{pc\,cm^{-3}}$ (YMW16) for the FRB direction $(l, b) = (117°, 44°)$. The MW halo DM of our model is $\mathrm{DM_{halo}} = 32^{+20}_{-20}\,\mathrm{pc\,cm^{-3}}$. Compared with the theoretical $\mathrm{DM_{IGM}} = 682\,f_{\mathrm{IGM}}\,\mathrm{pc\,cm^{-3}}$, f_{IGM} is constrained to $f_{\mathrm{IGM}} < 0.99$–1 using our halo DM model, while $f_{\mathrm{IGM}} < 0.94$–0.95 is derived using the high end value of PZ19.

3.6   Conclusions

In this chapter, we constructed a new model for DM associated with the extended hot gas halo in the MW, by taking into account the recent diffuse X-ray observation. Our hot gas halo model comprises of the two components: disk-like and spherical halo. The former is suggested by the recent diffuse X-ray observations, while the latter is theoretically introduced to make the total baryonic halo mass consistent with the cosmic baryon-to-dark-matter ratio. The radial profile of the spherical component is modeled by an isothermal gas under dynamical equilibrium with the dark matter halo potential of the MW. It is shown that the inclusion of the disk-like component is essential to explain the directional dependence of the observed EMs, which is in contrast to the previous models considering only the spherical halo.

Based on the newly proposed hot gas halo density profile, we derive the halo DM along any line of sight. Our model predicts a full range of $\mathrm{DM_{halo}} = 30$–$245\,\mathrm{pc\,cm^{-3}}$ over the whole sky, with a mean of $43\,\mathrm{pc\,cm^{-3}}$, which is slightly higher than the prevailing value ($30\,\mathrm{pc\,cm^{-3}}$) based on cosmological simulations (Dolag et al. 2015), but lower than the range preferred by a recent model of PZ19 (50–$80\,\mathrm{pc\,cm^{-3}}$). We provide a convenient analytic formula for the MW halo DM, which enables an easy estimate of $\mathrm{DM_{halo}}$ along any siteline toward extragalactic sources.

With the advent of large field-of-view surveys, such as CHIME and Apertif (van Leeuwen 2014), the number of nearby FRBs with $\mathrm{DM_{obs}} \lesssim 100\,\mathrm{pc\,cm^{-3}}$ (e.g., FRB 171020 with $\mathrm{DM_{obs}} = 114\,\mathrm{pc\,cm^{-3}}$ found by ASKAP; Shannon et al. 2018; Mahony et al. 2018, FRB 110214 with $\mathrm{DM_{obs}} = 169\,\mathrm{pc\,cm^{-3}}$ by Parkes; Petroff et al. 2019 and FRB 181030.J1054+73 with $\mathrm{DM_{obs}} = 104\,\mathrm{pc\,cm^{-3}}$ by CHIME; CHIME/FRB

Collaboration et al. 2019) is expected to increase in the foreseeable future. Since the total DMs of nearby FRBs might be dominated by the contribution from Galactic electrons, the estimate of $\mathrm{DM_{ISM}}$ and $\mathrm{DM_{halo}}$ would be more important.
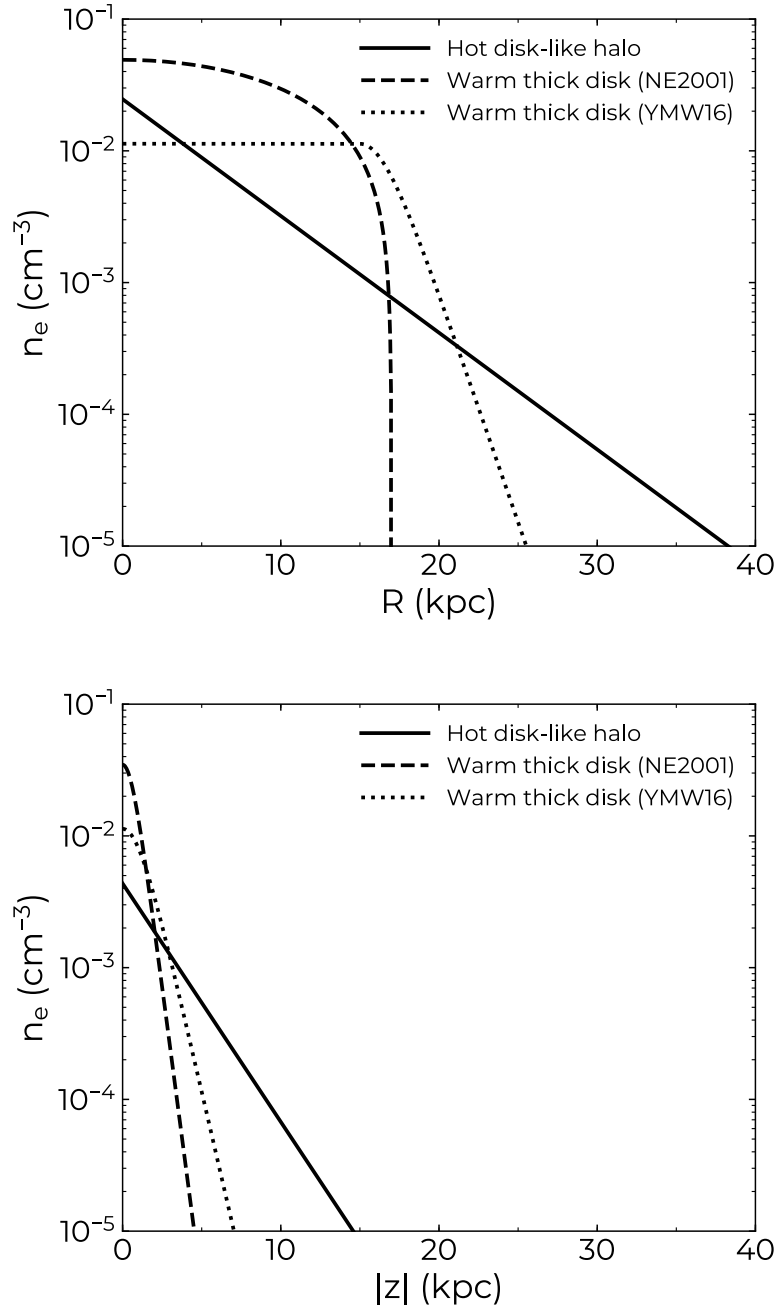
Figure 3.7: *Upper panel*: electron density plotted against Galactocentric radius in the in-plane (*R*-axis) direction from the Galactic center for the warm thick disk models and the hot disk-like halo; *lower panel*: electron density plotted against distance in the vertical (*z*-axis) direction from the Sun.
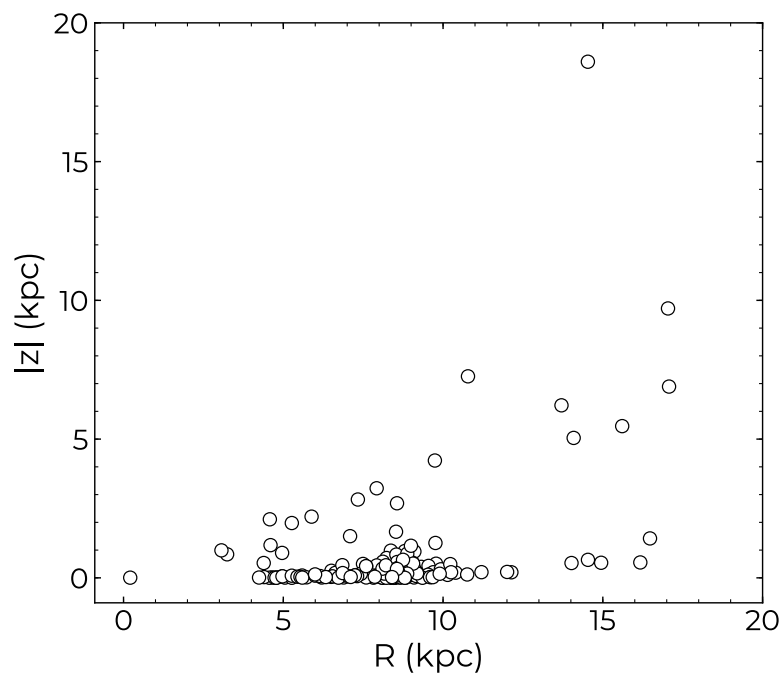
Figure 3.8: Spatial distribution of the 189 Galactic pulsars with DM-independent distances used to constrain the warm thick disk model of YMW16, which include a smaller ($N = 112$) sample of pulsars used for NE2001. The direction and distance information are adopted from Tables A1–A5 of YMW16.
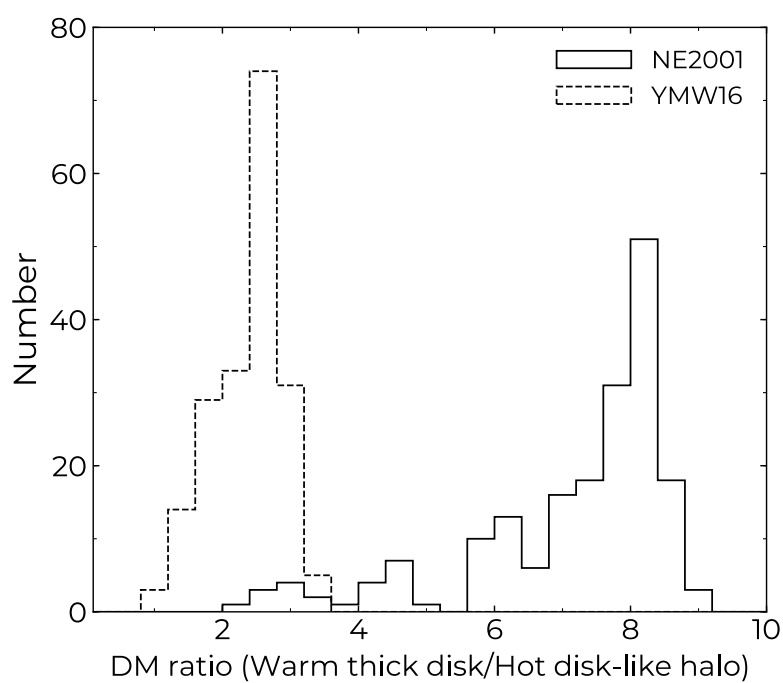
Figure 3.9: Histograms of DM ratio of the warm thick disk to the hot disk-like halo for the full sample of 189 Galactic pulsars shown in Figure 3.8.

Table 3.1:: Coefficients c_{ij} (in units of pc cm^{-3}) in Equation (3.7).

c_{ij}	$j=0$	$j=1$	$j=2$	$j=3$	$j=4$	$j=5$	$j=6$	$j=7$
				Disk-like + Spherical ($n=7$)				
$i=0$	250.12	-871.06	1877.5	-2553.0	2181.3	-1127.5	321.72	-38.905
$i=1$	-154.82	783.43	-1593.9	1727.6	-1046.5	332.09	-42.815	0
$i=2$	-116.72	-76.815	428.49	-419.00	174.60	-27.610	0	0
$i=3$	216.67	-193.30	12.234	32.145	-8.3602	0	0	0
$i=4$	-129.95	103.80	-22.800	0.44171	0	0	0	0
$i=5$	39.652	-21.398	2.7694	0	0	0	0	0
$i=6$	-6.1926	1.6162	0	0	0	0	0	0
$i=7$	0.39346	0	0	0	0	0	0	0

c_{ij}	$j=0$	$j=1$	$j=2$	$j=3$				
			Spherical ($n=3$)					
$i=0$	25.325	-1.4255	-1.0546	0.17295	–	–	–	–
$i=1$	-2.1749	1.4311	0.44722	0	–	–	–	–
$i=2$	-0.37683	-0.27977	0	0	–	–	–	–
$i=3$	0.16103	0	0	0	–	–	–	–

Part II

Magnetar Flares

Chapter 4

A Missing Link Between Magnetar Flares and Radio Pulsations

The work presented in this chapter originally appeared in:*Yamasaki, S., Kisaka, S., Terasawa, T., & Enoto, T. Relativistic Fireball Reprise: Radio Suppression at the Onset of Short Magnetar Bursts. MNRAS, 483, 4175–4186, 2019.*

4.1 Introduction

Magnetars (Duncan & Thompson 1992), an enigmatic class of highly magnetized neutron star, are known to exhibit flaring activities, phenomenologically classified into "giant flares" (10^{44}–10^{47} erg s^{-1} emitted in several minutes), "intermediate flares" (10^{41}–10^{43} erg s^{-1}) or "short bursts" (10^{38}–10^{41} erg s^{-1} with duration ranging from a few milliseconds to a few seconds), as well as large and sudden increases (factor of 10–1000 up to 10^{36} erg s^{-1}, lasting $\lesssim 1$ yr) of the persistent emission ("outbursts") which often accompany a variety of anomalies in radiative behaviors (see Rea & Esposito 2011; Kaspi & Beloborodov 2017 for recent reviews). Among them, short bursts are the most common events, displaying a variety of underlying duty cycles. While some short bursts have clustered distributions in time ("Soft Gamma-ray Repeaters"; SGRs), others do not ("Anomalous X-ray Pulsars"; AXPs). There is a variety of progenitor models proposed for magnetar flares; some of them are related to an internal instability that leads to the sudden ejection of magnetic energy from the core into magnetosphere (Thompson & Duncan 1995, 2001), while others to an external release of magnetic energy through magnetic reconnections (Lyutikov 2003; Gill & Heyl 2010; Yu 2012; Parfrey et al. 2013; Yu & Huang 2013).

Some magnetars are known to exhibit transient coherent radio pulsations during their burst active phases (e.g., Camilo et al. 2006; Camilo et al. 2007b), suggesting possible connections to radio pulsars. Meanwhile, magnetar-like short bursts have been discovered from a radio pulsar (Göğüş et al. 2016; Kennea et al. 2016; Younes et al. 2016). Under such circumstances, any isolated neutron star with magnetar-like activity may potentially have radio pulsations, whereas any ordinary radio pulsar that seems in burst-inactive states can occasionally show bursting activities (Kaspi & McLaughlin 2005). Therefore, the number of neutron stars that exhibit both radio pulsations and bursting activities could be potentially large and considerably increased by future wide-field transient surveys.

Furthermore, Archibald et al. (2017) have recently reported an observation of magnetar-like short bursts from a radio pulsar PSR J1119–6127, which coincide in time with the suppression of periodic radio emissions (see Figure 1.4). For each short burst, the persistent 1.4 GHz radio flux initially gets suppressed, followed by the recovery to its quiescent level on time scale of $\sim$ 10–100 s, which is much longer than the spin period of the pulsar ($P \sim 0.4$ s), requiring new explanations. Given such relationship between radio pulsations and bursting activities, considering both might enable us to gain new insights into the burst mechanism. In this chapter, we propose a model for radio suppression mechanism at the onset of short bursts, getting inspirations from the intriguing findings by Archibald et al. (2017). We give a brief overview of our model in what follows (see also Figure 4.1).

We consider a situation that short bursts occur in an isolated neutron star with pulsed radio emissions. Note that we do not necessarily suppose radio pulsars or magnetars, and thus our model is of wide application. A sudden deposition of the magnetic energy into the magnetosphere may generate an extremely optically thick, compact photoleptonic plasma (so-called "fireball"). The fireball eruption is expected to occur at the top of the magnetic loop in analogy with solar flares (e.g., Lyutikov 2006; Masada et al. 2010). Depending on the pressure balance between the fireball and the magnetic field at the fireball formation site, the fireball is instantaneously driven to expand relativistically by its own internal pressure, acquiring a bulk Lorentz factor of $\sim 10^3$ (see eq. [C.20] in Appendix C).

As a consequence of the fireball expansion, the magnetosphere is covered by a dense $e^{\pm}$ plasma of the fireball, which would make the local plasma cutoff frequency many orders of magnitude larger than radio frequencies ($\sim$ GHz). Pulsar radio emissions are generally considered to be related to the particle acceleration above the polar cap region, which is defined by the last open magnetic field line. We assume that a similar radio emission mechanism is operated in bursting neutron stars. The generation of radio pulses is expected to continue during the fireball expansion, while

the surrounding environment becomes dense enough to prohibit the radio emission to propagate. Therefore, whatever the radio emission mechanism is, pulsed radio emissions (if exists) would be inevitably suppressed until the local plasma density sufficiently decreases as the fireball expands. The recovery timescale of the radio emission is determined by the initial fireball properties.

In addition to the outflowing plasma component discussed above, we also consider the inflowing plasma component, which includes a trapped fireball that remains confined to the stellar surface by the closed magnetic fields (Thompson & Duncan 1995). At the onset of the fireball formation, some fraction of the fireball plasma may drift downward along the magnetic loop, bombarding the footpoints (loop base) effectively, which may in turn lead to the formation of a hot spot at the surface of the neutron star. Depending on the energy deposited by the particle inflow, the hot spot emanates soft X-ray emissions lasting ~ 0.1 s, observed as short bursts often seen in the magnetar population. Meanwhile, the outflowing plasma component might also emanate electromagnetic (EM) radiations, which could be observed as a smoking gun. We consider this possibility and thereby show that the fireball itself produces photospheric emission in hard X-ray to MeV gamma-ray range after entering the optically thin regime, although the detection is challenging due to its extremely short duration ($\sim \mu$s).

This chapter is outlined as follows. In Section 4.2, we describe the triggering mechanism of short bursts, putting an emphasis on the fireball evolution. We then examine the consequence of the fireball expansion, proposing a model for radio suppression by pair plasma in Section 4.3. The temporal behavior, spectrum and observability of the EM counterpart arising from the fireball photosphere is discussed in Section 4.4. Our radio suppression model is applied to the high-B radio pulsar with bursting activities (PSR J1119–6127) in Section 4.5.1, and implications for magnetar model of Fast Radio Bursts are presented in Section 4.5.2. Some discussions on the possibility of plasma lensing and conclusions will be given in Section 4.6. The detailed analytic derivation of the fireball evolution is summarized in Appendix C. In this chapter we often adopt a notation $Q_x = Q/10^x$ in cgs units and a unit $k_B = 1 = c$ (k_B and c are Boltzmann's constant and speed of light, respectively) regarding the temperature of the fluid (i.e., the temperature T and the electron rest mass energy m_e share the same dimension).
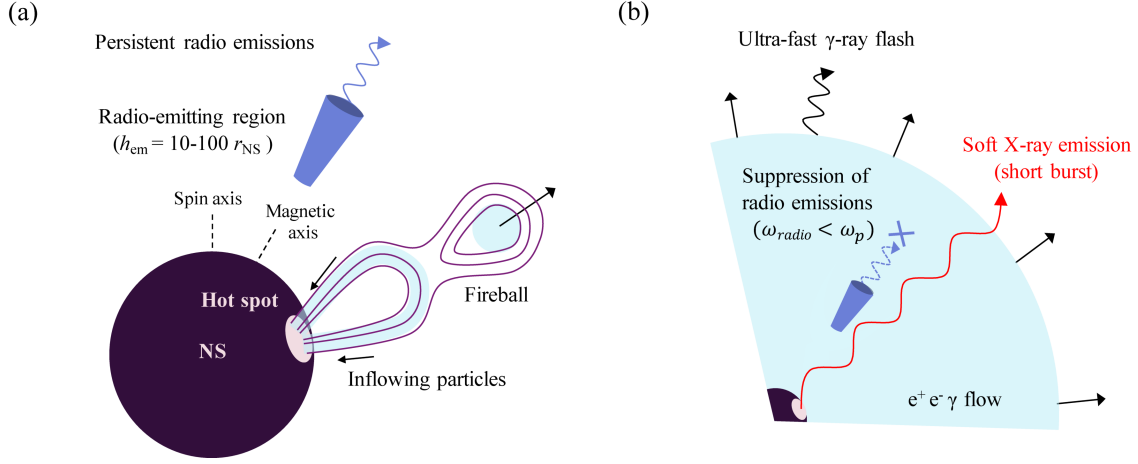
Figure 4.1: Schematic pictures of the model for short bursts and the radio suppression. (a) At the onset of the fireball release, a fraction of fireball plasma drifts downward along the magnetic loop and heats the surface of the neutron star, creating a hot spot. The pulsed radio emissions are assumed to be generated at altitude $h_{em} = 100$–1000 km above the neutron star surface. (b) After the fireball expansion, the radio emission site is covered by a dense $e^{\pm}\gamma$ plasma, which makes the plasma frequency significantly higher than radio frequencies, resulting in the suppression of radio emissions. While the hot spot on the stellar surface emanates soft X-ray emissions that is not affected by a plasma flow (the light-bending effect in the vicinity of the stellar surface is neglected for the purpose of presentation).

4.2   Event Trigger Mechanism

4.2.1   Fireball Expansion

A sudden release of pure energy into a relatively compact volume in the magnetosphere leads to the formation of a radiation-dominated $e^{\pm}$ pair plasma (so-called "fireball"). We consider a situation that the fireball is not trapped by the magnetic pressure in the magnetosphere. No sooner is the fireball formed than it frees itself from the confinement of the magnetic pressure and starts to expand. This is possible depending on the formation height and/or the magnetic field geometry near the surface of the neutron star (e.g., a highly non-dipolar configuration discussed by Huang & Yu 2014a,b; Yao et al. 2018).

The fireball is treated as a spherically evolving relativistic fluid composed of e^+e^- pairs plus γ photons (possibly with some baryons as discussed in Appendix C). Photons can be regarded as a relativistic fluid, since they are strongly coupled with pairs due to the extremely optically thick environment. The conservation of energy

and momentum for a steady hydrodynamical flow in spherical symmetry leads to a set of simple scaling laws that govern the radial evolution of the bulk Lorentz factor and temperature (Paczynski 1986; Goodman 1986). The bulk Lorentz factor increases linearly with r as $\Gamma \approx \Gamma_i(r/r_i)$ for $r < r_\infty$, where r_i is the initial fireball size and r_∞ the saturation radius above which the acceleration of plasma stops and fireball enters a coasting phase with an asymptotic bulk Lorentz factor Γ_∞. Meanwhile, the fireball temperature cools as $T \approx T_i(r/r_i)^{-1}$. The dynamical evolution of fireball is uniquely determined by initial fireball parameters r_i, T_i and Γ_i. For the sake of simplicity, we implicitly assume $\Gamma_i = 1$ and different values of r_i and T_i are tried.
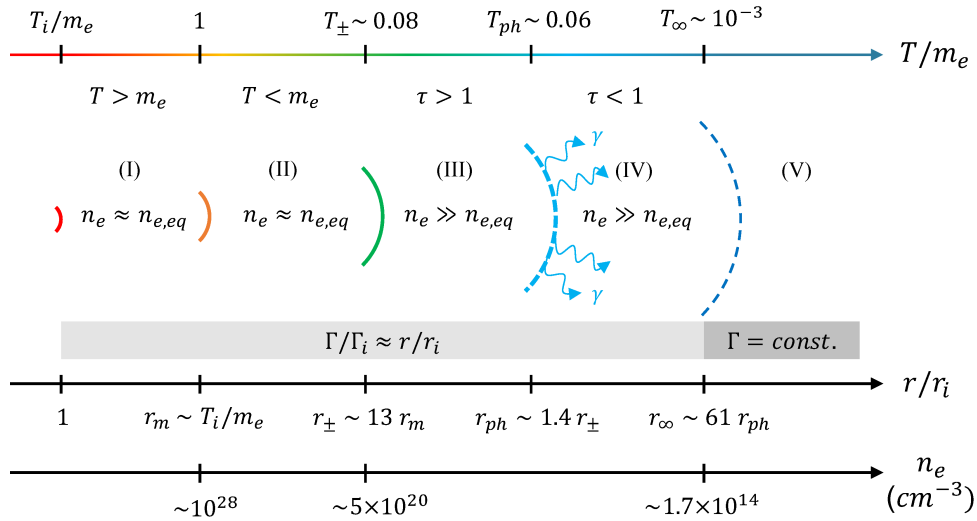
Figure 4.2: Schematic picture of the fireball evolution with an initial fireball size of $r_i = 10^5$ cm. The photospheric emissions expected during coasting phase (phase IV) are shown as wavy arrows, which would be observed as ultra-fast gamma-ray flashes. Variations of r_i do not significantly influence the scaling between adjacent critical radii (only $r_\pm/r_m$ weakly depends on r_i as $r_\pm/r_m \approx 13.4 + \log r_{i,5}$). See Appendix C for the detailed derivation of each value.

In addition to the dynamical evolution, we consider the evolution of the pair number density, taking into account the interactions among pairs and photons (i.e., creation and annihilation). We denote the number density of fireball electrons (equal to that of positrons) by n_e, and hence the net lepton number density $2n_e$. We assume that the fireball plasma starts to evolve from the equilibrium number density of electrons (and positrons) given as (Canuto & Ventura 1977; Thompson & Duncan

1995)

$$n_{e,\mathrm{eq}}(T) \approx \frac{2}{(2\pi)^{3/2}} \lambda_C^{-3} \, (T/m_e)^{3/2} \, e^{-m_e/T}$$

$$\sim 10^{28} \, (T/m_e)^{3/2} \, e^{-m_e/T} \quad \mathrm{cm}^{-3}, \tag{4.1}$$

where λ_C is the Compton length. The quantum effects under the magnetic field higher than the critical field strength $B_Q \equiv m_e^2 c^3/(e\hbar) \sim 4.4 \times 10^{13}$ G may change the equilibrium number density by a factor of $\sim B/B_Q$ (Harding & Lai 2006), but barely affect the result. To summarize, the evolution of electron (positron) number density n_e is characterized by several critical radii (see Table 4.1) that determine the physical properties of the fireball (Grimsrud & Wasserman 1998; Iwamoto & Takahara 2002; Li & Sari 2008):

(I)–(II) The initial fireball is at rest in pair equilibrium due to its high temperature with its size $r = r_i$. It immediately expands and cools down to the electron rest mass energy at $r = r_m$, and then the number density of pairs begins to deviate from the equilibrium number density at $r = r_\pm$.

(III) The pair annihilation dominates the pair process since the number of pair-creating high-energy photons decreases as the fireball cools. Eventually, the fireball reaches the photospheric radius $r = r_{ph}$ at which the optical depth to electron scattering becomes an order of unity.

(IV) When the fireball becomes optically thin, photons begin to leak freely out of the photosphere. However, they still continue to supply the radiation energy to pairs, which accelerates pairs up to the coasting radius $r = r_\infty$.

(V) The photons cease to inject the radiation energy to pairs, and the fireball begins to freely coast at constant speed $\Gamma = \Gamma_\infty$. The pair annihilation no longer occurs due to the small number density. Therefore, the total number of pairs conserves and the pair density evolves as $\propto r^{-2}$.

Finally, we obtain the radial evolution of the fireball from the analytic estimates as shown in Appendix C, which is also summarized in Figure 4.2. Hereafter, we often relate initial fireball parameters with the total fireball energy by

$$E_{\mathrm{fb}} = a T_i^4 r_i^3 \sim 10^{40} \, r_{i,5}^3 \left(\frac{T_i}{m_e}\right)^4 \quad \mathrm{erg}. \tag{4.2}$$

Although we adopt an initial fireball size of $r_i = 10^5$ cm as a reference assuming a typical total energy for short bursts $\sim 10^{40}$ erg, the results on radii presented in Figure

Table 4.1:: Description of critical radii that control the fireball evolution.

$r_i \cdots$	Initial fireball size
$r_m \cdots$	Electron temperature radius (at which $T = m_e$)
$r_{\pm} \cdots$	Pair equilibrium breakup radius
$r_{ph} \cdots$	Photospheric radius (at which $\tau \sim 1$)
$r_{\infty} \cdots$	Coasting radius

4.2 can be easily scaled to other values of r_i, since only $r_{\pm}/r_m$ is weakly dependent on r_i (see eq. [C.10]). These results will be used to estimate the time scale for radio suppression and recovery in Section 4.3.

4.2.2   Hot Spot Formation

At the onset of a fireball eruption, some fraction of the fireball plasma may be left at the loop top and stream downward along the magnetic loop. These energetic particles immediately bombard the loop base, which leads to create an inhomogeneity in temperature ("hot spot") at the stellar surface which might be comparable in size to the initial fireball. Although the formation of multiple hot spots is possible depending on configuration and size of magnetic loops, here we consider a single hot spot as a whole for simplicity. We assume that a fraction of the initial fireball energy E_{fb} is converted via the bombardment into the energy of the hot spot E_{rad}, which is immediately radiated away by the blackbody emissions. If the hot spot with radius r_{spot} cools by radiating thermal emissions with temperature T_{spot}, the phenomenological duration of the thermal radiation from the hot spot may be estimated as

$$\begin{aligned} \Delta t_{\mathrm{rad}} &\approx \frac{E_{\mathrm{rad}}}{\sigma_{\mathrm{SB}} T_{\mathrm{spot}}^4 4\pi r_{\mathrm{spot}}^2} \\ &\sim 80 \quad E_{\mathrm{rad},38} \, r_{\mathrm{spot},5}^{-2} \left(\frac{T_{\mathrm{spot}}}{10 \ \mathrm{keV}}\right)^{-4} \ \mathrm{ms}, \end{aligned} \tag{4.3}$$

where σ_{SB} is the Stephan–Boltzmann constant. Here we adopt a typical blackbody temperature ~ 10 keV for $E_{\mathrm{rad}} \sim 10^{38}$ erg burst (e.g., 2016 July bursts of PSR J1119–6127, Göğüş et al. 2016). While the hot spot size r_{spot} could presumably be related to the initial fireball size r_i as $r_{\mathrm{spot}} \approx r_i$ as far as $r_i \lesssim 10^6$ cm, the hot spot temperature is expected to linearly scale with the total energy of radiation as $E_{\mathrm{rad}} \propto T_{\mathrm{spot}}^4$. This implies that the duration of the flare estimated above would be almost constant for a wide range of observed radiation energy $E_{\mathrm{rad}} = 10^{36}$–$10^{41}$ erg, which is broadly consistent with the peak ~ 100 ms in the duration distribution of short bursts (Kaspi & Beloborodov 2017). The efficiency of the surface radiation $E_{\mathrm{rad}}/E_{\mathrm{fb}}(\lesssim 1)$ is highly

uncertain due to the lack of knowledge on the energy dissipation process at the neutron star surface[1]. Given the smaller size and the higher temperature of the hot spot compared to the whole stellar surface, the resulting emission should be observed as pulsed emissions, whose pulsed fraction could be either small or large, depending on the geometry relative to the observer.

4.3 Radio Suppression by $e^\pm$ Pair Outflows

4.3.1 Persistent Radio Emissions from Magnetars

Up to the present, coherent radio pulsations have been detected from only four magnetars, all of which are transient, emerging in coincidence with X-ray outbursts (Camilo et al. 2007a,b; Levin et al. 2010; Kaspi et al. 2014). The high-energy radiation of magnetars is generally considered to be powered by the magnetic energy, since its characteristic quiescent X-ray luminosity 10^{34}–10^{36} erg s^{-1} (Rea & Esposito 2011) is in excess of the rotational energy loss rate due to the magnetic braking (so-called "spin-down luminosity") $L_{\rm sd} = 3.9 \times 10^{35}\, B_{14}^2 R_6^6\, P^{-4}$ erg s^{-1} = 10^{32}–10^{34} erg s^{-1} where R is the neutron star radius and $P = P/(1\ {\rm s})$. In contrast, radio pulsations from magnetars are normally well below $L_{\rm sd}$ (but brighter than for normal radio pulsars) and might be powered by the rotational energy (e.g., Szary et al. 2015). Namely, coherent radio emissions from magnetars may be generated by the relativistic plasma flow accelerated outwards along the open magnetic field lines with an emission altitude of $h_{\rm em} = 10$–$100\,R$ above the stellar surface, as is likely the case for conventional radio pulsars. In that case, the persistent radio emission from magnetars should be beamed as radio pulsars although the beam size could be temporarily changed by the bursting activity (e.g., Beloborodov 2009; Szary et al. 2015). The transient, low-efficiency, and anisotropic nature of radio emission all indicate that the detection rate of pulsed radio emissions of magnetars could be low, which is consistent with observations. Given the circumstantial evidence above, we assume that a similar radio emission mechanism operates both in magnetars and radio pulsars.

---

[1]A larger radiation efficiency $E_{\rm rad}/E_{\rm fb} \gtrsim 1$ might be possible if the formation height of the fireball plasma is so high that the inflowing plasma attains a significant gravitational energy.

4.3.2 Radio Suppression and Recovery

When the fireball begins to expand, the surrounding environment of the radio-emitting region is covered by a fireball plasma. In general, the motion of a charged particle is strongly confined along the magnetic field line inside the magnetosphere, and the fireball plasma cannot interact with particles that are responsible for radio emissions. For this reason, we can reasonably assume that the generation of radio emissions continues during the fireball expansion.

As a consequence of an expanding plasma flow, however, it is expected that any radio emission at $\sim$ GHz frequencies arising in the magnetosphere would suffer from the absorption. Here we consider a radio suppression due to the damping of waves by the pair plasma as a relevant absorption process. The plasma frequency of the fireball outflow measured in the observer frame is defined as

$$\nu_p = \frac{\Gamma}{2\pi}\sqrt{\frac{4\pi n'_e e^2}{m_e}} \sim 9.0 \times 10^3 \, \Gamma \, n_e'^{1/2} \text{ Hz}, \qquad (4.4)$$

below which the radiation in general cannot propagate through the medium. Here Γ is the bulk Lorentz factor of the fireball and n'_e the electron number density measured in the comoving frame of the fireball plasma. The evolution of n'_e and ν_p under different initial conditions is shown in Figure 4.3 and Figure 4.4. One can see that the fireball is in the coasting phase [phase (V)] when the plasma frequency reaches observing radio frequencies $\sim$GHz. At this stage ($r \gg r_\infty$), the bulk Lorentz factor of the plasma stays constant $\Gamma = \Gamma_\infty$, and the electron number density decreases as $n'_e = n'_e(r_\infty)(r/r_\infty)^{-2}$. Substituting these to Equation (4.4), we can express the plasma frequency at phase (V) as a function of time ($t \sim r/c$):

$$\nu_p(t) \approx 4.7 \times 10^{11} \, r_{i,5}^{5/8} \left(\frac{T_i}{m_e}\right)^2 t^{-1} \text{ Hz}. \qquad (4.5)$$

Then, the characteristic time scale for the recovery of the pulsed radio emissions from suppression by the pair plasma defined by $\nu_p(\tau_{\text{off}}) = \nu \sim$ GHz is estimated as

$$\tau_{\text{off}} \approx 4.7 \times 10^2 \, r_{i,5}^{-7/8} \left(\frac{E_{\text{fb}}}{10^{40} \text{ erg}}\right)^{1/2} \nu_9^{-1} \text{ s}, \qquad (4.6)$$

where we have introduced the total fireball energy E_{fb} by using Equation (4.2) . From the observational perspective, τ_{off} is directly obtained by examining a radio light curve and r_i might be related to the observed hot spot size, both of which allow us to estimate the total fireball energy E_{fb}. Although a baryon-free fireball is implicitly

assumed here, the possible baryon contamination at the time of fireball formation does not significantly change our result. We estimate that the heavy baryon loading would increase ν_p only by a factor of $\lesssim$ a few (see Appendix C.3). One possible uncertainty in our model is the assumption on the isotropic expansion of fireball. Given the relatively large initial Lorentz factor of the fireball (e.g., $\Gamma_i \gtrsim 3$), it is expected that the fireball may expand in a highly anisotropic manner; this could result either in delayed radio suppression or none whatsoever. We leave the exploration of this possibility for a future work.

Intriguingly, the spectrum of pulsed radio emissions from four magnetars is known to be flat across wide frequency ranges (typically 1–100 GHz, Kaspi & Beloborodov 2017). A natural consequence of this is that the recovery of radio emissions from the complete suppression would take place gradually (not abruptly) while the plasma frequency passes through the spectrum energy ranges of magnetars. Given the observing frequency band $\nu \in [\nu_1, \nu_2]$ that is contained by the flat spectrum frequency ranges of magnetars, the radio emissions are completely suppressed ($\nu_p \gg \nu_2$) at early times, and then followed by the subsequent partial recovery phase ($\nu_p \in [\nu_1, \nu_2]$), whose time scale could be the same order as τ_{off} for a band width $\Delta\nu \sim \nu$.
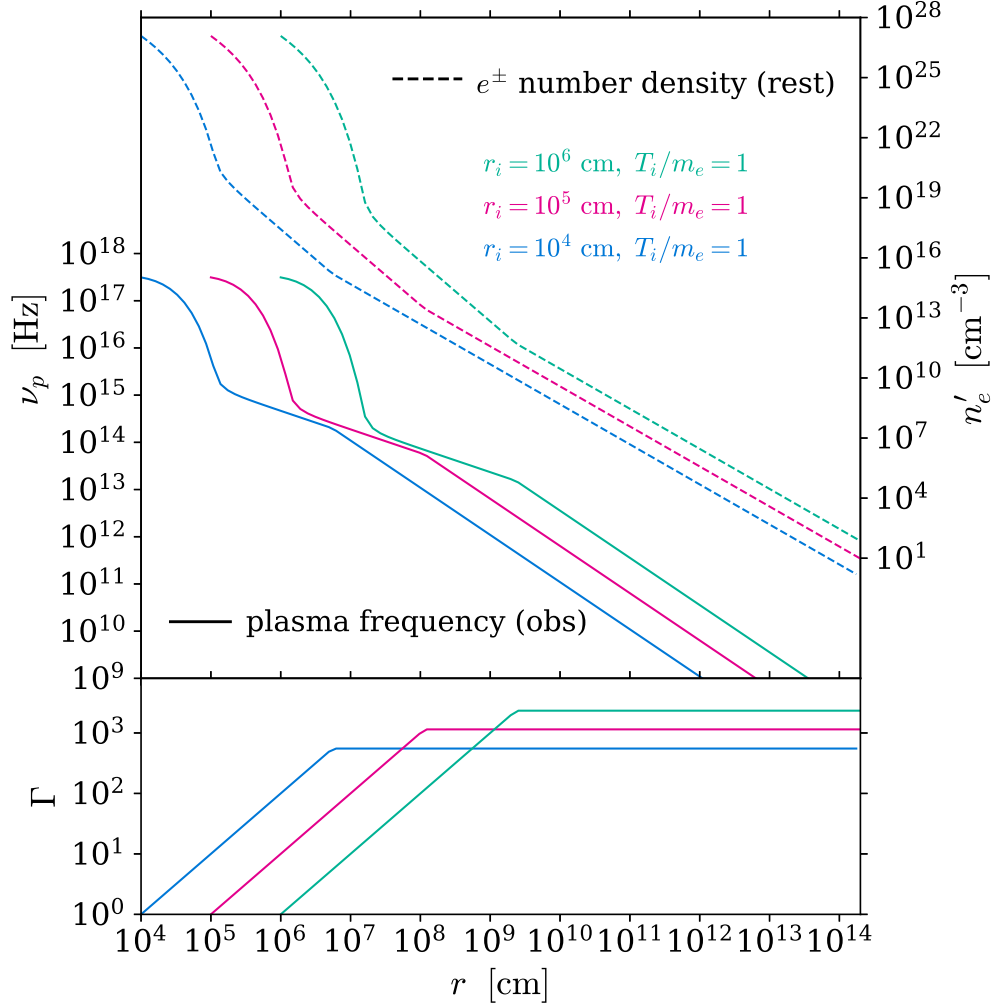
Figure 4.3: Evolution of the electron number density in the plasma rest frame (upper panels, dashed lines), plasma frequency in the observer frame (upper panels, solid lines) and bulk Lorentz factor of fireball plasma (lower panels) for different initial sizes (left) and temperatures (right). Equations (C.6), (C.11), (C.13) and (C.22) are combined to describe the overall evolution of n'_e, which is then translated into ν_p by using Equation (4.4) . The initial radius and temperature can be converted into the total fireball energy by using Equation (4.2).
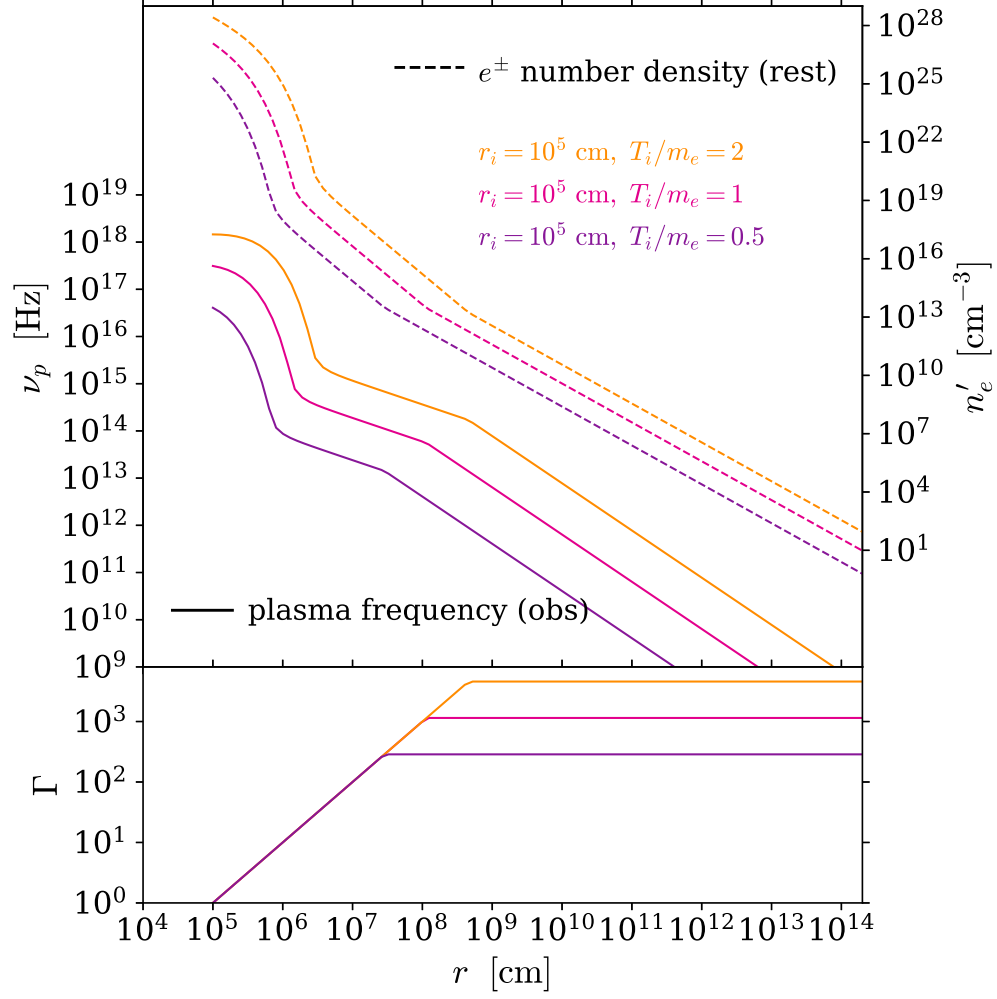
Figure 4.4: Same as Figure 4.3 but with different initial fireball temperatures.

4.4 High-energy Counterparts

In Section 4.2.2, we interpret observed short bursts as thermal emissions from the hot spot that is generated by particles inflowing toward the stellar surface. On the other hand, the expanding fireball is also expected to emanate radiations at times when it becomes optically thin. Detecting such a signature of the expanding fireball would be useful to examine the validity of our scenario presented in Section 4.3. Here we consider EM wave signatures from expanding fireball component, which should be distinguished from short bursts originated from inflowing component of the fireball plasma. While the rest frame temperature of the fireball decreases monotonically with increasing radius ($T \propto r^{-1}$), the emissions from the photosphere would be a blackbody with the Doppler-boosted temperature

$$T_{\rm obs} = \frac{T}{\Gamma(1 - \beta\mu)} \equiv \mathcal{D}T, \tag{4.7}$$

where $\beta\mu$ is the projection of the three velocity onto the line-of-site, and $\mathcal{D}$ being the Doppler factor. Because of the blue-shifted temperature (by a factor of $\mathcal{D} \sim 2\Gamma$–Γ for $\theta = 0$–$1/\Gamma$), the peak energy ranges relatively wider. The observed photospheric emissions would peak at $\epsilon_{\rm obs,peak} \sim 2\Gamma_{\rm ph}T_{\rm ph} \approx 2\Gamma_i T_i$, where we have used $\Gamma T = const$. The flux per energy interval received by a distant observer is given as

$$
\begin{aligned}
\mathcal{N}(\epsilon_{\rm obs}) &= \frac{4\pi\epsilon_{\rm obs}^3}{h^3 c^2} \int_{-1}^{1} \frac{\mu d\mu}{\exp(\epsilon_{\rm obs}/T_{\rm obs}) - 1} \\
&\approx \frac{4\pi\epsilon_{\rm obs}^2}{h^3 c^2} \frac{T}{\Gamma} \left\{ -\ln\left[1 - \exp\left(-\frac{\epsilon_{\rm obs}}{2\Gamma T}\right)\right] \right\}.
\end{aligned}
\tag{4.8}
$$

Using $T/\Gamma \propto r^{-2}$ and $\Gamma T = const$, the observed spectrum at $d = 10$ kpc is presented in Figure 4.5. The observed duration of the photospheric emission is expressed as

$$\delta t_{\rm obs} = \delta t(1 - \beta\mu) = \delta t' \Gamma(1 - \beta\mu) = \mathcal{D}^{-1}\delta t', \tag{4.9}$$

where $\delta t'$ and δt denote the time interval of emitted two photons in the source comoving frame and in the observer frame, respectively (hence $\delta t = \Gamma\delta t'$). We can see that the arrival time difference of the two photons is affected by both the Lorentz-boost and the purely geometrical effect. The burst lasts during phase (IV) in the source rest frame $\delta t' \sim r_\infty/c \lesssim 10^{-2}$ s. Therefore, the observed duration is extremely short: $\delta t_{\rm obs} \sim \delta t'/\Gamma_\infty \lesssim 10^{-5}$ s.

Let $\mathcal{N}_{\rm lim}$ be the onboard trigger sensitivity of a gamma-ray detector at observing energy $\epsilon_{\rm obs}$ with sampling time window $t_{\rm exp}$. In general, detectors are optimized for
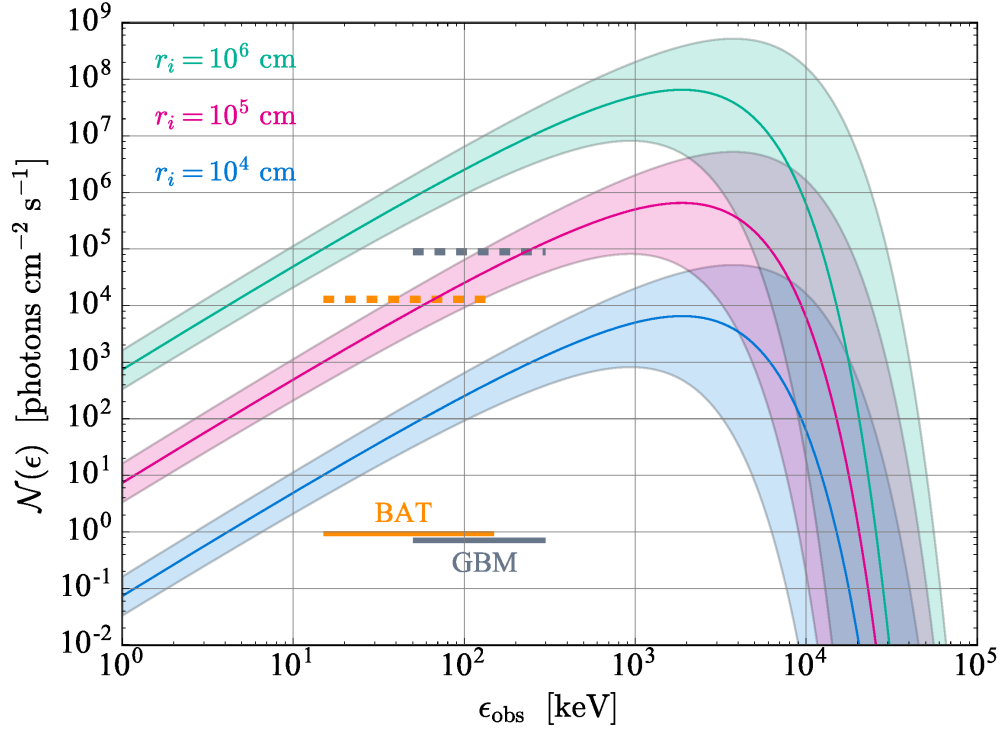
Figure 4.5: Expected spectra of the photospheric emissions with different initial fireball sizes (same as Figure 4.3). Results for the initial temperature of $T_i = m_e$ are shown in solid lines with shaded regions corresponding to a factor of two higher and lower temperature. The initial radius and temperature can be converted into the total fireball energy by using Equation (4.2). The trigger sensitivities of BAT and GBM are shown in solid horizontal lines. The exposure-corrected sensitivities estimated using Equation (4.10) are also shown in dashed horizontal lines.

transients with duration longer than the minimum sampling time window $\sim \mathcal{O}(\text{ms})$. In the case of ultra-fast gamma-ray flashes with typical duration $\delta t_{\text{obs}} \sim \mathcal{O}(\mu s)$ ($\ll t_{\text{exp}}$), however, the trigger threshold should be corrected for the sampling time window as

$$\mathcal{N}_{\text{lim}}^{\text{app}} = \mathcal{N}_{\text{lim}} \times \frac{t_{\text{exp}}}{\delta t_{\text{obs}}}, \tag{4.10}$$

where $\mathcal{N}_{\text{lim}}^{\text{app}}$ is the apparent trigger sensitivity. Adopting $\mathcal{N}_{\text{lim}} \sim 0.21 \, (t_{\text{exp}}/1\,\text{s})^{-1/2} \, \text{cm}^{-2} \, \text{s}^{-1}$ (at $\epsilon_{\text{obs}} = 15\text{--}150$ keV, assuming mean photon energy of 60 keV) with the minimum sampling time window $t_{\text{exp}} = 4$ ms for the Neil Gehrels *Swift* Burst Alert Telescope (BAT, Barthelmy et al. 2005), and $\mathcal{N}_{\text{lim}} \sim 0.71 \, (t_{\text{exp}}/1\,\text{s})^{-1/2} \, \text{cm}^{-2} \, \text{s}^{-1}$ (at $\epsilon_{\text{obs}} = 50\text{--}300$ keV) with $t_{\text{exp}} = 16$ ms for the *Fermi* Gamma-ray Burst Monitor (GBM, Meegan et al. 2009), we estimate the apparent trigger sensitivity as shown in Figure 4.5. It

can be seen that the event triggering onboard may be challenging unless the initial fireball size is relatively large ($\sim 10^6$ cm). Still, it is particularly interesting to search the archival X-ray or gamma-ray data for photon events clustering within a sub-millisecond time window. Conversely, the ultra-fast photospheric emission discussed above is observable when the fireball energy is sufficiently high, and this could be the origin of initial gamma-ray spikes of giant flares (e.g., Thompson & Duncan 2001; Lyutikov 2006).

Another possible EM counterpart is afterglow emissions. In the case of giant flares, radio afterglow emissions have been detected from two sources (Frail et al. 1999; Gaensler et al. 2005). For instance, late-time observations of the radio afterglow from SGR 1806-20 set a constraint on the total kinetic energy of ejecta $\sim 10^{44}$ erg (Granot et al. 2006), which is in agreement with the fireball model if we take into account a heavy baryon loading (Li & Sari 2008) or possible magnetic loading (Lyutikov 2006). However, at relatively lower energies considered here ($E_{\rm fb} \lesssim 10^{40}$ erg), the expected kinetic energy of fireball plasma in the coasting phase falls far short of the energy required to power observable radio afterglows.

4.5   Applications

4.5.1   PSR J1119–6127

The radio pulsar PSR J1119–6127 was first discovered by Parkes 1.4 GHz pulsar survey with a spin period $P \sim 0.4$ s, spin-down rate $\dot{P} \sim 4 \times 10^{-12}$ s s^{-1} and spin-down luminosity of $L_{\rm sd} \sim 2.3 \times 10^{36}$ erg s^{-1} at 8.4 kpc (Camilo et al. 2000). These spin-down parameters indicate that PSR J1119–6127 is relatively young (with characteristic age 1.9 kyr) and its surface dipole magnetic field strength ($B \sim 4.1 \times 10^{13}$ G) is close to the critical field strength. Several short bursts were detected on 2016 July 27–28 by *Swift*–BAT and *Fermi*–GBM (Göğüş et al. 2016; Kennea et al. 2016; Younes et al. 2016) with a large flux increase in the soft X-ray band (outburst, Archibald et al. 2016), after which the radio pulsations became undetectable for two weeks and re-activated again (Burgay et al. 2016) with a change seen in the radio pulse profile (Majid et al. 2017).

More recently, Archibald et al. (2017) has reported the detection of three short bursts on 30 August 2016 (with an average energy of 10^{37} erg emitted within a few seconds) that coincide in time with the suppression of persistent radio fluxes (see Section 1.3.3; Figure 1.4). The burst spectrum is fitted with a blackbody with peak temperature ~ 2 keV, and the radiative area at $d = 8.4$ kpc distance is estimated to

be about 1 km. As a possible explanation for this, they interpret the short bursts as a thermal emission from the magnetically confined fireball (Thompson & Duncan 1995), and consider a leakage of a pair plasma from the trapped fireball into the particle-accelerating region, which would shield the electric field, resulting in the suppression of radio emissions. In that case, however, the cessation of particle acceleration should occur abruptly (with at most light-crossing time of the radio-emitting region $\sim$ ms) rather than continuously once the sufficient number of $e^{\pm}$ pairs is supplied (Lyubarsky 2009; Timokhin 2010b; Timokhin & Arons 2013; Kisaka et al. 2016), which seems contradictory with their interpretation of the "gradual" radio recovery (the radio light curve is fitted with an exponential recovery model with a typical time scale $\sim$ 70 s). Moreover, the formation of a fireball with its surface temperature ($\sim$ 2 keV), which is about three orders of magnitude lower than the internal temperature $m_e \sim 511$ keV, is unlikely. Furthermore, the cessation of the radio emission due to the leakage of pair plasma into polar cap region should last for at most a few seconds (assuming that the duration of short bursts is limited by the lifetime of the fireball), which is much shorter than the observed timescale for radio suppression $\sim \mathcal{O}(100 \text{ s})$.

Alternatively, we apply our general radio suppression model to PSR J1119–6127 below. The time scale for the radio recovery $\lesssim 100$ s could be accounted for by adopting fireball parameters of $r_i \sim 10^5$ cm and $T_i \sim 0.5\, m_e$ from Equation (4.6). This translates into an initial fireball energy of $E_{\rm fb} = a T_i^4 r_i^3 \sim 10^{38}$ erg, which is sufficiently large to generate short bursts from surface hot spots (i.e., with an efficiency $E_{\rm rad}/E_{\rm fb} \sim 0.1$). Substituting the observed blackbody temperature of the short bursts ~ 2 keV and the size of the radiating region $r_{\rm spot} = 10^5$ cm (Archibald et al. 2017) into Equation (4.3), we estimate the duration of the thermal emissions to be $\Delta t_{\rm rad} \sim 5\ E_{\rm rad,37}\, r_{\rm spot,5}^{-2}\, (T_{\rm spot}/2\text{ keV})^{-4}$ s, where we have assumed that about 10% of the fireball energy ($E_{\rm fb} = 10^{38}$ erg) is converted into radiation energy of the surface hot spot. This roughly agrees with the observed duration $\sim$ 2–4 s and the total radiation energy $\sim 10^{37}$ erg of three short bursts on August 30th 2016 (Archibald et al. 2017).

Furthermore, the problem of the magnetic confinement is easily solved if we assume a moderate formation height of the initial fireball. Given a dipole magnetic field $B \propto r^{-3}$, the magnetic pressure at an altitude $h_{\rm fb}$ above the stellar surface is $P_B = B^2/(8\pi) \sim 6.4 \times 10^{25} (B_p/4 \times 10^{13}\text{ G})^2\, h_{\rm fb,6}^{-6}$ erg cm^{-3}, whereas the total pressure of the fireball with initial temperature T_i is $P = P_e + P_r = 11/4\, P_r \sim 10^{24}\, (T_i/0.5\, m_e)^4$ erg cm^{-3}, where P_e and P_r are plasma pressure and radiation pressure, respectively. The fireball therefore can escape from the magnetic trapping (i.e., $P \gtrsim P_B$) when the initial condition $h_{\rm fb} \gtrsim 20$ km is satisfied. This critical height could be even smaller if the magnetic field is dominated by the higher multipoles

close to the neutron star surface. The non-detection of the high-energy counterparts associated with these short bursts is marginally consistent with the expected burst flux shown in Figure 4.5.

We also apply our model to the two-week disappearance of radio pulsations after the 2016 July 27–28th short bursts (Burgay et al. 2016). Given that the two-week radio suppression is caused by a single burst, the initial fireball energy must exceed 10^{48} erg, which is comparable to that of giant flares and thus seems unlikely. Instead, a viable scenario is that a series of short bursts that are too faint to be detectable occurred repeatedly or in succession during the initial outburst in July 2016, which suppressed the radio pulsation continuously for up to two weeks.

4.5.2 Fast Radio Bursts

Provided that the neutron star activity is directly responsible for the FRB generation, one possible trigger mechanism is magnetar flares (e.g., Popov & Postnov 2010b; Lyubarsky 2014; Kulkarni et al. 2015; Pen & Connor 2015; Katz 2016; Murase et al. 2016; Beloborodov 2017; Metzger et al. 2019). The minimum requirement for these models is that the flare energy must exceeds that of typical FRBs (10^{38}–10^{40} erg). As shown in the upper panel of Figure 4.3 and Figure 4.4, our radio suppression model indicates that the $\sim$GHz radio emission associated with an expanding plasma must originate at the distance $r_{\rm em} \gtrsim 10^{13} \, r_{i,5}^{5/8}(T_i/m_e)^2 \nu_9^{-1}$ cm from the neutron star under the most optimistic FRB efficiency of order unity. This in turn rules out any FRB models that predicts the radio wave generation in the vicinity of the neutron stars (i.e., inside the magnetosphere $\lesssim 10^{10}$ cm). In contrast, our model prefers scenarios in which FRBs are generated outside the magnetosphere, e.g., by the maser emission due to the termination shock (Lyubarsky 2014) or the internal shocks (Beloborodov 2017). In such cases, our model predicts that an FRB should occur at least $r_{\rm em}/c \sim 100$ s behind the giant flare.

4.6 Discussion and Conclusions

In this chapter, we investigated relativistically expanding fireball plasma as a possible origin both for short bursts and simultaneous suppression of the persistent radio emission from bursting neutron stars.

A sudden release of the magnetic energy inside the magnetosphere generates a fireball composed of $e^{\pm}$ plasma and radiation. Under the condition that the radiation

pressure of the fireball exceeds the magnetic pressure, the fireball begins to expand at relativistic speed, covering the magnetosphere with dense $e^{\pm}$ plasma. This would lead the plasma frequency to greatly exceed the radio frequency in the rest frame of the plasma, resulting in suppression of the persistent (pulsed) radio emission of bursting neutron stars. We analytically derive the radial evolution of the plasma number density, and estimate the characteristic time scale for the recovery of radio suppression to be ~ 100 s for a $\sim 10^{40}$ erg fireball. On the other hand, some fraction of the fireball plasma may heat the stellar surface via the particle bombardment, creating hot spots. The particle energy is converted to the hot spot and immediately radiated away as a thermal emission, which can give rise to a short burst with typical duration of ~ 100 ms. The ultra-fast gamma-ray flashes from the expanding fireball photosphere are expected as a smoking gun, although the onboard detection by current gamma-ray telescopes might be challenging due to its extremely short duration $\sim \mu$s.

Then we applied our hypothesis to the radio pulsar PSR J1119–6127 with magnetar-like short bursts. The observed radio suppression timescale $\lesssim 100$ s is well explained by fireball parameters of $r_i \sim 10^5$ cm and $T_i \sim 0.5\, m_e$, corresponding to an initial fireball energy of $aT_i^4 r_i^3 \sim 10^{38}$ erg. This also permits $\sim 10^{37}$ erg short bursts at ~ 2 keV. The expected gamma-ray counterpart has not been reported yet for J1119–6127, presumably due to the detector's sensitivity limit. However, an archival search for clustered photon events in an extremely short time window contemporaneous with the time of short burst detection would be highly intriguing. Our model can naturally explain the J1119 observations well, and this might be one of the causes of the nulling and mode-changing commonly seen in radio pulsars. The implications for FRBs are also discussed. Provided that FRBs are generated by a plasma outflow that is also responsible for magnetar flares, we argue that the radio emission must be produced at $r \gtrsim 10^{13}$ cm from the neutron star, which is a minimum requirement to avoid the absorption by the plasma cutoff effect.

Our fireball model naturally accounts for the radio suppression associated with bursting activities in J1119–6127. Since the plasma frequency decreases with time, the timescale for radio suppression would be shorter for higher frequencies. Namely, a solid proof of our model would be provided by future simultaneous observations of neutron stars with radio pulsations at X-ray and at *multiple* radio bands, during a period of magnetar flares. However, it should be noted that similar radio switch-off phenomena called "nulling" and "mode changing" are commonly observed in radio pulsars. The global change in the magnetosphere is proposed as a possible mechanism for them (e.g., Wang et al. 2007; Timokhin 2010a). Indeed, as the duration of nulling and mode changing varies from one or two rotations to even days, one cannot exclude the possibility that they had played a role for ~ 100 s radio disappearance seen

in J1119–6127. The change in the average radio pulse profile of J1119–6127 also resembles those for mode changing pulsars (Archibald et al. 2017). Therefore, instead of ruling out this possibility, we only point out that our model could be related to nulling and/or mode changing. Particularly, a radio suppression caused by a fireball with its energy sufficiently low to remain undetected in X-ray bands would manifest as nulling. This might be the origin of some short-duration nulling events.

In most part of this chapter, we have treated the fireball plasma as radio absorber. After the recovery of radio pulses, however, it might also work as a plasma lens that leads to the light amplification, depending on the density fluctuation and the geometric configuration of radio pulses. Let us consider the simplified geometry shown in Figure 4.6 (a), when the pulsar rotation axis is perpendicular to its magnetic momentum. The observer is assumed to be located in the beam-plane which is perpendicular to the rotation axis, and ray paths in this plane are modelled as shown in Figure 4.6 (b). We consider a radio pulse that leaves the source at $t = t_\mathrm{p}$ ($> \tau_\mathrm{off}$) and reaches the lensing point at $t = t_\mathrm{lens}$, corresponding to a travel distance of $r_\mathrm{lens} = c\,(t_\mathrm{lens} - t_\mathrm{p})$. For simplicity, we assume that the plasma has a local fluctuation of $\Delta n_e \sim n_e$, which leads to the light refraction at $r = r_\mathrm{lens}$ with a pitch angle $\Delta\theta$. In general, the phase of an EM wave is given by the contributions of geometrical and dispersive (group) time delays over a whole ray path:

$$\Phi(u) = \Phi_g(u) + \Phi_\mathrm{DM}(u), \tag{4.11}$$

where u is the transverse coordinate in the lens plane. A minimum requirement for the strong lensing is $\Delta\Phi_g \sim \Delta\Phi_\mathrm{DM}$ so that $\nabla\Phi = 0$ at some spacial scales (Main et al. 2018).

The difference in geometrical distance between the wavefronts arises from ray paths outside the fireball plasma: $\overline{\mathrm{OL_1}} - \overline{\mathrm{OL_0}} = r_\mathrm{lens}\,[1 - \cos\,(\Delta\theta/2)]$, where $\overline{\mathrm{OL_0}}$ is the path length of the closest approach from the lens to the observer. This results in the geometrical phase change due to the source motion as

$$\Delta\Phi_g = \frac{\nu\,(\overline{\mathrm{OL_1}} - \overline{\mathrm{OL_0}})}{c} = \nu\,(t_\mathrm{lens} - t_p)\,\xi(\Delta\theta), \tag{4.12}$$

where $\xi(x) \equiv 1 - \cos\,(x/2)$. Meanwhile, the dispersive phase change is expressed as

$$\Delta\Phi_\mathrm{DM}(u) = -\frac{k_\mathrm{DM}}{\nu}\Delta\mathrm{DM}(u), \tag{4.13}$$

where $k_\mathrm{DM} = e^2/(2\pi m_e c) \sim 4148.808$ s pc^{-1} cm^{-3} MHz^2 is the dispersion constant and $\Delta\mathrm{DM} = \int n_e dz$ the excess of electron column density along the ray path. In the
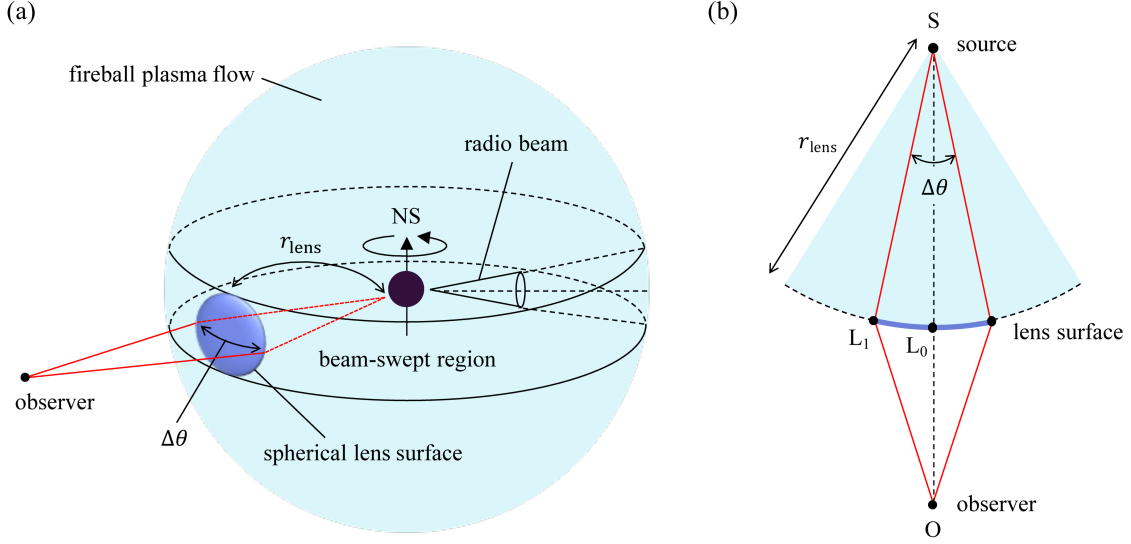
Figure 4.6: Geometries of scattering for a fireball plasma lens. (a) The observer is assumed to be located in the beam-plane which is perpendicular to the spin axis. The light blue sphere represents the fireball plasma that is responsible for the plasma lensing. We assume a circular radio beam and its projection onto the lens plane is shown as an equatorial belt ("beam-swept region"). Since the timescale for lensing must be much longer than the spin period in order to avoid the radio suppression, this beam-swept region can be regarded as being constantly radiating radio emissions. A light ray which intersects the spherical lens surface by the pitch angle $\Delta\theta$ is assumed to be deflected toward the observer. (b) Same as (a) but viewed in the beam-plane.

case of fireball plasma lens, the electron density evolution in the coasting phase is estimated as (eq. [C.22] in Appendix C)

$$n_e(t) = 2.3 \times 10^9 \; r_{i,5}^{-3/4} \, E_{\rm fb,40}^{1/2} \, t^{-2} \quad {\rm cm}^{-3}, \tag{4.14}$$

where t is the time from the burst onset, in units of seconds. The increase in the dispersion measure along each ray path is

$$\Delta{\rm DM} \;\; = \;\; \int_{t_p}^{t_{\rm lens}} n_e(t') \, c \, dt' \tag{4.15}$$

$$\sim \;\; 20 \; r_{i,5}^{-3/4} \, E_{\rm fb,40}^{1/2} \left(t_p^{-1} - t_{\rm lens}^{-1} \right) \quad {\rm pc \; cm}^{-3}. \tag{4.16}$$

Therefore, the dispersive phase change at $\sim$GHz frequencies is

$$\Delta\Phi_{\rm DM} = 8.3 \times 10^7 \; \nu_9^{-1} \, r_{i,5}^{-3/4} \, E_{\rm fb,40}^{1/2} \left(t_p^{-1} - t_{\rm lens}^{-1} \right). \tag{4.17}$$

Equating Equations (4.12) and (4.17), we obtain $t_{\rm lens}$ as a function of the pitch angle
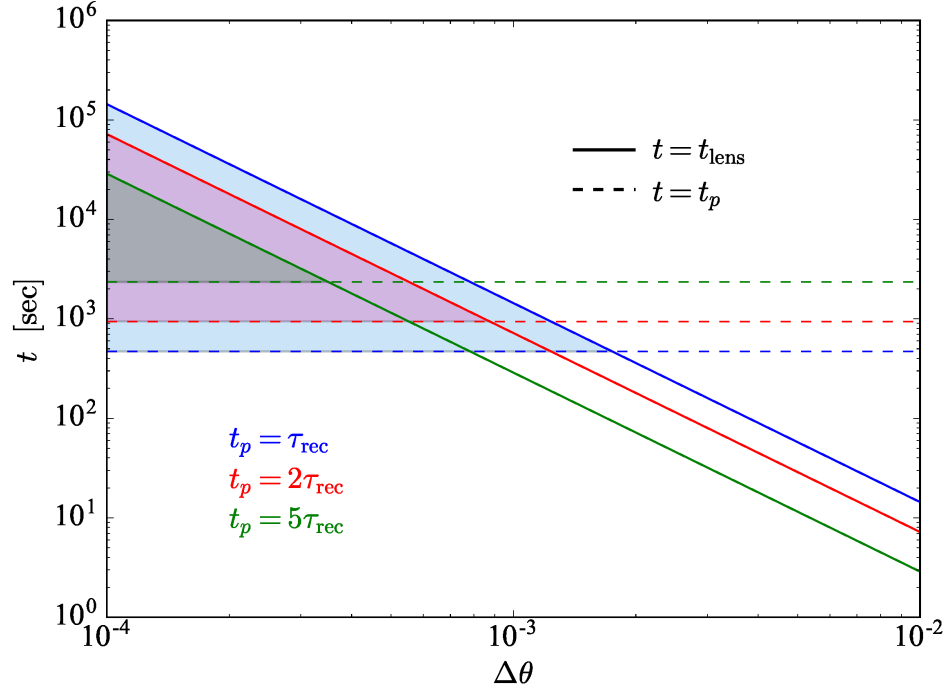
Figure 4.7: Constraints on the parameter space that might produce strong plasma lensing event: the elapsed time t since the burst onset and lensing pitch angle $\Delta\theta$ with assumptions of $t_p = \tau_{\text{off}}$, $2\tau_{\text{off}}$, $5\tau_{\text{off}}$ (colored). Solid lines and dashed lines represent the upper-limit (t_{lens}) and lower-limit (t_p) on the timescale of plasma lensing, respectively.

$\Delta\theta$

$$t_{\text{lens}} \sim 1.8 \times 10^{-4} \, \nu_9^{-1} \, r_{i,5}^{1/2} \left(\frac{t_p}{\tau_{\text{off}}}\right)^{-1} \xi(\Delta\theta)^{-1} \quad \text{sec.} \qquad (4.18)$$

The allowed parameter space for typical t_p are shown in Figure 4.7. This indicates that we can expect a strong lensing event on the order of $\gtrsim 10^3$ sec after the burst onset only when $\Delta\theta \lesssim 10^{-3}$. The pulse width for typical radio pulsars is roughly 1–10% of the spin period, so we cannot expect to find plasma lensing for ordinary radio pulses but for a radio pulse with sub-millisecond structures. Other possible candidates for strong plasma lensing are ultrashort duration pulses with widths of an order of sub-millimsecond ($\sim P\Delta\theta$), e.g., giant radio pulses in the Crab pulsar and FRBs.

In addition, the following prediction can be made based on our hypothesis. The fluence distribution of magnetar flares (from short to giant) are known to follow a single power-law (Cheng et al. 1996; Göğüş et al. 1999; Götz et al. 2006; Nakagawa

et al. 2009), implying that the number of bursts should dramatically increase with decreasing energy. In reality, however, bursts at the faint end of the energy distribution remain undetected owing to insufficient sensitivity of current X-ray detectors. Since our model predicts association of short bursts with radio suppression, there is a possibility that radio suppression could be used as a tracer of the short burst. Even for an extremely low-energy fireball with $E_{\rm fb} \sim 10^{34}$ erg, the corresponding radio shut-off time scale is $\tau_{\rm off} \sim 30 \, r_{i,3}^{-7/8} \, (E_{\rm fb}/10^{34}{\rm erg})^{1/2} \, \nu_9^{-1}$ s, which is much longer than the typical spin period of magnetars $\sim \mathcal{O}(1$ s$)$ and thus readily resolved in the radio light curve. Therefore, the radio monitoring of known radio pulsars or magnetars for which radio pulsations are confirmed would enable us to constrain the burst rate at lower energies. Such unresolved bursts may significantly contribute to the soft thermal component of persistent X-ray emissions from magnetars (Thompson & Duncan 1996; Lyutikov 2003; Nakagawa et al. 2018). The spectral similarities between short bursts and the persistent emission during the outburst phase also support this possibility (Enoto et al. 2012).

The Galactic search for pulsars with the Square Kilometer Array (SKA) is expected to yield $\sim 20,000$ new pulsars (Keane et al. 2015). Statistically, a small but significant fraction (say 1%) of these should be radio pulsars with magnetar-like bursting activities, which could be used to test our hypothesis through simultaneous radio and X-ray observations in the near future.

Chapter 5

Modeling the X-ray Spectra of Violent Magnetar Flares by Resonant Inverse Compton Scattering

The work presented in this chapter is based on an ongoing project and will be soon submitted to a referred journal.

5.1   Introduction

As introduced in Section 1.3, it is nearly established that magnetar flares are generated by a sudden release of the magnetic energy, which would result in the formation of a hot electron/positron plasma. With the exception of the initial short hard spike of giant flares, this plasma is confined to the stellar surface by the strong magnetic pressure, thereby forming an optically-thick bubble called "trapped fireball" (Thompson & Duncan 1995). The trapped fireball gradually cools by losing its energy through the radiation from its photosphere and occasionally manifests itself as a soft extended tail which shows high-amplitude pulsations over 1-100 s at the same spin period of an underlying neutron star (Thompson & Duncan 1995, 1996; Feroci et al. 2001). This is in contrast to the case of less energetic flares (Chapter 4), where the successful formation of the trapped fireball is not clear (Watts et al. 2010; Kaspi & Beloborodov 2017) and instead we consider the formation of hot spots.

An early consideration of energy transport in the trapped fireball predicted the

observed burst emission spectrum (the photon flux per unit energy) to appear almost flat at the Reighly-Jeans region and to remain the same as a blackbody at the Wien region (Ulmer 1994; Lyubarsky 2002; hereafter "modified blackbody"). This is due to the energy dependence of the opacity for photons in the extraordinary polarization mode expected under the presence of strong magnetic fields. This allows the lower energy photons to escape from deeper parts of the fireball, and thus the radiation at low energies emerges as a superposition of blackbodies, shaping the flat spectrum. Later, as demonstrated in Figure 5.1, the observed flaring spectra at soft X-ray energies turns out to be in good agreement with the model whereas the model significantly underpredicts the observed spectra at hard X-ray energies (e.g., Olive et al. 2004; Israel et al. 2008), and the discrepancy remains unsolved for more than a decade. The spectral formation of magnetar flares remains inconclusive areas.

The resonant inverse Compton scattering (RICS) may well be a plausible process that can interpret these observations of energetic flares. During the flare, photons emitted from the fireball should resonantly interact with the magnetospheric particles. At the resonance, the effective cross section exceeds the classical Thomson value by a few orders of magnitude, which makes the RICS most efficient process in the magnetar magnetosphere. Since scattering particles are expected to move in parallel to the magnetic field lines at the mildly relativistic speed, the energy of scattered photons would shift due to the relativistic Doppler effect. Hence, the velocity distribution of the scattering particles is of profound importance in the RICS.

The RICS has been primarily studied in the context of modeling the spectra of the quiescent magnetar emission (e.g., Thompson et al. 2002; Baring & Harding 2007; Lyutikov & Gavriil 2006; Fernández & Thompson 2007; Beloborodov & Thompson 2007; Nobili et al. 2008; Rea et al. 2008; Zane et al. 2011; Beloborodov 2013; Wadiasingh et al. 2018), which is less energetic (typically $L \sim 10^{35}$ erg s^{-1}) compared to magnetar flares by over several orders of magnitude. However, a detailed model of RICS during the burst phase has yet to be developed. In the quiescent state, the magnetospheric particles with relativistic and/or ultra-relativistic velocity may be present (Beloborodov & Thompson 2007), whereas during the flare, the intense radiation from the fireball exerts a strong radiation force to the magnetospheric particles and keeps their velocity mildly-relativistic (e.g., Thompson et al. 2002).

The aim of this work is to explain the observed spectra of energetic magnetar flares by particularly considering the distortion of the original fireball emission spectrum by the RICS. We develop a toy model for the scattering process during the flare and performing three-dimensional Monte Carlo simulation, taking into account both the angular velocity distribution of particles that is unique to flaring magnetospheres, and the realistic seed photon spectrum from the trapped fireball. Since

An intermediate flare spectrum
from SGR 1900+14 [Olive+04]
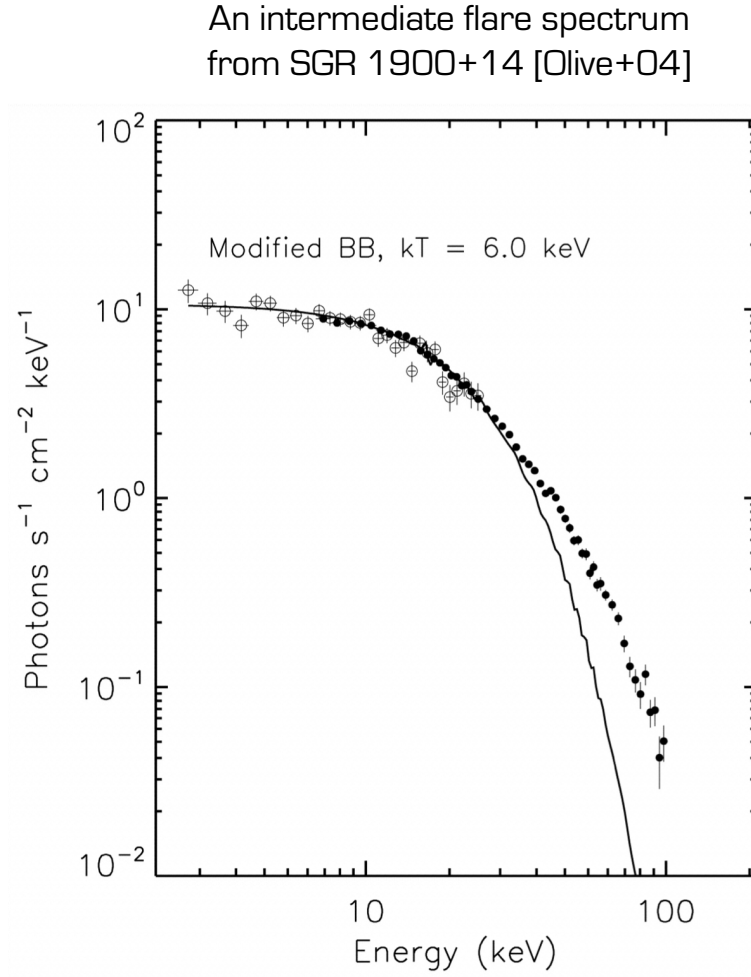
Figure 5.1: Comparison between the observed flare spectrum from SGR 1900+40 and the theoretical spectrum ("modified blackbody") proposed by Lyubarsky (2002) with an effective temperature of 6 keV (Figure 9 of Olive et al. 2004, adapted by permission of the AAS). The discrepancy between them at energies higher than ~ 30 keV is apparent.

our spectral model can be effectively described by a single parameter; the effective temperature of the fireball, this greatly reduces the complications and allows us to fit the observed spectra with low computational cost. Our model can be applied to energetic flares that include giant flares ($L = 10^{44}$–10^{47} erg s^{-1}) and intermediate flares ($L = 10^{41}$–10^{43} erg s^{-1}). Although a similar process may possibly operate in short bursts ($L = 10^{38}$–10^{41} erg s^{-1}) that are most commonly observed, whether the fireball successfully forms in short bursts remains unclear (e.g., Watts et al. 2010; Kaspi & Beloborodov 2017) due to its smaller energy dissipation rate as hinted by observations (e.g., Göğüş et al. 2000).

This chapter is organized as follows. In Section 5.2, we present the formulation of the model that we are simulating. We then describe in detail how to implement the simulation in Section 5.3, followed by the simulation result in Section 5.4. Implications of our model for observed burst spectra of SGR 1900+14 are discussed in Section 5.5.

5.2   Basic Formalism

Table 5.1:: Description of important quantities that control RCS.

$\epsilon_{i(f)}\cdots$	Initial (final) photon energy in the OF
$\omega_{i(f)}\cdots$	Initial (final) photon energy in the ERF
$\Theta_{i(f)}\cdots$	Initial (final) photon angle to the particle momentum (local magnetic field) in the OF
$\theta_{i(f)}\cdots$	Initial (final) photon angle to the particle momentum (local magnetic field) in the ERF
$\hat{\boldsymbol{k}}_{\boldsymbol{i(f)}}\cdots$	Unit vector of initial (final) photon momentum in the OF
$\vartheta\cdots$	Colatitude (polar angle) of initial photon
$\varphi\cdots$	Azimuthal angle of initial photon about $\hat{\boldsymbol{z}}$
$\Pi\cdots$	Azimuthal angle of scattered photon about $\hat{\boldsymbol{B}}$ in the ERF ($\Pi = 0$ in $\hat{\boldsymbol{B}}$-$\hat{\boldsymbol{z}}$ plane)

In the magnetar magnetospheres, an electron can be effectively treated being restricted to move along the magnetic field line (as beads threaded on a wire) in its lowest Landau level since it loses its gyro-momentum through the fast cyclotron cooling, which leads to the rapid decay of excited quantum states (Gonthier et al. 2000). In these conditions, a sequence of two independent processes; absorption and re-emission can be regarded as a single scattering with resonant cross section (e.g.,

Canuto et al. 1971)

$$\sigma_{\rm res}(\omega) = \pi^2 r_e c \, \delta(\omega - \omega_B)(1 + \cos^2 \theta_i), \tag{5.1}$$

where $\omega_B \equiv eB/(m_e c)$ is the cyclotron frequency in the electron rest frame (ERF) with B being the local magnetic field strength, $r_e \equiv e^2/(m_e c^2)$ the classical electron radius and θ_i the angle of incoming photon measured in the ERF with respect to the particle momentum (see also Table 5.1 and Figure 5.2 for other relevant properties introduced in this section). As the electron's momentum is parallel to the local magnetic field direction, B conserves between ERF and observer frame (OF).

Let us consider the thermal radiation from a magnetically-confined fireball formed during the magnetar flare. Here the fireball is approximated as a point-like source with isotropic emission at the center of the neutron star (see Section 5.3.2 for details). These photons are efficiently scattered by magnetospheric particles if the photon energy in the ERF satisfies a resonance condition:

$$\omega_i = \gamma_e \epsilon_i (1 - \beta_e \cos \Theta_i) = \hbar \omega_B \tag{5.2}$$

where γ_e is the Lorentz factor of a scattering particle, β_e the particle velocity in units of c, Θ_i the angle of incoming photon measured in the OF with respect to the particle momentum. In general, the location of the resonance layer depends on the magnetic field structure and the particle velocity distribution. For a dipole field geometry, the cyclotron energy of an electron at distance r from the stellar center can be written as

$$\hbar \omega_B \sim 1.1 \times 10^3 \left(\frac{B_p}{10^{14}\,\rm G} \right) \left(\frac{r}{R_{\rm NS}} \right)^{-3} \quad {\rm keV}, \tag{5.3}$$

where B_p is the polar magnetic field strength and $R_{\rm NS}$ the stellar radius for which we assume a typical value of 10 km. The resonance layer, at which the resonance condition $\epsilon_i \sim \hbar \omega_B$ is met, for $\epsilon_i \lesssim 10$ keV photons locates at $\gtrsim$ several stellar radii if the factor of $\gamma_e(1 - \beta_e \cos \Theta_i)$ is neglected. Therefore, the point-like assumption of the trapped fireball seems valid except for the most energetic giant flares that generate a trapped fireball with its size comparable to the altitude of resonance layer.

During the magnetar flare in the luminosity range of interest $L \gtrsim 10^{40}$ erg s^{-1}, magnetospheric particles should feel a strong radiation drag force. This is in stark contrast to the case of persistent emissions from magnetars in quiescent state, which is much less powerful $L \lesssim 10^{35}$ erg s^{-1}. We consider the following thought experiment on the motion of an electron under such a strong radiation force. The incident photon angle with respect to the local magnetic field in the ERF is related to the OF angle

by Lorentz transformation as

$$\cos\theta_i = \frac{\cos\Theta_i - \beta_e}{1 - \beta_e\cos\Theta_i}. \tag{5.4}$$

Thus, an electron moving parallel to the magnetic field with speed $\beta_e \sim 0$ (i.e., the right-hand side of eq. [5.4] is positive) is pushed forward by the radiation force ($\theta_i < \pi/2$), which leads to acceleration. Conversely, once the electron attains a relativistic velocity $\beta_e \sim 1$ (i.e., the right-handed side of eq. [5.4] is negative), it is pushed back by the radiation force ($\theta_i > \pi/2$), which leads to deceleration. Therefore, even if the electron does not "see" the photon with right angle, it would be immediately accelerated or decelerated to reach the equilibrium state, where the radiation force is directed perpendicularly to the magnetic field ($\theta_i = \pi/2$). Since the timescale for this regulation is negligibly short (see Appendix D), we can reasonably assume the above condition in the ERF, which allows us to uniquely determine the particle velocity in resonance with an incoming photon with Θ_i as

$$\beta_e = \cos\Theta_i; \qquad \gamma_e = 1/\sin\Theta_i. \tag{5.5}$$

A direct consequence of this angular velocity distribution might be the accumulation of decelerated plasma near the highest point of each closed magnetic field line (e.g., Beloborodov 2013). Tellingly, these particles might annihilate and emit $m_e c^2 \sim 511$ keV lines although it is highly dependent on the local plasma density and thus out of the scope of this work.

The scattering process does not change the photon energy in the ERF; $\omega_i = \omega_f$, since the majority of $\lesssim \mathcal{O}(10 \text{ keV})$ photons satisfies $\epsilon_i \ll m_e c^2/\gamma_e$ with $\gamma_e \sim \mathcal{O}(1)$ and thus the electron recoil is negligible. The scattered photon energy in the OF, ϵ_f, is related to the emission angle in the ERF, θ_f, through the Lorentz transformation of ω_f,

$$\epsilon_f = \gamma_e\omega_f(1 + \beta_e\cos\theta_f). \tag{5.6}$$

The photon emission angle in the ERF, θ_f, is in a random direction. A more detailed implementation will be described in Section 5.3.2. Finally, the photon emission angle in the OF, Θ_f, is obtained by

$$\cos\Theta_f = \frac{\cos\theta_f + \beta_e}{1 + \beta_e\cos\theta_f}, \tag{5.7}$$

which is equivalent to Equation (5.4) via the inverse Lorentz transformation.
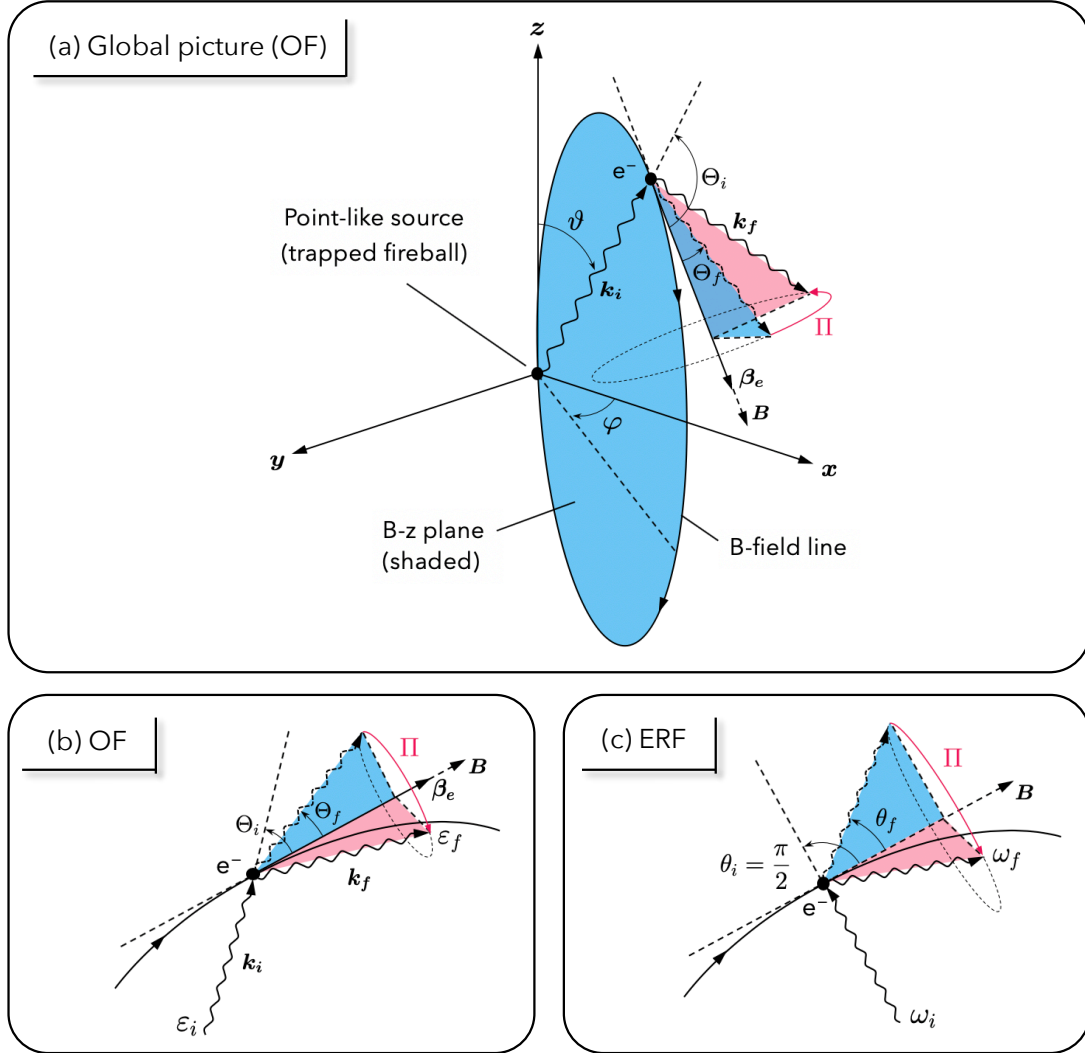
Figure 5.2: Scattering geometry in (a)–(b) the observer frame (OF) and (c) the electron's rest frame (ERF); all relevant angles and energies are indicated. The shaded region indicates the $\boldsymbol{B}$-$\boldsymbol{z}$ plane and the dipole magnetic moment is taken to be parallel to the z-axis (i.e., $\hat{\boldsymbol{\mu}}_B = \hat{\boldsymbol{z}}$).

5.3   A Toy Model

We aim to obtain the reprocessed spectrum of the fireball emission by injecting the seed photons by 3D Monte Carlo method. Below, detailed implementation and key assumptions are presented.

5.3.1   Model Geometry

In order to track a single photon trajectory, we adopt spherical coordinate r, θ, ϕ centered on the star with z-axis aligned with magnetic pole. When the twist of magnetic fields relative to magnetic poles is moderate, poloidal magnetic fields are well approximated as dipole (Thompson et al. 2002):

$$\hat{\boldsymbol{B}} = \frac{2\cos\theta\,\hat{\boldsymbol{r}} + \sin\theta\,\hat{\boldsymbol{\theta}}}{\sqrt{3\cos^2\theta + 1}},\tag{5.8}$$

where $\hat{\boldsymbol{r}}$ and $\hat{\boldsymbol{\theta}}$ denote basis vectors for polar coordinate. Since the scattering process is solely dependent on the configuration of magnetic fields that uniquely determine the particle velocity distribution (Section 5.2), no assumption is made on the magnetic field strength.

Although the emission from the point-like fireball is isotropic, the emission observed along a given line of sight might be modulated by the rotation of the star (which will be found not to be the case in Section 5.4). As a first step to obtain the spectra averaged over the entire rotational phase, we consider an aligned rotator in which magnetic axis is parallel to the spin axis ($\hat{\boldsymbol{\Omega}} = \hat{\boldsymbol{\mu}}_B = \hat{\boldsymbol{z}}$).

5.3.2   Scattering

Seed Photon Spectrum

We adopt a theoretical seed photon spectrum of a trapped fireball proposed by Lyubarsky (2002), who considered the detailed radiation transfer in the fireball under strong magnetic fields. The spectral formation inside the fireball is strongly affected by the presence of the two polarization modes with different scattering cross sections: the ordinary mode (O-mode: polarized in the $\hat{\boldsymbol{k}}$-$\hat{\boldsymbol{B}}$ plane) and extraordinary mode (E-mode: perpendicularly polarized to the $\hat{\boldsymbol{k}}$-$\hat{\boldsymbol{B}}$ plane). Since the scattering of the E-mode photons is significantly suppressed by a factor of $\sigma_{\rm E}/\sigma_{\rm O} \sim (\epsilon/\hbar\omega_B)^2 \sim$

$10^{-4}(\epsilon/10\,\mathrm{keV})^2(B/10^{14}\,\mathrm{G})^{-2}$ (Meszaros 1992), the photosphere of the E-mode photons lies far below that of O-mode photons. This allows the observer to see deeper into the fireball at lower energies, where each layer of E-mode photosphere should radiate a Planckian spectrum. As a result, the emerging spectrum from the trapped fireball has an analytic form:

$$N(\epsilon) \propto \epsilon^2 \left\{ \exp\left[\frac{\epsilon^2}{T_{\mathrm{eff}}\sqrt{\epsilon^2 + (3\pi^2/5)T_{\mathrm{eff}}^2}} \right] - 1 \right\}^{-1}, \tag{5.9}$$

where T_{eff} is the effective (bolometric) temperature of the fireball. The overall spectrum is characterized by a plateau at Rayleigh-Jeans region due to the energy dependence of the E-mode opacity ($\propto \epsilon^2$), which is in striking contrast to the commonly assumed Planckian spectrum. Before examining the broadband seed photon spectrum [eq. (5.9)], a monoenergetic spectrum with $N(\epsilon) \propto \delta(\epsilon - T_{\mathrm{eff}})$ will be explored in order to see qualitatively how our model redistributes the photon energy.

Photon Trajectory

Let us consider an initial photon emanating from the fireball located at the center of the coordinate. We define the unit momentum vector of initial photons in the Cartesian coordinate as $\hat{\boldsymbol{k}}_{\boldsymbol{i}} = (\sin\vartheta\cos\varphi, \sin\vartheta\sin\varphi, \cos\vartheta)$, where ϑ and φ are colatitude and azimuthal angle of initial photons, respectively. Assuming isotropic emission, $\cos\vartheta$ is chosen to be a random number in the range $[-1, 1]$, whereas φ is uniformly distributed in the range $[0, 2\pi]$. The incoming photon angle in the OF with respect to the local magnetic field line, Θ_i, is related to the initial photon colatitude, ϑ, via

$$\cos\Theta_i = \hat{\boldsymbol{B}} \cdot \hat{\boldsymbol{k}}_{\boldsymbol{i}} = \frac{2\cos\vartheta}{\sqrt{3\cos^2\vartheta + 1}}. \tag{5.10}$$

This allows us to determine the particle velocity (eq. [5.5]) and ERF cyclotron energy (eq. [5.2]) in resonance with the incoming photon as shown in Figure 5.3. The general relativistic effect on the photon trajectory (i.e., the light bending due to the gravitational redshift) is neglected because the altitude of the scattering layer is typically high ($\gtrsim$ several stellar radii) enough to avoid this.

Scattering Probability

In general, the scattering probability depends on the local plasma density, and we need to assume the spatial current distribution to know whether the scattering occurs
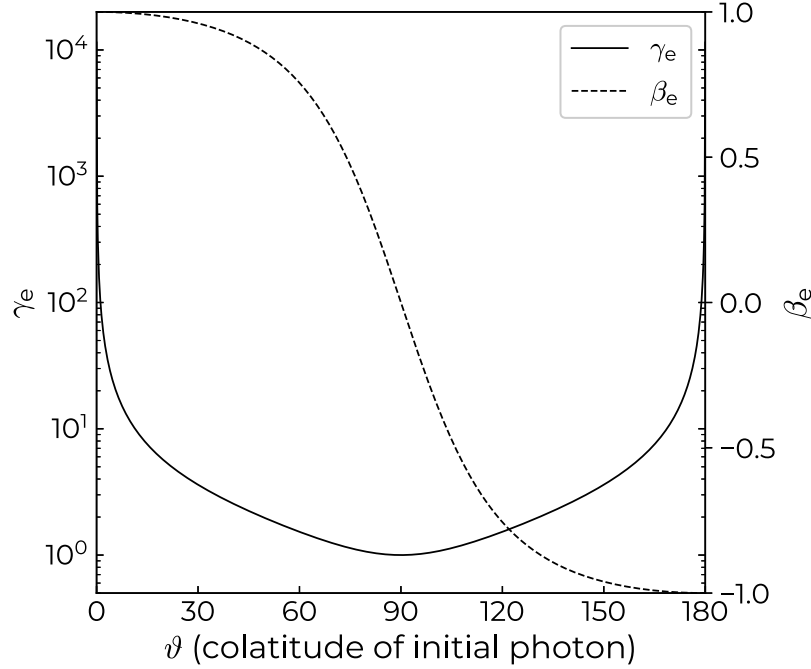
Figure 5.3: The velocity of a particle (γ_e and β_e) in resonance with the incoming photon with colatitude ϑ. Equations (5.5) and (5.10) are simply combined.

at the resonance point. This approach may be possible for the persistent emission from magnetars in a quiescent state, if the steady electric current is induced along the twisted field lines in a similar manner to that of the force-free magnetosphere (e.g., Thompson et al. 2002; Fernández & Thompson 2007; Nobili et al. 2008). However, during the flare, when a dense cloud of particles are anticipated to be newly supplied in the magnetosphere, the presence of such persistent currents is not trivial and hence a self-consistent treatment of the magnetosphere is not possible anymore. In order to avoid these complications, we presume that the plasma is sufficiently optically-thick to the resonant scattering (but optically-thin to the non-resonant scattering $\sigma_T/\sigma_{res} \lesssim 10^{-2}$), which is the case for bursting magnetospheres, and that all photons are scattered only once at 100% probability wherever the resonant condition is satisfied (e.g., Nobili et al. 2008). In reality, the scattered photon may meet the resonance condition even after the first scattering, which leads to the multiple scatterings. Yet, it seems reasonable to begin with the single scattering case and thus we leave the exploration of multiple scattering for future work. Remarkably, these assumptions make the scattering process entirely free from the magnetic field strength, the number density of the scattering particles and the polarization-dependence of the cross sections, and thereby considerably reducing the complexity of the model without loss

of generality.

Emission Angle

We follow the prescription by Fernández & Thompson (2007) to determine the direction of the scattered photons in the ERF. The differential cross section of resonant cyclotron scattering is proportional to

$$\frac{d\sigma_{\mathrm{res}}}{d(\cos\theta_f)\,d\Pi} \propto 1 + \cos^2\theta_f, \tag{5.11}$$

where Π is its azimuthal angle about the local magnetic field direction. Thus, the cumulative probability density of scattering into an angle $\leq \cos\theta_f$ is

$$p = \frac{1}{8}(\cos^3\theta_f + 3\cos\theta_f + 4), \tag{5.12}$$

which can be solved for $\cos\theta_f$ analytically:

$$\cos\theta_f = \left\{q + \sqrt{q^2+1}\right\}^{-1/3} - \left\{q + \sqrt{q^2+1}\right\}^{1/3}, \tag{5.13}$$

where $q \equiv 2 - 4p$. The distribution of $\cos\theta_f$ is uniquely determined by randomly generating p in the range $[0,1]$. Regarding the azimuthal angle about local magnetic field, we randomly choose Π in the range $[0, 2\pi]$ such that $\Pi = 0$ coincides with $\hat{\boldsymbol{B}}$-$\hat{\boldsymbol{z}}$ plane (see Figure 5.2).

5.4   Simulation

We generate a large sample (typically $N = 10^7$) of seed photons by Monte Carlo technique and treat their resonant interaction with particles probabilistically to obtain their post-scattering energies and momenta in the OF. Let θ_k be the colatitude of the scattered photon in the OF such that $\cos\theta_k = \hat{\boldsymbol{k}}_{\boldsymbol{f}} \cdot \hat{\boldsymbol{z}}$. The observer viewing angle is then defined as $\theta = \theta_v$, and photons with $|\theta_v - \theta_k| < \theta_{\mathrm{beam}}$ are sampled to obtain the reprocessed spectra, where θ_{beam} is the finite angular width that is centered on the observer orientation (we set $\theta_{\mathrm{beam}} = 1°$). Additionally, the spectra averaged over the entire viewing angles are also extracted. Since the scattered photon direction is axsymmetric about z-axis (magnetic axis), there is no phase dependence for aligned rotator.

Figure 5.4 illustrates the transmitted spectra for seed photons with a single
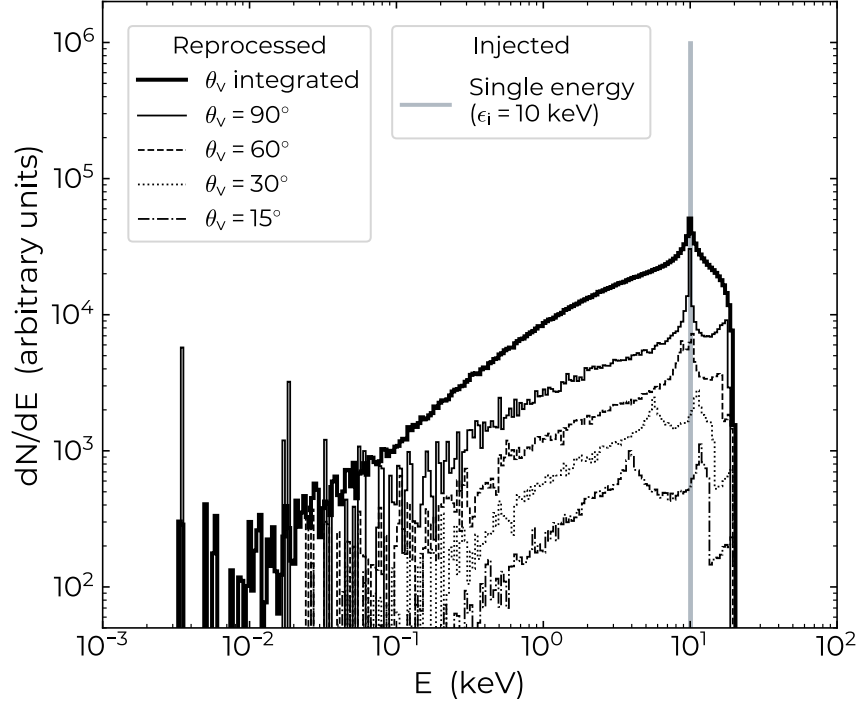
Figure 5.4: Spectral photon flux of RICS sampled for seed photons of energy $\epsilon_i = 10$ keV (thick gray solid histogram) which is typical energy of thermal X-rays emanating from fireball photospheres. The thick black solid histogram shows the reprocessed spectrum for photons averaged over the viewing angles. The thin black histograms (scaled for demonstration purposes) correspond to spectra of photons that fall into different viewing angles. Both upscattering ($\epsilon_f > \epsilon_i$) and downscattering ($\epsilon_f < \epsilon_i$) are exhibited.

energy $\epsilon_i = 10$ keV. Evidently, one can see the effect of both upscattering ($\epsilon_f > \epsilon_i$) and downscattering ($\epsilon_f < \epsilon_i$). Remarkably, the maximum degree of upscattering $\epsilon_f/\epsilon_i \sim 2$ is modest albeit fully consistent with the range that our model limits:

$$0 \leq \epsilon_f/\epsilon_i = 1 + \cos\Theta_i \cos\theta_f \leq 2, \tag{5.14}$$

where Equations (5.2), (5.5) and (5.6) are combined. This can be qualitatively understood as follows. Both (up- and down-) scatterings are pronounced when $|\cos\Theta_i \cos\theta_f| \sim 1$. If one considers, for example, a case of $\cos\Theta_i \sim 1$ and $\cos\theta_f \sim \pm 1$, this indicates a relativistic velocity of the scattering particle $\beta_e = \cos\Theta_i \sim 1$ (see eq. [5.5]) in our model. Such a photon scatters the photon in a parallel direction to the local magnetic field in the OF (i.e., the relativistic limit $\cos\Theta_f \to 1$ ($\beta_e \to 1$) in eq. [5.7]) independent of the ERF emission angle θ_f. Meanwhile, $\cos\theta_f \sim \pm 1$
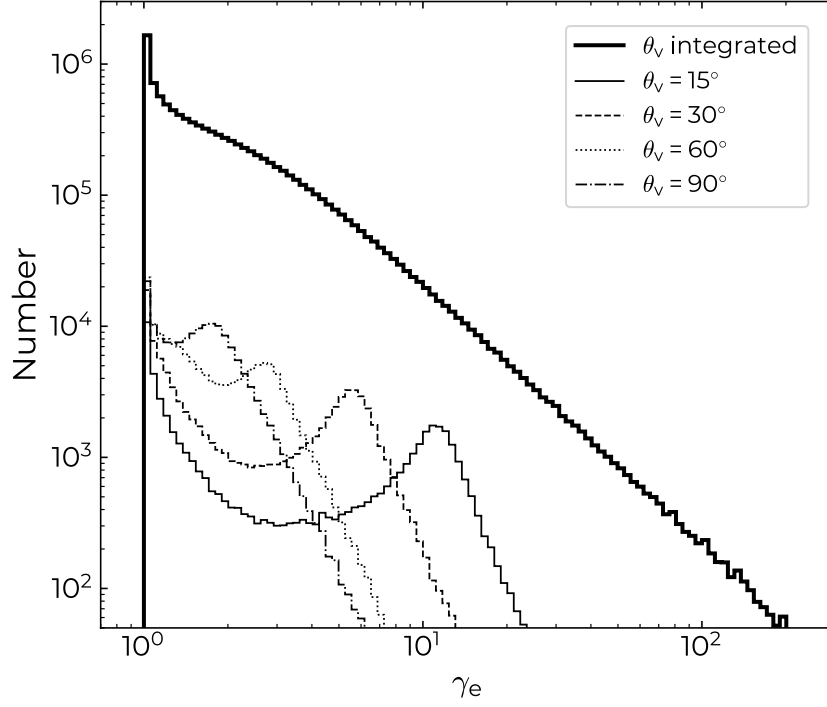
Figure 5.5: Lorentz factor distribution of electrons that scatter photons in different viewing angles (shown as thin black histograms). The result for all (integrated over the viewing angles) resonant electrons is shown as a thick black solid histogram, which demonstrates that the majority of scattering particles move at the mildly-relativistic velocity.

can be realized with a certain probability since $\cos\theta_f$ is uniformly sampled from the range $[-1, 1]$. Therefore, the strong (up- and down-) scattering should be observed in the near polar directions (i.e., the bimodal energy redistribution seen in the $\theta_v = 15°$ case), whereas in the equatorial directions (see the $\theta_v = 90°$ case; there is little energy redistribution) scattering should be relatively suppressed, which can account for the substantial differences among spectra viewed by the observer in different direction.

In Figure 5.6, we compare the reprocessed spectra with the injected fireball spectrum given by Equation (5.9) with an effective temperature of $T_{\mathrm{eff}} = 10$ keV. Evidently, the injected fireball spectrum is Compton upscattered by a factor of ~ 2 at $\epsilon \gtrsim 30$ keV. Moreover, the lower energy spectrum also exhibits a noticeable change; the initially flat spectrum becomes somewhat steeper due to the downscattering. Despite the clear angular dependence of the scattering seen in the case of monoenergetic spectrum shown in Figure 5.4, there is little difference among the reprocessed broadband spectra of the aligned rotator viewed in different angles, which clearly indicates
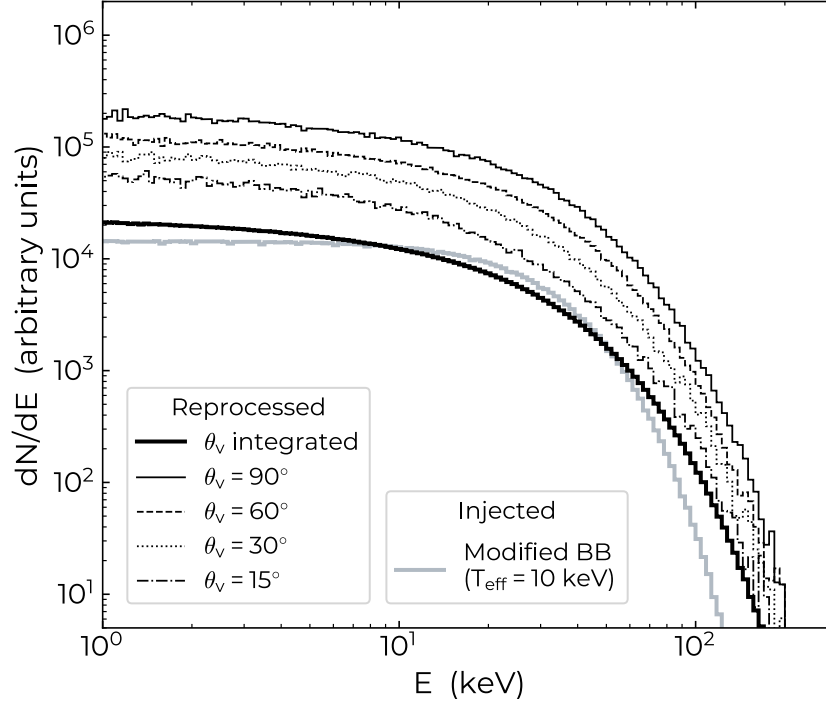
Figure 5.6: Spectral photon flux of RICS that might be sampled during magnetar flares. Thin black histograms are scaled for purpose of demonstration. The seed photon spectrum (the modified blackbody spectrum proposed by Lyubarsky 2002) with an effective temperature of $T_{\mathrm{eff}} = 10$ keV is also shown by the thick gray solid histogram.

that our model is almost isotropic. This is presumably due to the dominance of mildly-relativistic scattering particles as shown in Figure 5.5; the Doppler boost of the particle is insignificant. The almost isotropic character of our model also suggests that any degree of misalignment between the magnetic moment and the spin axis (i.e., temporal changes in the effective viewing angle) would not markedly produce the modulation in reprocessed spectra. Accordingly, we adopt the θ_v-integrated spectrum of the aligned rotator as a fiducial model. Thus we can almost accurately characterize the model with only one free parameter; T_{eff} and the flux normalization.

5.5   Discussion and Conclusion

Table 5.2:: SGR 1900+14 Burst Properties on March 29, 2006

Burst	Time (UT)	Duration (s)	Luminosity[a] (erg s^{-1})	Energy[a] (erg)
1	02:53:13.3	1.2	1.5×10^{41}	1.8×10^{41}
2	02:53:15.4	1.2	1.0×10^{41}	1.2×10^{41}

[a] Assuming a distance to the source of 10 kpc as done in Israel et al. (2008).

In order to verify our spectral model with observations, we analyzed intermediate flares from the representative magnetar SGR 1900+14 (Israel et al. 2008) with the surface dipole field strength $B_p \sim 7.0 \times 10^{14}$ G (Kaspi & Beloborodov 2017), which occurred on 2006 March 29[1], using the data of *Swift* Burst Alert Telescope (BAT; Krimm et al. 2013). Following the same methodology as presented in Israel et al. (2008), we carry out spectroscopy in the 15–100 keV range[2]. Specifically, we extract time-integrated spectra of two successive high-luminosity intermediate bursts (Burst 1 and Burst 2 hereafter; see Table 5.2), occurring at 4–5.2 s and 6.1–7.3 s (separated in time by 2.1 s, which is in fact within the stellar spin period of $P \sim 5.2$ s) in the top panel of Figure 1 in Israel et al. (2008), respectively. They are both classified into intermediate bursts in terms of duration and luminosity, albeit close to the lower end of the criteria. This may guarantee the self-consistent particle velocity distribution (eq. [5.5]) maintained by the strong radiation force of the flare, making them ideal targets.

Since our model implementation is purely numerical, a formal fit to the data requires the interpolation among a dense grid of pre-calculated spectral templates, which is computationally expensive. Instead of this, we simply overplot the model to the observed spectra in a qualitative fashion. We generate model templates that are calculated for a single dimension array within the range where the model parameter $T_{\rm eff}$ is defined (e.g., $T_{\rm eff} = [1, 2, \cdots, 99, 100]$ keV). In our model, the reprocessed spectrum parallelly shifts to higher energies with its entire shape nearly unchanged

---

[1]We extract flares during the third trigger (Sequence 00203109000) on 2006 Mar 29 from UT 01:27:53 to 01:28:36 with a total exposure of 43 s. See Israel et al. (2008) for more details.

[2]Since the cross section of photoelectric absorption drops exponentially at hard X-ray energies, the BAT spectra are not affected by the interstellar (neutral hydrogen) absorption; they can be regarded as intrinsic burst spectra.

as T_{eff} increases. Therefore, by sliding the spectral template parallelly to energy (varying T_{eff}) and flux (varing normalization), one can almost uniquely find a good-fit value of T_{eff} "by eye" that can reproduce the observed spectrum.

In Figure 5.7, we compare our model with the observed burst spectra. As one can clearly see, our model is in surprisingly good agreement with observations. We obtain good-fit effective temperatures $T_{\mathrm{eff}} = 7$ keV and 6 keV for the observed spectra of Burst 1 and Burst 2, respectively. There is no characteristic differences between two bursts in terms of their spectra and light curve. The effective temperature of the trapped fireball allows us to estimate the spherical radius of the fireball r_{FB} via $L = 4\pi r_{\mathrm{FB}}^2 \sigma_{\mathrm{SB}} T_{\mathrm{eff}}^4$, where $\sigma_{\mathrm{SB}} = \pi^2/(60\hbar^3 c^2)$ is the Stefan-Boltzmann constant and the emission is assumed to be isotropic. Adopting typical burst properties, this is re-written as $r_{\mathrm{FB}}/R_{\mathrm{NS}} \sim 2.5\,(L/10^{41}\ \mathrm{erg\ s^{-1}})^{1/2}(T_{\mathrm{eff}}/6\mathrm{keV})^{-2}$ (see also Olive et al. 2004 for a similar discussion), which is comparable to the stellar radius. Meanwhile, a typical height of resonant layer r_{res} for the thermal emission with $T_{\mathrm{eff}} = 6$–7 keV is estimated by Equations (5.2), (5.3) and (5.5) as $r_{\mathrm{res}}/R_{\mathrm{NS}} \sim 10\,\gamma_e$. Accordingly, we can ensure that the point-like assumption of fireball is valid ($r_{\mathrm{FB}} \gg r_{\mathrm{res}}$) for these bursts.

As demonstrated in the above, the observed hard X-ray spectra at 15–100 keV are successfully reproduced by the RICS model. Then how about the soft-band X-ray spectra? Since our model predicts that the downscattering effect slightly steepens the initially flat spectrum at low energy ranges, it is also interesting to compare this with observations. Olive et al. (2004) observed a set of intermediate flares (with average luminosity $L = 6.0 \times 10^{40}\ \mathrm{erg\ s^{-1}}$) from SGR 1900+14 that occurred on 2001 July 2, using the data of the FREGATE (French Gamma-Ray Telescope) and WXM (Wide-Field X-Ray Monitor) experiments aboard the HETE (High-Energy Transient Explorer) spacecraft. They obtained a broadband spectrum over 2–150 keV, extending down to soft X-ray energies (see Figure 5.1). We confirm that our model appears in good agreement with their broadband spectral behaviour including the softer part. The implication of the consistency between our model and observations is that a single scattering is sufficient to account for the hard component of observed spectra, and thereby suggesting that the optical depth to the resonant scattering might be $\tau_{\mathrm{res}} \sim \mathcal{O}(1)$ in the flaring magnetosphere.

Since the majority of magnetar flares have more or less thermal spectra, two blackbody model are known to provide successful fits. This may be interpreted as a thermalized emission from E-mode and O-mode photospheres (e.g., Israel et al. 2008; Kumar et al. 2010; Younes et al. 2014), while it is not clear whether the observed difference in temperature and size between the two photospheres can be realized (van Putten et al. 2016). In contrast, a seed photon spectrum adopted in this work (mod-

ified BB) takes into account the energy transfer under presence of strong magnetic field and two photon polarization modes (as noted in Section 5.9). Moreover, our model is a single-component, physically meaningful model; this is an advantage over the phenomenological multi-component models. Despite the good agreement with theoretical predictions, we believe that it is essential to study more bursts from different sources, to definitely validate our interpretation of the data. Furthermore, the two blackbody model can be tested by our RICS formalism, although this is beyond the scope of this work. As our model can directly extract the information of the fireball, this could be an ideal follow-up study, leading to a desired tool to investigate magnetar bursts.
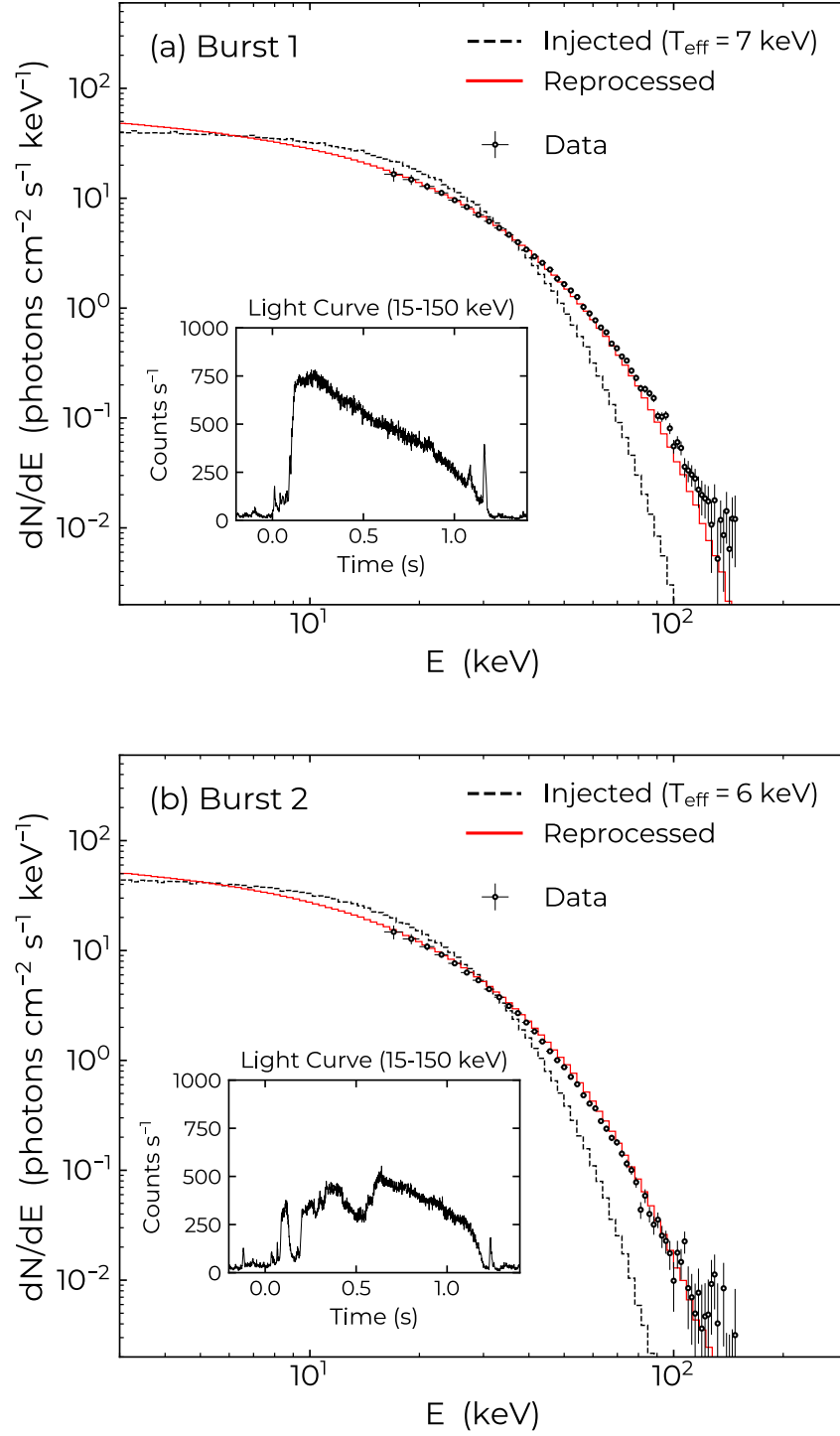
Figure 5.7: Hard X-ray spectra of the intermediate flares from SGR 1900+14 observed on 2006 March 29 by the *Swift*-BAT telescope (Top: Burst 1, Bottom: Burst 2). The data are overplotted by the best-fit reprocessed model spectra. The original spectra (the modified blackbody spectrum proposed by Lyubarsky 2002) are also shown.

Chapter 6

Conclusions

In this thesis we have carried out theoretical attempts to reveal the mysterious origins of FRBs and magnetars. These include theoretical arguments on the origin of FRBs and the modeling of the Galactic baryon distribution in mind of application to FRBs which we discussed in Chapter 2 and 3, respectively. Regarding the magnetar flares, we have answered two basic questions that are closely tied to the origin of flares: "*What is the relationship between magnetar flares and radio emissions?*" (Chapter 4) and "*What shapes the magnetar flare spectra inside the magnetosphere?*" (Chapter 5). Below we summarize the main findings and contributions of this thesis.

- **Origin of FRBs:** Most of FRBs do not show evidence for repetition, and such non-repeating FRBs may be produced at the time of a merger of binary neutron stars (BNS), provided that the BNS merger rate is close to the high end of the currently possible range. However, the merger environment is polluted by dynamical ejecta, which may prohibit the radio signal to propagate. We examine this by using a general-relativistic simulation of a BNS merger, and show that the ejecta appears about 1 ms after the rotation speed of the merged star becomes the maximum. Hence, there is a time window in which an FRB signal can reach outside, and the short duration of non-repeating FRBs can be explained by screening after ejecta formation. A fraction of BNS mergers may leave a rapidly rotating and stable neutron star, and such objects may be the origin of repeating source like FRB 121102. We show that a merger remnant would appear as a repeating FRB in a time scale of ∼1–10 yrs, and expected properties are consistent with the observations of FRB 121102. We construct an FRB rate evolution model including these two populations of repeating and non-repeating FRBs from BNS mergers, and show that the detection rate of repeating FRBs relative to non-repeating ones rapidly increases with improving

search sensitivity. This may explain why the only repeating source at that time (FRB 121102) was discovered by the most sensitive survey by the Arecibo Radio Telescope. Several unique predictions are made, including appearance of the repeating FRB 1–10 years after a BNS merger that is localized by gravitational wave and subsequent electromagnetic radiation.

- **Galactic halo DM model for FRBs:** A new model of the MW halo component of the DM for FRBs, is presented in light of recent diffuse X-ray observations. In addition to the spherical component of isothermal gas ($kT \sim 0.3$ keV) in hydrostatic equilibrium with the Galactic gravitational potential, our model includes a disk-like non-spherical hot gas component to reproduce the directional dependence of the observed X-ray emission measure (EM). The total gas mass ($1.2 \times 10^{11}\ M_\odot$) is dominated by the spherical component, and is consistent with the total baryon mass of the MW expected from the dark matter mass and the cosmic baryon-to-dark-matter ratio. Our model predicts a mean halo DM of 43 pc cm^{-3}, with a full range of 30–245 pc cm^{-3} over the whole sky. The large scatter seen in the X-ray EM data implies a ~ 0.2 dex (rms) fluctuation of the MW halo DM. We provide an analytic formula to estimate the MW halo DM of our model along any line of sight, which can be easily used to compute the total MW component of DM toward extragalactic sources, in combination with existing DM models of the warm ionized medium associated with the Galactic disk. Since our model predicts relatively large DM values over the whole sky (30–245 pc cm^{-3}), this strong DM signal would be imprinted onto the observed DM of FRBs. We plan to further investigate this by using nearby FRBs with a small observed DM ($\lesssim 100$ pc cm^{-3}), and there is a good prospect that a sample of such FRBs will increase with CHIME and other wide-field FRB surveys. Based on the above method, our hot gas halo model will be refined and upgraded with a new sample of FRBs, which would provide us an important benchmark for understanding the missing galactic baryon problem.

- **Connection between magnetar flares and radio pulsations:** There is growing evidence that a clear distinction between magnetars and radio pulsars may not exist, implying that the population of neutron stars that exhibit both radio pulsations and bursting activities could be potentially large. In this situation, new insights into the burst mechanism could be gained by combining the temporal behavior of radio pulsations. We present a general model for radio suppression by relativistic $e^\pm$ plasma outflows at the onset of magnetar flares. A sudden ejection of magnetic energy into the magnetosphere would generate a fireball plasma, which is promptly driven to expand at relativistic speed. This would make the plasma cutoff frequency significantly higher than

the rest frame radio frequency, resulting in the suppression of radio waves. We analytically show that any GHz radio emission arising from the magnetosphere is suppressed for ~ 100 s, depending on the total fireball energy. On the other hand, thermal radiation is expected from the hot spot(s) on the stellar surface created by an inflow of dense plasma, which could be the origin of short bursts. Since our hypothesis predicts radio suppression in coincidence with short bursts, this could be an indirect method to constrain the occurrence rate of short bursts at the faint end that cannot be detected by X-ray detectors. Furthermore, ultra-fast gamma-ray flashes from the fireball photosphere is also expected as a smoking gun, although the onboard detection is challenging due to its extremely short duration $\sim \mu$s. Finally, our model is applied to the radio pulsar with magnetar-like activities, PSR J1119–6127 in light of recent observations. Our model has an implication for FRBs, which might be related to magnetar flares. For instance, the position of FRB generation is severely constrained to $\gtrsim 10^{10}$ cm from the magnetar. Finally, since the plasma frequency would decrease with time, the timescale for the radio suppression would be shorter for higher frequencies. Namely, an unambiguous test of our model would be provided by future simultaneous observations of radio-emitting neutron stars at X-ray and at *multiple* radio bands during a period of magnetar flares.

- **Spectral formation of magnetar flares:** Although the trapped fireball model can successfully explain the temporal behavior of energetic flares, there has been a longstanding discrepancy between theoretical and observational flare spectra. In this work, we attempt to resolve this problem by considering the reprocess of the original fireball spectrum by the resonant inverse Compton scatterings. During the flare, photons emitted from the fireball should resonantly interact with the magnetospheric particles. We show by a simple thought experiment that such scattering particles are expected to move at mildly relativistic speed along closed magnetic field lines, which would slightly shift the incident photon energy due to the Doppler effect. Based on this idea, we develop a toy model for the scattering process during the flare and performing three-dimensional Monte Carlo simulation, taking into account both the angular velocity distribution of particles that is unique to flaring magnetospheres, and the realistic seed photon spectrum from the trapped fireball. We find that our spectral model can be effectively described by a single parameter; the effective temperature of the fireball, which greatly reduces the complications and allows us to fit the observed spectra with low computational cost. Our model is applied to the Swift/BAT data of energetic magnetar flares from SGR 1900+14, which gives a surprisingly good fit with fireball. The implication is that a single

scattering is sufficient to account for the hard component of observed spectra, and thereby suggesting that the optical depth to the resonant scattering might be $\sim \mathcal{O}(1)$ in the flaring magnetosphere. As our model can extract the information of the fireball, this could be an ideal follow-up study, leading to a desired tool to investigate magnetar bursts.

References

Abadie, J., Abbott, B. P., Abbott, R., et al. 2010, Classical and Quantum Gravity, 27, 173001

Abbott, B. P., Abbott, R., Abbott, T. D., et al. 2016, ApJ, 832, L21

—. 2017, Phys. Rev. Lett., 119, 161101

Anderson, M. E., & Bregman, J. N. 2010, ApJ, 714, 320

Arcavi, I., Wolf, W. M., Howell, D. A., et al. 2016, ApJ, 819, 35

Archibald, R. F., Kaspi, V. M., Tendulkar, S. P., & Scholz, P. 2016, ApJ, 829, L21

Archibald, R. F., Burgay, M., Lyutikov, M., et al. 2017, ApJ, 849, L20

Bannister, K. W., Deller, A. T., Phillips, C., et al. 2019, Science, 365, 565

Baring, M. G., & Harding, A. K. 2007, Ap&SS, 308, 109

Barthelmy, S. D., Barbier, L. M., Cummings, J. R., et al. 2005, Space Sci. Rev., 120, 143

Bassa, C. G., Beswick, R., Tingay, S. J., et al. 2016, MNRAS, 463, L36

Bassa, C. G., Tendulkar, S. P., Adams, E. A. K., et al. 2017, ApJ, 843, L8

Belczynski, K., Perna, R., Bulik, T., et al. 2006, ApJ, 648, 1110

Beloborodov, A. M. 2009, Astrophys. J., 703, 1044

Beloborodov, A. M. 2013, ApJ, 777, 114

—. 2017, ApJ, 843, L26

Beloborodov, A. M., & Thompson, C. 2007, ApJ, 657, 967

Bhandari, S., Keane, E. F., Barr, E. D., et al. 2018, MNRAS, 475, 1427

Bildsten, L., & Cutler, C. 1992, ApJ, 400, 175

Bregman, J. N. 2007, ARA&A, 45, 221

Bregman, J. N., & Lloyd-Davies, E. J. 2007, ApJ, 669, 990

Bullock, J. S., Kolatt, T. S., Sigad, Y., et al. 2001, MNRAS, 321, 559

Burgay, M., Possenti, A., Kerr, M., et al. 2016, The Astronomer's Telegram, 9366

Caleb, M., Keane, E. F., van Straten, W., et al. 2018, MNRAS, 478, 2046

Cameron, P. B., Chandra, P., Ray, A., et al. 2005, Nature, 434, 1112

Camilo, F., Kaspi, V. M., Lyne, A. G., et al. 2000, ApJ, 541, 367

Camilo, F., Ransom, S., Halpern, J., et al. 2006, Nature, 442, 892

Camilo, F., Ransom, S. M., Halpern, J. P., & Reynolds, J. 2007a, ApJ, 666, L93

Camilo, F., Cognard, I., Ransom, S. M., et al. 2007b, ApJ, 663, 497

Camilo, F., Ransom, S. M., Halpern, J. P., et al. 2016, Astrophys. J., 820, 110

Canuto, V., Lodenquai, J., & Ruderman, M. 1971, Phys. Rev. D, 3, 2303

Canuto, V., & Ventura, J. 1977, Fund. Cosmic Phys., 2, 203

Cen, R., & Ostriker, J. P. 1999, ApJ, 514, 1

—. 2006, ApJ, 650, 560

Champion, D. J., Petroff, E., Kramer, M., et al. 2016, MNRAS, 460, L30

Chatterjee, S., Law, C. J., Wharton, R. S., et al. 2017, Nature, 541, 58

Cheng, B., Epstein, R. I., Guyer, R. A., & Young, A. C. 1996, Nature, 382, 518

CHIME/FRB Collaboration, Amiri, M., Bandura, K., et al. 2018, ApJ, 863, 48

CHIME/FRB Collaboration, Andersen, B. C., Bandura, K., et al. 2019, ApJ, 885, L24

Collins, J. A., Shull, J. M., & Giroux, M. L. 2004, ApJ, 605, 216

Connor, L., Sievers, J., & Pen, U.-L. 2016, MNRAS, 458, L19

Cordes, J. M., & Chatterjee, S. 2019, ARA&A, 57, 417

Cordes, J. M., & Lazio, T. J. W. 2002, arXiv:astro-ph/0207156

—. 2003, arXiv:astro-ph/0301598

Cordes, J. M., & Wasserman, I. 2016, MNRAS, 457, 232

Cordes, J. M., Wasserman, I., Hessels, J. W. T., et al. 2017, Astrophys. J., 842, 35

Dai, Z. G., Wang, J. S., Wu, X. F., & Huang, Y. F. 2016, ApJ, 829, 27

Dai, Z. G., Wang, J. S., & Yu, Y. W. 2017, ApJ, 838, L7

Deng, W., & Zhang, B. 2014, ApJ, 783, L35

Dolag, K., Gaensler, B. M., Beck, A. M., & Beck, M. C. 2015, MNRAS, 451, 4277

Drout, M. R., Chornock, R., Soderberg, A. M., et al. 2014, ApJ, 794, 23

Duncan, R. C., & Thompson, C. 1992, ApJ, 392, L9

Enoto, T., Kisaka, S., & Shibata, S. 2019, Rept. Prog. Phys., 82, 106901

Enoto, T., Nakagawa, Y. E., Sakamoto, T., & Makishima, K. 2012, MNRAS, 427, 2824

Faerman, Y., Sternberg, A., & McKee, C. F. 2017, ApJ, 835, 52

Falcke, H., & Rezzolla, L. 2014, A&A, 562, A137

Fang, T., Bullock, J., & Boylan-Kolchin, M. 2013, ApJ, 762, 20

Fang, T., Buote, D., Bullock, J., & Ma, R. 2015, ApJS, 217, 21

Fang, T., Marshall, H. L., Lee, J. C., Davis, D. S., & Canizares, C. R. 2002, ApJ, 572, L127

Fang, T., Sembach, K. R., & Canizares, C. R. 2003, ApJ, 586, L49

Fernández, R., & Thompson, C. 2007, ApJ, 660, 615

Feroci, M., Hurley, K., Duncan, R. C., & Thompson, C. 2001, ApJ, 549, 1021

Fielding, D., Quataert, E., McCourt, M., & Thompson, T. A. 2017, Mon. Not. Roy. Astron. Soc., 466, 3810

Foreman-Mackey, D., Hogg, D. W., Lang, D., & Goodman, J. 2013, PASP, 125, 306

Fox, A. J., Wakker, B. P., Savage, B. D., et al. 2005, ApJ, 630, 332

Frail, D. A., Kulkarni, S. R., & Bloom, J. S. 1999, Nature, 398, 127

Fukugita, M., Hogan, C. J., & Peebles, P. J. E. 1998, ApJ, 503, 518

Fukugita, M., & Peebles, P. J. E. 2004, ApJ, 616, 643

Gaensler, B. M., Madsen, G. J., Chatterjee, S., & Mao, S. A. 2008, PASA, 25, 184

Gaensler, B. M., et al. 2005, Nature, 434, 1104

Gao, H., Zhang, B., Wu, X.-F., & Dai, Z.-G. 2013, Phys. Rev. D, 88, 043010

Gavriil, F. P., Gonzalez, M. E., Gotthelf, E. V., et al. 2008, Science, 319, 1802

Gelfand, J. D., Lyubarsky, Y. E., Eichler, D., et al. 2005, ApJ, 634, L89

Geng, J. J., & Huang, Y. F. 2015, ApJ, 809, 24

Ghisellini, G., & Svensson, R. 1991, MNRAS, 252, 313

Gibson, B. K., Giroux, M. L., Penton, S. V., et al. 2000, AJ, 120, 1830

Gill, R., & Heyl, J. S. 2010, MNRAS, 407, 1926

Glendenning, N. K., & Moszkowski, S. A. 1991, Physical Review Letters, 67, 2414

Gonthier, P. L., Harding, A. K., Baring, M. G., Costello, R. M., & Mercer, C. L. 2000, ApJ, 540, 907

Goodman, J. 1986, ApJ, 308, L47

Götz, D., Mereghetti, S., Tiengo, A., & Esposito, P. 2006, A&A, 449, L31

Göğüş, E., Lin, L., Kaneko, Y., et al. 2016, ApJ, 829, L25

Göğüş , E., Woods, P. M., Kouveliotou, C., et al. 1999, ApJ, 526, L93

Göğüş, E., Woods, P. M., Kouveliotou, C., et al. 2000, ApJ, 532, L121

Göğüş, E., Kouveliotou, C., Woods, P. M., et al. 2001, ApJ, 558, 228

Göğüş, E., Woods, P. M., Kouveliotou, C., et al. 2011, ApJ, 740, 55

Granot, J., Ramirez-Ruiz, E., Taylor, G. B., et al. 2006, ApJ, 638, 391

Grimsrud, O. M., & Wasserman, I. 1998, MNRAS, 300, 1158

Gupta, A., Mathur, S., Krongold, Y., Nicastro, F., & Galeazzi, M. 2012, ApJ, 756, L8

Hagihara, T., Yao, Y., Yamasaki, N. Y., et al. 2010, PASJ, 62, 723

Hansen, B. M. S., & Lyutikov, M. 2001, MNRAS, 322, 695

Harding, A. K., & Lai, D. 2006, Reports on Progress in Physics, 69, 2631

Henley, D. B., & Shelton, R. L. 2013, ApJ, 773, 92

Hessels, J. W. T., Spitler, L. G., Seymour, A. D., et al. 2019, ApJ, 876, L23

Horesh, A., Hotokezaka, K., Piran, T., Nakar, E., & Hancock, P. 2016, ApJ, 819, L22

Hotokezaka, K., Kyutoku, K., Tanaka, M., et al. 2013, ApJ, 778, L16

Huang, L., & Yu, C. 2014a, ApJ, 784, 168

—. 2014b, ApJ, 796, 3

Hurley, K., Cline, T., Mazets, E., et al. 1999, Nature, 397, 41

Hurley, K., Boggs, S. E., Smith, D. M., et al. 2005, Nature, 434, 1098

Inoue, S. 2004, MNRAS, 348, 999

Ioka, K. 2003, ApJ, 598, L79

Israel, G. L., Romano, P., Mangano, V., et al. 2008, ApJ, 685, 1114

Iwamoto, S., & Takahara, F. 2002, ApJ, 565, 163

Johnston, S., Taylor, R., Bailes, M., et al. 2008, Experimental Astronomy, 22, 151

Kashiyama, K., Ioka, K., & Mészáros, P. 2013, ApJ, 776, L39

Kashiyama, K., & Murase, K. 2017, ApJ, 839, L3

Kaspi, V. M., & Beloborodov, A. M. 2017, ARA&A, 55, 261

Kaspi, V. M., & McLaughlin, M. A. 2005, ApJ, 618, L41

Kaspi, V. M., Archibald, R. F., Bhalerao, V., et al. 2014, ApJ, 786, 84

Katz, J. I. 2014, Phys. Rev. D, 89, 103009

—. 2016, Modern Physics Letters A, 31, 1630013

Keane, E., Bhattacharyya, B., Kramer, M., et al. 2015, Advancing Astrophysics with the Square Kilometre Array (AASKA14), 40

Keane, E. F. 2018, Nature Astronomy, 2, 865

Keane, E. F., & Petroff, E. 2015, MNRAS, 447, 2852

Keane, E. F., Johnston, S., Bhandari, S., et al. 2016, Nature, 530, 453

Kennea, J. A., Lien, A. Y., Marshall, F. E., et al. 2016, GRB Coordinates Network, Circular Service, No. 19735, #1 (2016), 19735

Kennel, C. F., & Coroniti, F. V. 1984, ApJ, 283, 710

Kerr, F. J., & Lynden-Bell, D. 1986, MNRAS, 221, 1023

Kisaka, S., Asano, K., & Terasawa, T. 2016, ApJ, 829, 12

Kiuchi, K., Kyutoku, K., Sekiguchi, Y., Shibata, M., & Wada, T. 2014, Phys. Rev. D, 90, 041502

Klypin, A., Zhao, H., & Somerville, R. S. 2002, ApJ, 573, 597

Kokubo, M., Mitsuda, K., Sugai, H., et al. 2017, ApJ, 844, 95

Kouveliotou, C., Dieters, S., Strohmayer, T., et al. 1998, Nature, 393, 235

Kouveliotou, C., Strohmayer, T., Hurley, K., et al. 1999, Astrophys. J., 510, L115

Kozlova, A. V., Israel, G. L., Svinkin, D. S., et al. 2016, MNRAS, 460, 2008

Krimm, H. A., Holland, S. T., Corbet, R. H. D., et al. 2013, ApJS, 209, 14

Kulkarni, S. R. 2018, Nature Astronomy, 2, 832

Kulkarni, S. R., Ofek, E. O., & Neill, J. D. 2015, ArXiv e-prints, arXiv:1511.09137

Kulkarni, S. R., Ofek, E. O., Neill, J. D., Zheng, Z., & Juric, M. 2014, ApJ, 797, 70

Kumar, H. S., Ibrahim, A. I., & Safi-Harb, S. 2010, ApJ, 716, 97

Kumar, P., Lu, W., & Bhattacharya, M. 2017, MNRAS, 468, 2726

Kumar, P., Shannon, R. M., Osłowski, S., et al. 2019, ApJ, 887, L30

Lai, D. 2012, ApJ, 757, L3

Lattimer, J. M., & Prakash, M. 2007, Phys. Rep., 442, 109

Levin, L., Bailes, M., Bates, S., et al. 2010, ApJ, 721, L33

Li, C., & Sari, R. 2008, ApJ, 677, 425

Li, Y., & Bregman, J. 2017, ApJ, 849, 105

Li, Z., Gao, H., Wei, J.-J., et al. 2019, ApJ, 876, 146

Liu, T., Romero, G. E., Liu, M.-L., & Li, A. 2016, ApJ, 826, 82

Lorimer, D. R., Bailes, M., McLaughlin, M. A., Narkevic, D. J., & Crawford, F. 2007, Science, 318, 777

Lyubarsky, Y. 2009, ApJ, 696, 320

—. 2014, MNRAS, 442, L9

Lyubarsky, Y. E. 2002, MNRAS, 332, 199

Lyutikov, M. 2003, MNRAS, 346, 540

—. 2006, MNRAS, 367, 1594

Lyutikov, M., & Gavriil, F. P. 2006, MNRAS, 368, 690

Madau, P., & Dickinson, M. 2014, ARA&A, 52, 415

Mahony, E. K., Ekers, R. D., Macquart, J.-P., et al. 2018, ApJ, 867, L10

Main, R., Yang, I.-S., Chan, V., et al. 2018, Nature, 557, 522

Majid, W. A., Pearlman, A. B., Dobreva, T., et al. 2017, ApJ, 834, L2

Maller, A. H., & Bullock, J. S. 2004, MNRAS, 355, 694

Manchester, R. N., Fan, G., Lyne, A. G., Kaspi, V. M., & Crawford, F. 2006, ApJ, 649, 235

Manchester, R. N., Hobbs, G. B., Teoh, A., & Hobbs, M. 2005, AJ, 129, 1993

Marcote, B., Paragi, Z., Hessels, J. W. T., et al. 2017, ApJ, 834, L8

Margalit, B., Berger, E., & Metzger, B. D. 2019, ApJ, 886, 110

Masada, Y., Nagataki, S., Shibata, K., & Terasawa, T. 2010, PASJ, 62, 1093

Masui, K., Lin, H.-H., Sievers, J., et al. 2015, Nature, 528, 523

Mathews, W. G., & Prochaska, J. X. 2017, ApJ, 846, L24

Mazets, E. P., Cline, T. L., Aptekar', R. L., et al. 1999, Astronomy Letters, 25, 628

Mazets, E. P., Golentskii, S. V., Ilinskii, V. N., Aptekar, R. L., & Guryan, I. A. 1979, Nature, 282, 587

McCammon, D., Almy, R., Apodaca, E., et al. 2002, ApJ, 576, 188

McConnell, D., McCulloch, P. M., Hamilton, P. A., et al. 1991, MNRAS, 249, 654

McKernan, B., Yaqoob, T., & Reynolds, C. S. 2004, Astrophys. J., 617, 232

McQuinn, M. 2014, ApJ, 780, L33

Meegan, C., Lichti, G., Bhat, P. N., et al. 2009, ApJ, 702, 791

Mereghetti, S., Götz, D., Weidenspointner, G., et al. 2009, ApJ, 696, L74

Meszaros, P. 1992, High-energy radiation from magnetized neutron stars

Metzger, B. D., Berger, E., & Margalit, B. 2017, ApJ, 841, 14

Metzger, B. D., Margalit, B., & Sironi, L. 2019, MNRAS, 485, 4091

Metzger, B. D., & Piro, A. L. 2014, MNRAS, 439, 3916

Michilli, D., Seymour, A., Hessels, J. W. T., et al. 2018, Nature, 553, 182

Mihalas, D., & Mihalas, B. W. 1984, Foundations of radiation hydrodynamics

Miller, M. J., & Bregman, J. N. 2013, ApJ, 770, 118

—. 2015, ApJ, 800, 14

Mingarelli, C. M. F., Levin, J., & Lazio, T. J. W. 2015, ApJ, 814, L20

Murase, K., Kashiyama, K., Kiuchi, K., & Bartos, I. 2015, ApJ, 805, 82

Murase, K., Kashiyama, K., & Mészáros, P. 2016, MNRAS, 461, 1498

Nakagawa, Y., Ebisawa, K., & Enoto, T. 2018, PASJ, 70, 32

Nakagawa, Y. E., Yoshida, A., Yamaoka, K., & Shibazaki, N. 2009, PASJ, 61, 109

Nakagawa, Y. E., Yoshida, A., Hurley, K., et al. 2007, PASJ, 59, 653

Nakar, E., Piran, T., & Sari, R. 2005, ApJ, 635, 516

Nakashima, S., Inoue, Y., Yamasaki, N., et al. 2018, ApJ, 862, 34

Navarro, J. F., Frenk, C. S., & White, S. D. M. 1997, ApJ, 490, 493

Nicastro, F., Zezas, A., Drake, J., et al. 2002, ApJ, 573, 157

Nicholl, M., Williams, P. K. G., Berger, E., et al. 2017, ApJ, 843, 84

Nobili, L., Turolla, R., & Zane, S. 2008, MNRAS, 386, 1527

Nuza, S. E., Parisi, F., Scannapieco, C., et al. 2014, MNRAS, 441, 2593

Ofek, E. O. 2017, ApJ, 846, 44

Olausen, S. A., & Kaspi, V. M. 2014, ApJS, 212, 6

Olive, J. F., Hurley, K., Sakamoto, T., et al. 2004, ApJ, 616, 1148

Omand, C. M. B., Kashiyama, K., & Murase, K. 2018, MNRAS, 474, 573

Paczynski, B. 1986, ApJ, 308, L43

—. 1992, , 42, 145

Palmer, D. M., Barthelmy, S., Gehrels, N., et al. 2005, Nature, 434, 1107

Parfrey, K., Beloborodov, A. M., & Hui, L. 2013, ApJ, 774, 92

Pen, U.-L., & Connor, L. 2015, ApJ, 807, 179

Perley, D. A., Perley, R. A., Dhawan, V., & Carilli, C. L. 2017, ApJ, 841, 117

Petroff, E., van Straten, W., Johnston, S., et al. 2014, ApJ, 789, L26

Petroff, E., Johnston, S., Keane, E. F., et al. 2015, MNRAS, 454, 457

Petroff, E., Barr, E. D., Jameson, A., et al. 2016, PASA, 33, e045

Petroff, E., Burke-Spolaor, S., Keane, E. F., et al. 2017, MNRAS, 469, 4465

Petroff, E., Oostrum, L. C., Stappers, B. W., et al. 2019, MNRAS, 482, 3109

Pietrzyński, G., et al. 2013, Nature, 495, 76

Piro, A. L. 2012, ApJ, 755, 80

—. 2016, ApJ, 824, L32

Piro, A. L., Giacomazzo, B., & Perna, R. 2017, ApJ, 844, L19

Planck Collaboration, Ade, P. A. R., Aghanim, N., et al. 2016, A&A, 594, A13

Platts, E., Weltman, A., Walters, A., et al. 2018, arXiv e-prints, arXiv:1810.05836

Pol, N., Lam, M. T., McLaughlin, M. A., Lazio, T. J. W., & Cordes, J. M. 2019, ApJ, 886, 135

Popov, S. B., & Postnov, K. A. 2010a, in Evolution of Cosmic Objects through their Physical Activity, ed. H. A. Harutyunian, A. M. Mickaelian, & Y. Terzian, 129–132

Popov, S. B., & Postnov, K. A. 2010b, in Evolution of Cosmic Objects through their Physical Activity, ed. H. A. Harutyunian, A. M. Mickaelian, & Y. Terzian, 129–132

Popov, S. B., Postnov, K. A., & Pshirkov, M. S. 2018, Phys. Usp., 61, 965

Price, D. C., Foster, G., Geyer, M., et al. 2019, MNRAS, 486, 3636

Prochaska, J. X., & Neeleman, M. 2018, MNRAS, 474, 318

Prochaska, J. X., & Zheng, Y. 2019, MNRAS, 485, 648

Prochaska, J. X., Macquart, J.-P., McQuinn, M., et al. 2019, Science, 365, aay0073

Quimby, R. M., Yuan, F., Akerlof, C., & Wheeler, J. C. 2013, MNRAS, 431, 912

Rasmussen, A., Kahn, S. M., & Paerels, F. 2003, in Astrophysics and Space Science Library, Vol. 281, The IGM/Galaxy Connection. The Distribution of Baryons at z=0, ed. J. L. Rosenberg & M. E. Putman, 109

Ravi, V., Shannon, R. M., Bailes, M., et al. 2016, Science, 354, 1249

Ravi, V., Catha, M., D'Addario, L., et al. 2019, Nature, 572, 352

Rea, N., & Esposito, P. 2011, Astrophysics and Space Science Proceedings, 21, 247

Rea, N., Zane, S., Turolla, R., Lyutikov, M., & Götz, D. 2008, ApJ, 686, 1245

Rea, N., Esposito, P., Turolla, R., et al. 2010, Science, 330, 944

Rea, N., Israel, G. L., Esposito, P., et al. 2012, ApJ, 754, 27

Readhead, A. C. S. 1994, ApJ, 426, 51

Readhead, A. C. S., & Duffett-Smith, P. J. 1975, A&A, 42, 151

Reynolds, R. J. 1989, ApJ, 339, L29

Rickett, B. J. 1990, ARA&A, 28, 561

Roca-Fàbrega, S., Valenzuela, O., Colín, P., et al. 2016, ApJ, 824, 94

Rybicki, G. B., & Lightman, A. P. 1979, Radiative processes in astrophysics

Savage, B. D., & Wakker, B. P. 2009, ApJ, 702, 1472

Savchenko, V., Neronov, A., Beckmann, V., Produit, N., & Walter, R. 2010, A&A, 510, A77

Scholz, P., Spitler, L. G., Hessels, J. W. T., et al. 2016, ApJ, 833, 177

Sekiguchi, Y., Kiuchi, K., Kyotoku, K., & Shibata, M. 2015, Phys. Rev. D, 91, 064059

Sembach, K. R., Wakker, B. P., Savage, B. D., et al. 2003, ApJS, 146, 165

Shannon, R. M., Macquart, J.-P., Bannister, K. W., et al. 2018, Nature, 562, 386

Shcherbakov, R. V. 2008, ApJ, 688, 695

Shibata, M., Kiuchi, K., & Sekiguchi, Y.-i. 2017, Phys. Rev. D, 95, 083005

Shull, J. M., & Danforth, C. W. 2018, ApJ, 852, L11

Shull, J. M., Smith, B. D., & Danforth, C. W. 2012, ApJ, 759, 23

Snowden, S. L., Egger, R., Freyberg, M. J., et al. 1997, ApJ, 485, 125

Sommer-Larsen, J. 2006, ApJ, 644, L1

Spitler, L. G., Cordes, J. M., Hessels, J. W. T., et al. 2014, ApJ, 790, 101

Spitler, L. G., Scholz, P., Hessels, J. W. T., et al. 2016, Nature, 531, 202

Spitzer, Jr., L. 1956, ApJ, 124, 20

Svensson, R. 1982, ApJ, 258, 335

Szary, A., Melikidze, G. I., & Gil, J. 2015, ApJ, 800, 76

Tanaka, S. J., & Takahara, F. 2010, ApJ, 715, 1248

—. 2013, MNRAS, 429, 2945

Taylor, J. H., & Cordes, J. M. 1993, ApJ, 411, 674

Tendulkar, S. P., Bassa, C. G., Cordes, J. M., et al. 2017, ApJ, 834, L7

Tepper-García, T., Bland-Hawthorn, J., & Sutherland, R. S. 2015, ApJ, 813, 94

Thompson, C., & Blaes, O. 1998, Phys. Rev. D, 57, 3219

Thompson, C., & Duncan, R. C. 1995, MNRAS, 275, 255

—. 1996, ApJ, 473, 322

—. 2001, ApJ, 561, 980

Thompson, C., Lyutikov, M., & Kulkarni, S. R. 2002, ApJ, 574, 332

Thornton, D., Stappers, B., Bailes, M., et al. 2013, Science, 341, 53

Timokhin, A. N. 2010a, MNRAS, 408, L41

—. 2010b, MNRAS, 408, 2092

Timokhin, A. N., & Arons, J. 2013, MNRAS, 429, 20

Totani, T. 2013, PASJ, 65, L12

Totani, T., Morokuma, T., Oda, T., Doi, M., & Yasuda, N. 2008, PASJ, 60, 1327

Tumlinson, J., Thom, C., Werk, J. K., et al. 2011, Science, 334, 948

Ulmer, A. 1994, ApJ, 437, L111

Usov, V. V. 1992, Nature, 357, 472

van Leeuwen, J. 2014, in The Third Hot-wiring the Transient Universe Workshop, ed. P. R. Wozniak, M. J. Graham, A. A. Mahabal, & R. Seaman, 79–79

van Putten, T., Watts, A. L., Baring, M. G., & Wijers, R. A. M. J. 2016, MNRAS, 461, 877

Wadiasingh, Z., Baring, M. G., Gonthier, P. L., & Harding, A. K. 2018, ApJ, 854, 98

Wang, J.-S., Yang, Y.-P., Wu, X.-F., Dai, Z.-G., & Wang, F.-Y. 2016, ApJ, 822, L7

Wang, N., Manchester, R. N., & Johnston, S. 2007, MNRAS, 377, 1383

Wang, Q. D., Yao, Y., Tripp, T. M., et al. 2005, Astrophys. J., 635, 386

Watts, A. L., Kouveliotou, C., van der Horst, A. e. J., et al. 2010, ApJ, 719, 190

Williams, P. K. G., & Berger, E. 2016, ApJ, 821, L22

Woods, P. M., & Thompson, C. 2006, Soft gamma repeaters and anomalous X-ray pulsars: magnetar candidates, Vol. 39, 547–586

Yamamoto, T., Shibata, M., & Taniguchi, K. 2008, Phys. Rev. D, 78, 064054

Yamasaki, S., Kisaka, S., Terasawa, T., & Enoto, T. 2019, MNRAS, 483, 4175

Yamasaki, S., & Totani, T. 2020, ApJ, 888, 105

Yamasaki, S., Totani, T., & Kawanaka, N. 2016, MNRAS, 460, 2875

Yamasaki, S., Totani, T., & Kiuchi, K. 2018, PASJ, 70, 39

Yang, Y.-P., Zhang, B., & Dai, Z.-G. 2016, ApJ, 819, L12

Yao, G.-R., Huang, L., Yu, C., & Shen, Z.-Q. 2018, ApJ, 854, 10

Yao, J. M., Manchester, R. N., & Wang, N. 2017, ApJ, 835, 29

Yao, Y., & Wang, Q. D. 2007, ApJ, 658, 1088

Yao, Y., Wang, Q. D., Hagihara, T., et al. 2009, ApJ, 690, 143

Yoshino, T., Mitsuda, K., Yamasaki, N. Y., et al. 2009, PASJ, 61, 805

Younes, G., Kouveliotou, C., & Roberts, O. 2016, GRB Coordinates Network, Circular Service, No. 19736, #1 (2016), 19736

Younes, G., Kouveliotou, C., van der Horst, A. J., et al. 2014, ApJ, 785, 52

Yu, C. 2012, ApJ, 757, 67

Yu, C., & Huang, L. 2013, ApJ, 771, L46

Zane, S., Turolla, R., Nobili, L., & Rea, N. a. 2011, Advances in Space Research, 47, 1298

Zhang, B. 2017, ApJ, 836, L32

—. 2018, The Physics of Gamma-Ray Bursts, doi:10.1017/9781139226530

Appendix A

Synchrotron Absorption

Murase et al. (2016) have shown that synchrotron absorption by non-thermal electrons in the nebula becomes important as well as free-free absorption in the ejecta, based on the early studies on the Galactic pulsar wind nebulae (Kennel & Coroniti 1984; Tanaka & Takahara 2010, 2013). Here we detail how we dealt with the synchrotron absorption in deriving the timescale for nebula/ejecta around the BNS merger remnant to be transparent to the process.

A.1   Nebula Region

The evolution of the electron energy distribution $n_e(\gamma_e, t)$ in the nebula region is given by the continuity equation:

$$\frac{\partial}{\partial t} n_e(\gamma_e) + \frac{\partial}{\partial \gamma_e} \left[\dot{\gamma}_e n_e(\gamma_e) \right] = S(\gamma_e), \tag{A.1}$$

where $\dot{\gamma}_e$ is the cooling rate. We assume that the particle injection term $S(\gamma_e)$ has a broken power-law form

$$S(\gamma_e) \propto \begin{cases} \gamma_e^{-q_1} & (\gamma_{\mathrm{m}} \leq \gamma_e \leq \gamma_{\mathrm{b}}) \\ \gamma_e^{-q_2} & (\gamma_{\mathrm{b}} \leq \gamma_e \leq \gamma_{\mathrm{M}}), \end{cases} \tag{A.2}$$

where $q_1 = 1\text{--}1.5\,(< 2)$ and $q_2 = 2.5 - 3\,(> 2)$ are the lower- and higher-energy power-law indices, respectively. We set the break Lorentz factor as $\gamma_{\mathrm{b}} = 10^4\text{--}10^6$ based on the study on Galactic PWNe (Tanaka & Takahara 2010, 2013), and γ_{M} is determined by equating the acceleration timescale of a single electron $t_{\mathrm{acc}} = 2\pi \gamma_e m_e c/(e B_{\mathrm{ej}})$ with

the synchrotron cooling timescale $t_{\rm syn}$. Since the typical Lorentz factor of injected particles $\gamma_{\rm b}$ is similar to $\gamma_c = 10^4$–10^7 at times 1–10 yr, we assume $\gamma_c \sim \gamma_{\rm b}$ for simplicity. In addition, we consider a steady state and thus the first term with $\partial/\partial t$ in the left-hand side of the Equation (A.1) is neglected. For a slow cooling regime ($\gamma_m \ll \gamma_c$), which is the case for the BNS-merger-produced nebula, the form of the emergent spectrum for the particles is expressed as

$$n_e(\gamma_e) \propto \begin{cases} \gamma_e^{-q_1} & (\gamma_{\rm m} \le \gamma_e \le \gamma_{\rm c} \sim \gamma_{\rm b}) \\ \gamma_e^{-q_2-1} & (\gamma_{\rm c} \sim \gamma_{\rm b} \le \gamma_e \le \gamma_{\rm M}), \end{cases} \tag{A.3}$$

where we have used the relation $\dot\gamma_e \approx \gamma_e/t_{\rm syn} \propto \gamma_e^2$. We normalized the steady-state spectrum such that a fraction $\epsilon_e = 1 - \epsilon_B \approx 1$ of the total internal energy U is carried by relativistic electrons and positrons, since it is generally believed that the pulsar wind is dominated by $e^\pm$ (Kennel & Coroniti 1984; Tanaka & Takahara 2013):

$$m_e c^2 \int_{\gamma_m}^{\gamma_{\rm M}} \gamma_e n_e(\gamma_e) d\gamma_e = \epsilon_e U/(4\pi r_{\rm ej}^3/3). \tag{A.4}$$

Consider a radiation with frequency ν propagating through the nebula with physical size of $r_{\rm ej} = \beta_{\rm PWN} \, ct$. The optical depth to the synchrotron absorption (Rybicki & Lightman 1979; Ghisellini & Svensson 1991) is estimated by

$$\tau_\nu^{\rm sa} = \frac{r}{8\pi m_{\rm e} \, c \, \nu^2} \int_{\gamma_{\rm m}}^{\gamma_{\rm M}} \frac{1}{\gamma_e^2} \frac{d}{d\gamma_e} \left[\gamma_e^2 P_{\rm s}(\nu, \gamma_e) \right] n_e(\gamma_e) \, d\gamma_e \;, \tag{A.5}$$

where $P_{\rm s}(\nu, \gamma) = \sqrt{3} \, e^3 B_{\rm ej}/(m_{\rm e} \, c^2) F(\nu/\nu_{\rm ch})$ is the synchrotron emitting power of a single electron, $F(x) = x \int_x^\infty K_{\frac{5}{3}}(\xi) d\xi$ the synchrotron function and $\nu_{\rm ch} = (3/2)\gamma^2 \nu_{\rm B}$ the characteristic frequency with $\nu_{\rm B} = e B_{\rm ej}/(2\pi m_{\rm e} \, c)$ being the cyclotron frequency. We numerically computed the transparency timescale $t_{\rm tr}^{\rm sa}$, by solving $\tau_\nu^{\rm sa}\,(t_{\rm tr}^{\rm sa}) = 1$. In numerical calculation, we set $\gamma_{\rm m} = 100$ (the result is insensitive to this value as long as it is small enough as noted in Murase et al. 2015) and $\gamma_{\rm M}$ to be sufficiently large. As a result, we find that the nebula becomes transparent to 1 GHz radio emission at latest $t_{\rm tr}^{\rm sa} \sim 1.2$ yr for different sets of parameters ranging $q_1 = 1$–1.5, $q_2 = 2.5$–3 and $\gamma_{\rm b} = 10^4$–10^6.

A.2   Ejecta Region

The synchrtron absorption in the ejecta is also estimated here. We assume a single power-law as a typical injection electron/positron spectrum at the termination shock:

$$S(\gamma_e) \propto \gamma_e^{-p} \quad (\gamma_{\mathrm{m}} < \gamma_e < \gamma_{\mathrm{M}}), \tag{A.6}$$

where $\gamma_m = (\Gamma_{\mathrm{PWN}}/1.9)\,(A/56)\,m_{\mathrm{p}}/m_{\mathrm{e}} \sim 2.0 \times 10^5$ is the minimum Lorentz factor for shock-accelerated electrons with $\Gamma_{\mathrm{PWN}} = (1 - \beta_{\mathrm{PWN}}^2)^{-1/2}$ and A being the atomic number of the dominant element (i.e., iron) in the ejecta. Due to the large value of γ_m, electrons in the ejecta is in the fast cooling regime $\gamma_c \lesssim \gamma_m$ (this is the case at $t10$ yr), which is in contrast to the nebula region. The emergent spectrum for electrons is given by

$$n_e(\gamma_e) \propto \begin{cases} \gamma_e^{-2} & (\gamma_c \leq \gamma_e \leq \gamma_{\mathrm{m}}) \\ \gamma_e^{-p-1} & (\gamma_{\mathrm{m}} \leq \gamma_e \leq \gamma_{\mathrm{M}}). \end{cases} \tag{A.7}$$

The above spectrum can be normalized with a similar manner in the case of the nebula, but with a different value of $\epsilon_e \sim 0.01$. By numerically calculating Equation (A.5) for $p > 2$ and a sufficiently large value of γ_{M}, it is found that the effect of the ejecta contribution to the synchrotron absorption optical depth is negligible: $\tau_\nu^{\mathrm{sa}}(1 \text{ yr}) \sim 10^{-6} \ll 1$.

Appendix B

Fully-ionized Gas

At high temperatures ($T \gtrsim 10^6$ K), the hot gas can be treated as a fully-ionized gas composed of hydrogen and helium since the electron contributions from other heavier elements are negligible for the metallicity range of our interest ($Z = 0.1\text{--}1\,Z_\odot \sim 0.001\text{--}0.01$). Here we show the definition and derivation of a few important quantities that have been used to compute the gas particle number density.

B.1   Mean Particle Mass

The equation of state (EOS) of an ideal gas relates gas pressure P, gas temperature T and gas particle number density n as

$$P = nk_BT \ .$$
(B.1)

To relate n to the mass density ρ, we use

$$n = \frac{\rho}{\overline{m}} \ ,$$
(B.2)

where $\overline{m}$ denotes the mean mass per particle. For our purpose, it is useful to express the $\overline{m}$ in units of proton mass m_p (hydrogen atom mass). We thus define a quantity μ called *mean particle mass* as

$$\mu \equiv \frac{\overline{m}}{m_p} = \frac{\rho}{m_p n} \ ,$$
(B.3)

where we have used Equation (B.2). In order to evaluate μ for an arbitrary gas composed of different atomic species, one must average particle mass over all species.

Let n_j and m_j the number density and the mass of the atom with atomic number j, respectively. Then one finds

$$\overline{m} = \frac{\sum_j n_j m_j + n_e m_e}{\sum_j n_j + n_e} \approx \frac{\sum_j n_j m_j}{\sum_j n_j + n_e} = \frac{\sum_j n_j A_j}{\sum_j n_j + n_e} m_p , \qquad (B.4)$$

where we have introduced the mass number A_j defined by $m_j \equiv A_j m_p$, and the mass of an electron m_e ($\ll m_j$) is neglected in the above approximation. The mean particle mass is therefore expressed as

$$\mu = \frac{\overline{m}}{m_p} = \frac{\sum_j n_j A_j}{\sum_j n_j + n_e} = \frac{\sum_j n_j A_j}{\sum_j n_j (1+j)}. \qquad (B.5)$$

The last equality holds when the gas being considered is fully ionized and thus the electron number density is given by $n_e = \sum_j j n_j$. In more general cases, n_e must be determined from the Saha's equation. Next, let us introduce the *mass fraction* X_j of each atomic element j by $X_j = m_j/m = \rho_j/\rho$ (i.e., $\sum_j X_j = 1$). Then the number density of atomic element j can be written as

$$n_j = \frac{\rho_j}{m_j} = \frac{\rho X_j}{m_p A_j}. \qquad (B.6)$$

Substituting Equation (B.6) into Equation (B.5) yields

$$\mu^{-1} = \sum_j \frac{X_j}{A_j}(1+j) \approx 2X_1 + \frac{3}{4}X_2 + \frac{1}{2}\sum_{j=3}^{\infty} X_j = 2X + \frac{3}{4}Y + \frac{1}{2}Z, \qquad (B.7)$$

where we have used $(1+j)/A_j \sim 1/2$ for heavy elements ($j \geq 3$). We define hydrogen mass fraction by $X \equiv X_1$ and helium mass fraction by $Y \equiv X_2$. The metal mass fraction Z is defined as a sum of mass fraction over all heavy elements $j \geq 3$. Therefore, our assumption of 30% helium mass fraction ($X = 0.7$, $Y = 0.3$, $Z = 0$) yields $\mu = 0.62$.

B.2 Mean Molecular Mass per Electron

The n_e and ρ can be related by the *mean molecular mass per electron* μ_e, defined by

$$\mu_e \equiv \frac{\rho}{m_p n_e}. \qquad (B.8)$$

According to the discussion in Section B.1, the electron number density in a fully-ionized gas reads

$$
\begin{aligned}
n_e &= \sum_j j n_j \\
&= \frac{\rho}{m_p} \sum_j \frac{X_j}{A_j} j \\
&= \frac{\rho}{m_p} \left(X_1 + \frac{1}{2} X_2 + \frac{1}{2} \sum_{j=3}^{\infty} X_j \right) \\
&= \frac{\rho}{m_p} \left(X + \frac{1}{2} Y + \frac{1}{2} Z \right) \\
&= \frac{\rho}{2 m_p} \left(1 + X \right).
\end{aligned}
\tag{B.9}
$$

Therefore we obtain $\mu_e = 2/(1+X)$, which yields $\mu_e = 1.18$ for our assumed helium mass abundance of 30%.

B.3 Hydrogen to Electron Abundance Ratio

The hydrogen abundance relative to the electron number density (χ_{H}) is determined by the He/H abundance ratio:

$$
\chi_{\mathrm{H}} \equiv \frac{n_{\mathrm{H}}}{n_e} = \frac{n_{\mathrm{H}}}{n_{\mathrm{H}} + 2 n_{\mathrm{He}}} = \frac{1}{1 + 2\, n_{\mathrm{He}}/n_{\mathrm{H}}} \sim 0.8\text{--}0.9.
\tag{B.10}
$$

In particular, a primordial gas with 25% He mass fraction ($n_{\mathrm{He}}/n_{\mathrm{H}} = 1/12$) has $n_{\mathrm{H}}/n_e \approx 0.857$. Similarly, our assumption of 30% He mass fraction (i.e., $n_{\mathrm{He}}/n_{\mathrm{H}} = 3/28$) yields $\chi_{\mathrm{H}} \approx 0.82$. This is why the value of $\chi_{\mathrm{H}} = 0.8$ or $\chi_{\mathrm{H}} = 0.9$ is often implicitly assumed in the literature.

Appendix C

Relativistic Plasma Flows

C.1 Dynamical Pair Equations

A sudden release of pure energy into a relatively compact region around the source generate a so-called "fireball". We treat the fireball as a spherically expanding relativistic fluid composed of e^+e^- pairs and γ photons ("$e^\pm\gamma$ fireball"). Photons can be regarded as a relativistic fluid, since they are strongly coupled with pairs due to the tiny mean free path between collisions. The conservation of energy and momentum for a steady hydrodynamical flow in spherical symmetry read

$$\frac{1}{r^2}\frac{d}{dr}\left\{r^2(U+P)\,\Gamma^2\beta\right\} = G^0, \tag{C.1}$$

$$\frac{1}{r^2}\frac{d}{dr}\left\{r^2(U+P)\,\Gamma^2\beta^2\right\} + \frac{dP}{dr} = G^1, \tag{C.2}$$

where $U = U_e + U_r$ is the total energy density, and $P = P_e + P_r$ being the total pressure. Subscripts "e" and "r" denote the plasma term and the radiation term, respectively. All the quantities are measured in the fluid rest-frame. β and Γ are the dimensionless three-velocity and bulk Lorentz factor defined as $\Gamma \equiv (1 - \beta^2)^{-1/2}$. G^μ is the radiation four-force density (Mihalas & Mihalas 1984). Under the optically thick condition ($\tau \gg 1$), there is no radiation flux ($G^0 = G^1 = 0$), and the radiation field stays close to the blackbody spectrum since the photons experience so many collisions that they inevitably thermalize before reaching the photosphere. Therefore $U_r = aT^4 = 3P_r$, where T is the temperature of the fluid. The evolution of the electron number density is tracked by the Boltzmann's equation integrated over the

momentum phase space:

$$\frac{1}{r^2} \frac{d}{dr} \left(r^2 n_e \Gamma \beta\right) = -\langle \sigma_{\mathrm{ann}} v \rangle \left(n_e^2 - n_{e,\mathrm{eq}}^2\right). \tag{C.3}$$

The right-hand side of Equation (C.3) represents the net pair creation rate $(\dot{n}_e)$ due to collisions in $e^+ + e^- \rightleftharpoons \gamma + \gamma'$ interaction. The pair annihilation cross-section is almost constant for $kT < m_e c^2$ being approximately $\langle \sigma_{\mathrm{ann}} v \rangle \approx \pi r_e^2$ with r_e the classical electron radius (Svensson 1982).

C.2 Evolution

The evolution of $e^\pm \gamma$ fireball including n_e evolution has been studied in great detail by Grimsrud & Wasserman (1998), and later developed by a number of authors (e.g., Iwamoto & Takahara 2002; Nakar et al. 2005; Li & Sari 2008). Here we follow their formulation. We assume that the fireball starts with initial conditions, i.e., a Lorentz factor Γ_i, temperature T_i and radius r_i. Combining the equation of state for a relativistic gas $U = 3P$, equation (C.1) and (C.2) reduce to a set of useful scaling laws that describe the radial evolution of Lorentz factor and temperature (Paczynski 1986; Goodman 1986):

$$\Gamma \approx \Gamma_i (r/r_i), \quad T \approx T_i (r_i/r). \tag{C.4}$$

As will be shown below, the evolution of the fireball falls into five phases, characterized by the corresponding radii that determine the physical state of the fireball.

C.2.1 Phase I ($\tau \gg 1$ and $T \gtrsim m_e$)

Initially, the fireball temperature is expected to be large ($T \gg m_e$) so that the pair plasma is in equilibrium state $n_e = n_{e,\mathrm{eq}}$, where $n_{e,\mathrm{eq}}$ is described in Equation (4.1). The fireball is initially confined at rest and immediately start to expand at a speed close to c, while the temperature decreases. Let $r = r_m$ be the radius at which the temperature equals to the electron rest mass energy. Then we obtain

$$\frac{r_m}{r_i} \approx \frac{T_i}{m_e}, \tag{C.5}$$

simply because $Tr = $ const. from Equation (C.4). The density evolution for $r > r_m$ is

$$n_e(r) = \frac{2}{(2\pi)^{3/2}} \lambda_C^{-3} \left(\frac{r_m}{r}\right)^{3/2} e^{-r/r_m} \tag{C.6}$$

as long as the pair equilibrium is met.

C.2.2 Phase II ($\tau \gg 1$ and $T < m_e$)

After the phase I, n_e soon starts to deviate from $n_{e,\mathrm{eq}}$, since $n_{e,\mathrm{eq}}$ decays exponentially with decreasing T. Let us assume a small deviation $\delta n_{e,\mathrm{eq}}$ from $n_e = n_{e,\mathrm{eq}}$ so that $n_e^2 - n_{e,\mathrm{eq}}^2 \approx 2\,n_{e,\mathrm{eq}}\,\delta n_e$. Then Equation (C.3) yields

$$
\begin{aligned}
\delta n_e &\approx -\frac{1}{2r^2\langle\sigma_{\mathrm{ann}}v\rangle n_{e,\mathrm{eq}}}\frac{d}{dr}\left(r^2 n_{e,\mathrm{eq}}\Gamma\beta\right) \\
&\approx -\frac{\Gamma}{2r\langle\sigma_{\mathrm{ann}}v\rangle}\left[3 + \frac{d\ln n_{e,\mathrm{eq}}}{d\ln r}\right] \\
&\approx \frac{\Gamma}{2r\langle\sigma_{\mathrm{ann}}v\rangle}\frac{m_e}{T},
\end{aligned}
\tag{C.7}
$$

where we make use of $\Gamma \propto r$ in the second deformation and $d\ln n_{e,\mathrm{eq}}/d\ln T \sim m_e/T$ in the third. Let $r_\pm$ ($T_\pm$) the radius (temperature) at which the deviation grows to the same order as the equilibrium density ($n_{e,\mathrm{eq}} = \delta n_e$). Then we obtain the following equation

$$\frac{2}{(2\pi)^{3/2}}\lambda_C^{-3}\left(T_\pm/m_e\right)^{3/2} e^{-m_e/T_\pm} = \frac{\Gamma_\pm}{2\pi r_e^2\, r_\pm}\frac{m_e}{T_\pm}. \tag{C.8}$$

Using $T_\pm r_\pm \approx m_e r_m$ and $\Gamma_\pm/r_\pm \approx \Gamma_i/r_i$, this reduces to

$$\frac{r_\pm}{r_m} = \ln\left\{\sqrt{2/\pi}\lambda_C^{-3} r_e^2\, r_i/\Gamma_i\right\} - \frac{5}{2}\ln\left(\frac{r_\pm}{r_m}\right). \tag{C.9}$$

It can be seen that $r_\pm/r_m$ weakly depends on r_i. Evaluating Equation (C.9) numerically, we obtain an analytic fitting formula:

$$\frac{r_\pm}{r_m} \approx 13.4 + \log\left(r_{i,5}\right). \tag{C.10}$$

Thus, we get $r_\pm/r_m \sim 13$ for a reference initial radius $r_i = 10^5$ cm [1], and the corresponding temperature $T_\pm = m_e(r_m/r_\pm) \sim 0.08\, m_e$ (weakly dependent on r_i). Consequently, the electron number density at $r = r_\pm$ is estimated as

$$
\begin{aligned}
n_e(r_\pm) &= n_{e,\mathrm{eq}}(r_\pm) + \delta n_e(r_\pm) \approx 2\,\delta n_e(r_\pm) \\
&\sim \frac{1}{\pi r_e^2}\left(\frac{\Gamma_i}{r_i}\right)\left(\frac{r_\pm}{r_m}\right) \\
&\sim 5.2 \times 10^{20}\,\Gamma_i\, r_{i,5}^{-1} \ \ \mathrm{cm}^{-3},
\end{aligned}
\tag{C.11}
$$

where we have used Equation (C.10) in the last derivation.

C.2.3 Phase III ($\tau \sim 1$ and $T \lesssim m_e$)

For $r > r_\pm$, pairs have already deviated greatly from the equilibrium state ($n_e \gg n_{e,\mathrm{eq}}$) and the pair Equation (C.3) becomes simply

$$
\frac{1}{r^2}\frac{d}{dr}\left(r^3 n_e\right) = -\pi r_e^2 \frac{r_\pm}{\Gamma_\pm} n_e^2,
\tag{C.12}
$$

where we have used $\Gamma = \Gamma_\pm(r/r_\pm)$. Namely, the pair annihilation dominates the pair creation since the number of high-energy photons decrease. This can be solved analytically:

$$
n_e(r) = \frac{n_e(r_\pm)}{1 + (1/3)(r_\pm/r_m)[1 - (r_\pm/r)^3]}\left(\frac{r_\pm}{r}\right)^3.
\tag{C.13}
$$

Then we can calculate the optical depth to the electron scattering as

$$
\begin{aligned}
\tau(r) &= \int_r^\infty 2n_e(s)\sigma_T(1-\beta)\Gamma\, ds \\
&= -\frac{8}{3}\ln\left\{1 - \frac{(1/3)(r_\pm/r_m)(r_\pm/r)^3}{1 + (1/3)(r_\pm/r_m)}\right\}
\end{aligned}
\tag{C.14}
$$

where $\sigma_T = 8\pi/3\, r_e^2$ is the Thomson cross-section. We define the photospheric radius r_{ph} at which the optical depth becomes unity $[\tau(r_{ph}) = 1]$. Then we get

$$
\frac{r_{ph}}{r_\pm} = \left\{\left(1 - e^{-3/8}\right)\left(3\frac{r_m}{r_\pm} + 1\right)\right\}^{-1/3} \sim 1.4,
\tag{C.15}
$$

[1] Grimsrud & Wasserman (1998) originally obtained $r_\pm/r_m \sim 33$ for $r_i = 10^6$ cm, which seems to be an overestimate because they simply neglect $\ln(r_\pm/r_m)$ appearing in the right-hand side of Equation (C.9).

with the corresponding temperature $T_{ph} \sim T_{\pm}(r_{\pm}/r_{ph}) \sim 0.06\, m_e$.

C.2.4 Phase IV $(\tau \lesssim 1$ and $T \ll m_e)$

When $\tau \lesssim 1$, photons start to stream freely, and the single fluid approximation (eq. [C.1] and [C.2]) does not hold anymore. Nevertheless, pairs continue to accelerate up to the point where the escaping radiation could no longer supply enough energy to pairs. The Lorentz factor of pairs (Γ) evolves by the following equation of motion of the pairs:

$$\frac{d\Gamma}{dr} = \frac{\sigma_T F_r}{m_e c^3}, \tag{C.16}$$

where F_r is the photon energy flux that the pairs feel in their rest-frame. We can relate the photon energy flux in the rest frame of pairs to the photon internal energy in the rest frame of photons by a simple Lorentz transformation:

$$F_r = \Gamma_{\rm rel}^2 \beta_{\rm rel} c \left(U_r' + P_r'\right), \tag{C.17}$$

where U_r' and $P_r'(= U_r'/3)$ are the radiation energy density and pressure in the rest frame of photons, respectively. Since the photon energy density in the rest frame of free streaming photons can be approximated by a blackbody, we can write as $U_r' = aT_r^4$, where T_r is the photon temperature in its rest frame (Li & Sari 2008). $\Gamma_{\rm rel}$ is the Lorentz factor for the relative velocity $\beta_{\rm rel}$ of photons (β_r) with respect to the pairs (β), which can be written as

$$\Gamma_{\rm rel} = \Gamma\Gamma_r(1 - \beta\beta_r) \sim \frac{1}{2}\left(\frac{\Gamma_r}{\Gamma} + \frac{\Gamma}{\Gamma_r}\right), \tag{C.18}$$

where Γ_r is the Lorentz factor of photons. Note that photons do not completely decouple from the pairs at this stage and thus Γ_r has a finite value. Then we arrive at

$$\frac{d\Gamma}{dr} = \frac{aT_r^4}{3}\left[\left(\frac{\Gamma_r}{\Gamma}\right)^2 - \left(\frac{\Gamma}{\Gamma_r}\right)^2\right]\frac{\sigma_T}{m_e c^2} \tag{C.19}$$

Combining $T_r = T_i(r_i/r)$ and $\Gamma_r = \Gamma_i(r/r_i)$, the asymptotic Lorentz factor of pairs is obtained as (Li & Sari 2008)

$$\Gamma_\infty \equiv \lim_{r \to \infty} \Gamma \sim 1.46 \left(\frac{3m_e c^2}{r_i a T_i^4 \sigma_T} \right)^{-1/4}$$

$$\sim 1.1 \times 10^3 \, \Gamma_i \, r_{i,5}^{1/4} \left(\frac{T_i}{m_e} \right). \tag{C.20}$$

Conversely, the radius $r = r_\infty$ at which $\Gamma = \Gamma_\infty$ is estimated as $r_\infty \approx (\Gamma_\infty/\Gamma_i) r_i$. Relating r_∞ with $r_{ph} \sim 18 \, (T_i/m_e) \, r_i$, we finally obtain

$$\frac{r_\infty}{r_{ph}} \sim 61 \, r_{i,5}^{1/4} \left(\frac{T_i}{m_e} \right). \tag{C.21}$$

The electron number density at $r = r_\infty$ is $n_e(r_\infty) \sim 3.3 \times 10^{-7} \, r_{i,5}^{-3/4} \, n_e(r_\pm) \sim 1.7 \times 10^{14} \, r_{i,5}^{-7/4}$ cm^{-3}.

C.2.5   Phase V ($\tau \ll 1$ and $T \ll m_e$)

For $r > r_\infty$, the pair annihilation does not occur any more due to the small pair number density, and thus the total number of pairs preserves. Neglecting the right-hand side of Equation (C.3), we obtain $n_e r^2 = $ const. Namely, the evolution of the electron number density is

$$n_e(r) = n_e(r_\infty) \left(\frac{r_\infty}{r} \right)^2. \tag{C.22}$$

C.3   Baryon Loaded Fireball

If the initial fireball forms in the vicinity of the neutron star surface, it is expected that some amount of baryons should be contaminated, which could break the equality of the pair number density ($n_{e^-} > n_{e^+}$) and might affect the late time evolution. Conservation of baryon number and energy reads

$$\dot{M} = 4\pi r^2 A m_p \, n \, \Gamma \beta = const, \tag{C.23}$$

$$L = 4\pi r^2 (U + P) \Gamma^2 \beta = const, \tag{C.24}$$

where n is the baryon number density with mass number A (and atomic number Z) and m_p being the proton mass. We assume the charge neutrality $n_{e^-} = n_{e^+} + Zn$ and

introduce a dimensionless entropy

$$\eta \equiv \frac{L}{\dot{M}}, \tag{C.25}$$

which represents the radiation-to-baryon ratio. We can see that the adiabatic evolution ($\Gamma \propto r$ and $T \propto 1/r$) breaks up when the kinetic energy begins to dominate the radiation energy. This transition takes place when $U + P \sim A m_p n$ with a corresponding radius $r_M = \eta \, (r_i/\Gamma_i)$, above which the Lorentz factor stays constant ($\Gamma_\infty = \eta$). A critical value of η is obtained as

$$\eta_c \sim 200 \left(\frac{Z}{A} \right)^{1/4} r_{i,5}^{1/4} \, \Gamma_i^{3/4} \, \frac{T_i}{m_e}, \tag{C.26}$$

by simply setting $r_M = r_{ph}{}^2$.

In the case of extremely heavy baryon loading $\eta \lesssim \eta_c$, the number density of positrons becomes negligible compared to that of both electrons and baryons (hence $n_e \sim Zn$). Setting $(U + P)_i \sim aT_i^4$ in a set of Equations (C.23)–(C.25), the radial evolution of the electron number density may be estimated as

$$n_e \sim \frac{aT_i^4 \Gamma_i}{m_p} \left(\frac{Z}{A} \right) \times \begin{cases} \eta^{-1} \, (r/r_i)^{-3} & (r < r_M) \\ \eta^{-2} \, (r/r_i)^{-2} & (r > r_M), \end{cases} \tag{C.27}$$

Remarkably, the observed plasma frequency $\nu_p \propto \Gamma n_e^{1/2}$ does not depend on η at $r > r_M$ since $n_e \propto \eta^{-2}$ and $\Gamma = \eta$.

Meanwhile, for a moderate baryon loading $\eta \gg \eta_c$, the coasting Lorentz factor can be estimated in much the same manner as we employed with baryon-free fireball. We define the effective electron mass $\tilde{m}_e$ as

$$\tilde{m}_e = \frac{2 m_e n_e + A m_p n}{2 n_e} \sim m_e + \frac{A m_p}{2Z}. \tag{C.28}$$

Here we assume the number densities of electrons and positrons are nearly equal outside the photospheric radius. By replacing m_e with $\tilde{m}_e$ in Equation (C.20), the coasting Lorentz factor Γ_∞ is found to reduce at most by a factor of $(A m_p / 2Z m_e)^{1/4} \sim 6 \, (A/Z)^{1/4}$ compared to the baryon-free case. The inequality between electron/positron number density does not significantly change $r_{\rm eq}$ and r_{ph} throughout $\eta > \eta_c$ (Grimsrud & Wasserman 1998).

---

[2]Note that, the optical depth is approximated as $\tau \approx Zn\sigma_T r/\Gamma$, taking into account baryon-associated electrons.

Therefore, we conclude that the evolution of electron number density conserves as long as the baryon contamination is small ($\eta \gg \eta_c$). Given the heavy baryon loading, the density at the coasting phase (phase V) would reduce by a factor of $6\,(A/Z)^{1/4}$ at most, since $n_e(r) \propto r_\infty^{-1} \propto \Gamma_\infty^{-1}$.

Appendix D

Relaxation Timescale of Particle Motion during Flares

Here we provide an order-of-magnitude estimate for the timescale over which relaxation of particle motions to dynamical equilibrium takes place. Following Thompson et al. (2002), the radiative force $F_{\rm rad}$ exerted on an electron at a give distance r from the stellar center in the ERF is

$$\begin{aligned}
F_{\rm rad} &= \int d\omega\, \sigma_{\rm res}(\omega) \frac{L_\omega}{4\pi r^2 c} \sim \frac{\pi^2 r_e}{\omega_B} \frac{L}{4\pi r^2} \\
&\sim 1.2 \times 10^{-6} \left(\frac{B_p}{10^{14}\ {\rm G}} \right)^{-1} \left(\frac{r}{R_{\rm NS}} \right) \left(\frac{L}{10^{40}\ {\rm erg\,s}^{-1}} \right) \quad {\rm dyne}, \quad (\text{D.1})
\end{aligned}$$

where L_ω is the spectral intensity of the radiation and $L = \int L_\omega\, d\omega \sim (\omega L_\omega)_{\omega=\omega_B}$ is the pseudo-bolometric luminosity. The angular dependence is neglected in the second equation for simplicity. Consider a deviation of the incident radiation angle in the ERF with respect to the local magnetic field from the equilibrium state $\pi/2 - \theta_i = \Delta\theta_i$; then an equation of particle motion along the magnetic field line gives

$$m_e \dot{v}_e = F_{\rm rad} \sin\Delta\theta_i, \qquad (\text{D.2})$$

where $\dot{v}_e$ is the acceleration (deceleration) along $\boldsymbol{B}$ relative to the initial ERF. Given the size of the magnetic loop comparable to the location of the electron $\sim r$, the dynamical timescale for electrons to acquire the equilibrium velocity distribution can be roughly estimated as

$$\tau_{\rm relax} \sim \sqrt{\frac{r}{|\dot{v}_e|}} \sim \frac{10^{-8}}{|\sin\Delta\theta_i|^{1/2}}\, B_{p,14}^{1/2} L_{40}^{-1/2} \quad {\rm s}. \qquad (\text{D.3})$$

Hence, the timescale for relaxation of particle motion due to strong radiation force is typically much shorter than the duration of the flare. One can also see that the above estimate holds for any location inside magnetosphere because the dependence on r vanishes.